Universität Stuttgart

Institut für Wasser- und Umweltsystemmodellierung

Mitteilungen

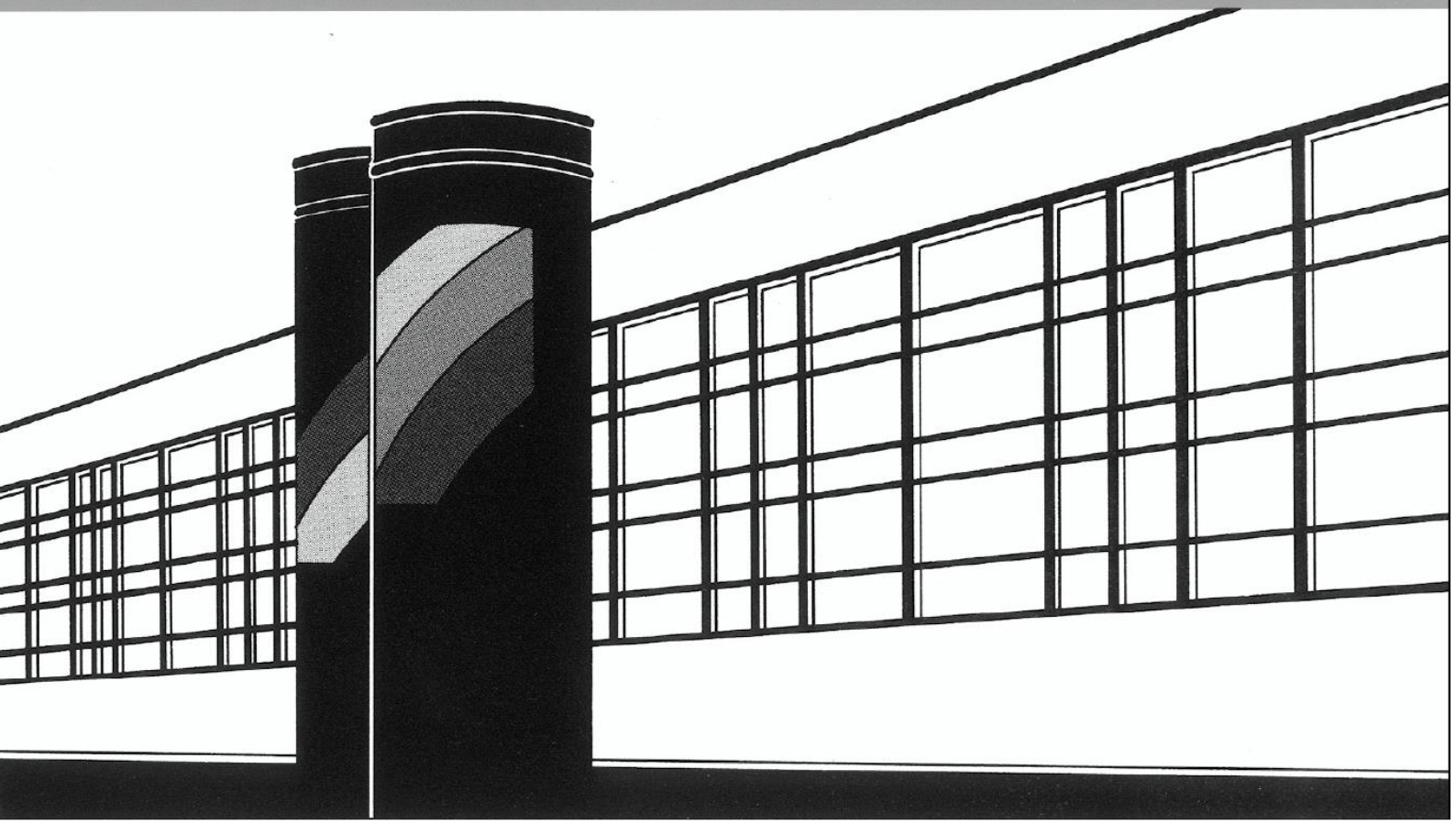

Heft 253 Christoph Grüninger

Numerical Coupling of Navier-Stokes and Darcy Flow for Soil-Water Evaporation

Numerical Coupling of Navier-Stokes and Darcy Flow for Soil-Water Evaporation

von der Fakultät Bau- und Umweltingenieurwissenschaften
und dem Stuttgart Research Centre for Simulation Technology
der Universität Stuttgart
zur Erlangung der Würde eines Doktor-Ingenieurs (Dr.-Ing.)
genehmigte Abhandlung

vorgelegt von

Christoph Oskar Grüninger

aus Göppingen

Hauptberichter:	apl. Prof. Dr. rer. nat. Bernd Flemisch
Mitberichter:	Prof. Dr.-Ing. Rainer Helmig
	Prof. Béatrice Rivière, Ph. D., Rice University, Houston, TX

Tag der mündlichen Prüfung: 18. Mai 2017

Institut für Wasser- und Umweltsystemmodellierung
der Universität Stuttgart

2017

Heft 253

Numerical Coupling of Navier-Stokes and Darcy Flow for Soil-Water Evaporation

von
Christoph Grüninger

Eigenverlag des Instituts für Wasser- und Umweltsystemmodellierung
der Universität Stuttgart

D93 Numerical Coupling of Navier-Stokes and Darcy Flow for Soil-Water Evaporation

Bibliografische Information der Deutschen Nationalbibliothek
Die Deutsche Nationalbibliothek verzeichnet diese Publikation in der Deutschen Nationalbibliografie; detaillierte bibliografische Daten sind im Internet über http://www.d-nb.de abrufbar

Grüninger, Christoph:
Numerical Coupling of Navier-Stokes and Darcy Flow for Soil-Water Evaporation, Universität Stuttgart. - Stuttgart: Institut für Wasser- und Umweltsystem-modellierung, 2017

(Mitteilungen Institut für Wasser- und Umweltsystemmodellierung, Universität Stuttgart: H. 253)
Zugl.: Stuttgart, Univ., Diss., 2017
ISBN 978-3-942036-57-3

NE: Institut für Wasser- und Umweltsystemmodellierung <Stuttgart>: Mitteilungen

Herausgegeben 2017 vom Eigenverlag des Instituts für Wasser- und Umweltsystem-modellierung

Druck: Document Center S. Kästl, Ostfildern

Abstract

The objective of this work is to develop algorithms and provide a framework for an efficient coupling of free flow and porous-medium flow to simulate porous-medium-soil-water evaporation. The implementation must particularly be capable of simulating laminar free flows, be fast enough for applied research, and cover simulations in two and three dimensions with complex geometries.

General We introduce a model for a compositional non-isothermal free flow coupled with a two-fluid-phase compositional non-isothermal porous-medium flow. The free flow is modeled with the Navier-Stokes, component and energy transport equations. The porous-medium flow is modeled with compositional two-fluid-phase Darcy and energy transport equations. As the pressure has different orders in the free-flow and porous-medium-flow subdomains, the coupling is not straightforward. Although the simulation of the coupled flows is motivated by a laboratory experiment to measure soil-water evaporation caused by wind blowing over a water-filled porous bed, we intend to also explore its use in other applications

Conceptual model The free flow is considered to be incompressible and laminar. We also assume that air and water follow nonlinear laws that describe their physical properties, and binary diffusion. Within the porous medium only creeping flows occur. Many quantities are averaged and used in a macroscopic sense. We use a formulation of two-phase Darcy law using the liquid saturation and the gas pressure as primary variables. The component mass fractions are calculated by Henry's law and the vapor pressure. The liquid phase may locally vanish leading to a variable switch, where the vapor mass fraction is tracked instead of the liquid saturation. We assume that a local thermodynamic equilibrium is valid everywhere within the domain, even across the interface. We follow the coupling concept proposed by Mosthaf et al. [2011], including the Beavers-Joseph-Saffman approach which has a sharp interface between the two subdomains.

Discretization We use a cell-centered finite volume method (FVM) on an axially parallel grid to discretize the partial differential equations of the compositional two-phase Darcy's law, the heat equation in both subdomains, and the component transport in the free-flow domain. For the Navier-Stokes equation, we use the marker and cell (MAC) scheme which moves the degrees of freedom for the velocities towards the edges of the grid elements, forming one secondary, staggered grid per dimension. The MAC scheme is stable and can be interpreted as a FVM. The coupling conditions are applied without additional variables along the coupling interface. They are incorporated as Dirichlet, Neumann or Robin boundary conditions resulting in interface fluxes.

Implementation For the porous-medium flow, we use the finite-volume implementation provided by DuMu^{x}. The marker and cell scheme is implemented on top of Dune-PDELab utilizing

the material laws from DuMu^x. The grid is split into two subdomains and the grid elements can be graded. This is especially useful for developing smaller elements closer to the interface. We can use complex geometries in two or three dimensions. The coupling is provided by a Dune-Multidomain local coupling operator. The time integration is approximated with an implicit Euler scheme and an adaptive time stepping. The system of nonlinear equations is linearized by a Newton method. All contributions to the Jacobian are compiled in one system of linear equations.

Solving the linear system The resulting matrices are difficult to solve. Although they are sparse, with a blocked structure of bands of nonzero entries, the matrices contain a saddle point problem and are nonsymmetric. We solve the matrices with direct methods. We also investigate iterative methods to get around the computational complexity and memory consumption of the direct methods: An Algebraic Multigrid (AMG) method, a Schur complement method, and a Generalized Minimal Residual method (GMRES) preconditioned with the reordering algorithm MC64 and an incomplete LU factorization with threshold and pivoting (ILUTP). We experience problems with AMG's error criteria leading to convergence problems. The Schur complement method is slow, as the Schur complement, which is not explicitly calculated, lacks preconditioners. GMRES with ILUTP shows similar results to a direct method, but reveals a restriction on the time step size for larger problem sizes, flawing a possible speedup compared to the direct methods.

Numerical results We validate our implementation for proper operation with the simulation of a laboratory experiment for soil-water evaporation. The laboratory experiment consists of a water-filled sand box with a horizontal pipe installed on top of the box and a propeller creating a constant air flow. We use the implementation to investigate the influence of the Reynolds number on the evaporation rate. Further, we compare the two-dimensional simplification to different three-dimensional geometries with regard to the effects on the evaporation. For low Reynolds numbers, the geometry of the free-flow subdomain has a significant influence on the evaporation rate.

Another application involves a geological repository for nuclear waste. We investigate the water saturation in the concrete ceiling and the rock above a ventilation gallery. Our results conclude that within the first 200 years, only part of the concrete will dry, and the rock will remain unaffected. This confirms the same result by another group, though they observe evaporation rates up to the factor of ten higher.

Our third application is the water management within a polymer electrolyte membrane (PEM) fuel cell. Neglecting electrochemistry, we simulate the flow through the gas channels and the porous layer covering the membrane, including the transport of vapor and liquid water, the evaporation of water within the porous layer, and how energy and vapor are conveyed away. In comparison to the above applications, the gas phase flow is not horizontally parallel to the porous bed, but is forced to completely enter the porous medium and leave it through a second gas channel. We also briefly compare two different gas channel layouts.

Summary We introduce the discretization of the coupling concept and its implementation. We conduct simulations of applications from different areas. We show the versatility of our approach and that it can be used as the basis for further research.

German abstract

Kurzfassung

Ziel der vorliegenden Arbeit ist die Entwicklung von Algorithmen und das Bereitstellen eines Frameworks für die effiziente Kopplung zwischen einer freien Strömung und einer Strömung in einem porösen Medium um Bodenwasserverdunstung zu simulieren. Insbesondere muss die Software in der Lage sein laminare freie Strömung zu simulieren, effizient genug sein für Anwendungen und zwei- wie drei-dimensionale Simulationen mit komplexen Geometrien abdecken.

Überblick Wir stellen ein Kopplungsmodell für eine nichtisotherme freie Strömung und eine nichtisotherme Zwei-Flüssigphasen-Strömung im porösen Medium, jeweils mit Komponententransport, vor. Die freie Strömung ist mit der Navier-Stokes-, einer Komponenten- und einer Energietransport-Gleichung modelliert, die Strömung im porösen Medium mit einer Darcy-Gleichung für zwei Flüssigphasen und zwei Komponenten und einer Energietransport-Gleichung. Die Kopplung wird erschwert durch den Druck, der in den Teilgebieten von unterschiedlicher Ordnung ist. Die Simulation der gekoppelten Strömungen ist durch einen Laborversuch zu Bodenwasserverdunstung motiviert, aber auch andere Anwendungen wollen wir untersuchen können.

Modellkonzept Die freie Strömung sei inkompressibel und laminar, die physikalischen Fluid-Eigenschaften folgen nichtlinearen Gesetzen. Wir beschränken uns auf binäre Diffusion und im porösen Medium gibt es nur schleichende Strömung. Viele Größen sind gemittelt und werden makroskopisch verwendet. Die Zwei-Phasen-Darcy-Strömung hat die Primärvariablen Sättigung der Flüssigphase und Gasphasen-Druck. Die Massenbrüche der Komponenten werden durch das Henry-Gesetz und den Dampfdruck beschrieben. Stellenweise kann die Flüssigphase verschwinden, dann wird die Primärvariable von der Wassersättigung zum Dampfmassenbruch verändert. Es gelte ein lokales thermodynamisches Gleichgewicht, auch über das Kopplungsinterface hinweg. Wir übernehmen das Kopplungskonzept von Mosthaf et al. [2011], das auf dem Beavers-Joseph-Saffman-Ansatz mit einem abrupten Interface zwischen den Teilgebieten beruht.

Diskretisierung Wir diskretisieren mit einer zell-zentrierten Finite-Volumen-Methode (FVM) auf einem achsenparallelen Gitter alle partiellen Differentialgleichungen außer der Navier-Stokes-Gleichung. Für letztere setzen wir die Marker-and-Cell-Methode (MAC) ein, welche die Geschwindigkeitsfreiheitsgrade auf die Elementkanten verschiebt und ein versetztes Sekundärgitter pro Dimension bildet. Die MAC-Methode ist stabil und kann als FVM aufgefasst werden. Die Kopplungsbedingungen werden ohne zusätzliche Variablen auf dem Interface als Dirichlet-, Neumann- oder Robin-Randbedingungen angewandt, welche Flüsse über das Interface ergeben.

Implementierung Für die Strömung im porösen Medium kommt die FVM-Implementierung von DuMu^{x} zum Einsatz. MAC wird mit Hilfe von Dune-PDELab und den Materialgesetzen von

DuMu^x umgesetzt. Das Gitter wird in zwei Teilgebiete zerlegt, Gitterelemente können stufenweise verkleinert werden, was für kleinere Zellen in Richtung der Kopplung verwendet wird. Außerdem können sowohl zwei- wie drei-dimensionale komplexe Geometrien umgesetzt werden. Die Kopplung wird mit einem lokalen Operator auf Basis von Dune-Multidomain durchgeführt. Die Zeitintegration wird mit einem impliziten Euler-Verfahren genähert. Wir linearisieren das System nichtlinearer Gleichungen mit einem Newton-Verfahren. Alle Beiträge für die Jacobimatrix werden in einem System linearer Gleichungen zusammengetragen.

Lösen des linearen Systems Die resultierenden Matrizen sind schwierig zu lösen. Sie sind dünnbesetzt mit einer geblockten Bandstruktur der Nicht-Null-Einträge. Allerdings enthalten sie ein Sattelpunktproblem und sind unsymmetrisch. Wir lösen sie mit direkten Verfahren, die eine hohe Rechenzeit- und Speicherkomplexität aufweisen. Wir untersuchen alternativ iterative Verfahren: ein algebraisches Mehrgitterverfahren (AMG), ein Schurkomplement-Verfahren und ein GMRES-Verfahren (Generalized Minimal Residual), vorkonditioniert mit einer Umsortierung nach dem MC64-Algorithmus und einer unvollständigen LU-Zerlegung mit Schwellwert und Pivotisierung (ILUTP). Wir stellen Konvergenzprobleme durch Unstimmigkeiten beim Fehlerkriterium des AMGs fest. Das Schurkomplement-Verfahren ist langsam, weil ein geeigneter Vorkonditionierer für das nicht explizite Schurkomplement fehlt. GMRES mit ILUTP erzielt ähnliche Ergebnisse wie die direkten Verfahren, zeigt aber eine Beschränkung der Zeitschrittweite für größere Probleme, was mögliche Beschleunigungen zunichtemacht.

Numerische Ergebnisse Wir überprüfen unsere Implementierung mit der Simulation eines Laborexperiments zur Bodenwasserverdunstung. Der Versuchsaufbau ist eine wassergefüllte Sandbox mit einer horizontal darüber verlaufenden Röhre mit konstanter Luftströmung. Wir untersuchen den Einfluss der Reynolds-Zahl auf die Verdunstungsrate und vergleichen zweidimensionale Vereinfachungen mit verschiedenen dreidimensionalen Geometrien. Für moderate Reynolds-Zahlen hat die Geometrie des Gebiets der freien Strömung einen signifikanten Einfluss.

Eine andere Anwendung ist ein atomares Endlager in geologischen Formationen. Untersucht wird die Wassersättigung in der Betondecke und dem darüber liegenden Deckgestein eines Lüftungsschachts. Innerhalb der ersten 200 Jahre trocknet der Beton nur teilweise und das Gestein bleibt unverändert. Dies stimmt mit dem Ergebnis einer anderen Forschergruppe überein, die allerdings Verdunstungsraten erzielen, die von unseren bis zu einem Faktor zehn abweichen.

Unsere dritte Anwendung ist das Wassermanagement einer Polymer-Elektrolyt-Membran-Brennstoffzelle (PEM). Unter Vernachlässigung der Elektrochemie simulieren wir die Strömung durch die Gaskanäle und die poröse Schicht um die Membran unter Berücksichtigung des Transports von Dampf und flüssigem Wasser, der Verdunstung in der porösen Schicht und des Abtransports von Energie und Dampf. Die Strömung findet nicht nur horizontal über die poröse Schicht statt, sondern muss vollständig ins poröse Medium eindringen, um einen zweiten Gaskanal zu erreichen. Wir vergleichen auch zwei unterschiedliche Anordnungen der Gaskanäle.

Zusammenfassung Wir stellen die Diskretisierung des Kopplungskonzepts und dessen Umsetzung vor. Wir simulieren Anwendungen aus unterschiedlichen Bereichen. Dabei zeigen wir die Vielseitigkeit unseres Ansatzes und dass dieser für weitere Forschungen verwendet werden kann.

Contents

List of Figures

Das Wasser ist ein freundliches Element für den, der damit bekannt ist und es zu behandeln weiß.

Johann Wolfgang von Goethe, 1809

1 Motivation

Water is essential to life as mankind knows it [Ball, 2005]. We are surrounded by water; it is part of all humans, animals and plants, as well as in the atmosphere and in the ground below our feet. Only 35 percent to 40 percent of the world's precipitation runs off to rivers and lakes or seeps into the soil, meaning that the remaining balance evaporates to the atmosphere. On average, one meter of water evaporates every year. This has an impact on Earth's energy budget; more than half of the net solar radiation over the land surface is disposed towards evaporation. In comparison, photosynthesis usually dissipates less than one percent of the net solar radiation, with five percent dissipation at the maximum. [Brutsaert, 1982] Astonishingly, the knowledge about this ubiquitous process is inadequate. Rind et al. [1997] report on the discrepancy between measurements and several evaporation modeling approaches. In order to determine future water availability, accurate estimates of the moisture transport are crucial.

The evaporation of a fluid inside a porous medium to the surrounding atmosphere is a more general problem. We are going to investigate the flow of dry air parallel to a sand-filled box. This porous medium has a sharp margin and can contain both gas and liquid. The liquid inside the porous medium evaporates and diffuses into the free flow. Outside the porous medium the liquid only occurs vaporized in the gas as a component. Figure 1.1a provides a schematic diagram of such a problem. The setup and our numerical examples are based on a lab experiment performed by Mosthaf et al. [2014]. For a photograph of the setup see figure 1.1b. This general setup has a wide range of applications and is not limited to investigations of the evaporation of soil water.

There are several applications related to soil science: In arid regions with high evaporation potential, irrigated fields are susceptible to salinization which lowers or destroys their soil fertility. Jambhekar et al. [2015] simulate the evaporation of soil water to analyze this evaporative salinization. Another application is the underground storage of supercritical carbon dioxide, as part of carbon dioxide capture and storage (CCS). Oldenburg and Unger [2004] investigated the consequences of a leakage in the cap rock, leading to the release of carbon dioxide to the atmosphere where it forms a plume, see figure 1.2a. The authors found out that the CO_2 concentration would remain low enough to not endanger human life on the surface. Often, the solution outside the porous medium is of no importance, just its effect inside the porous medium. So-called top boundary conditions approximately account for the effect of the evaporation without its computational costs. These boundary conditions are developed by examining the coupled problem [Tang and Riley, 2013]. Besides storing carbon dioxide in the subsurface, engineers plan to build underground end disposal facilities for their nuclear waste, too. Zhang [2015] and Masson et al. [2016] try to predict the evaporation of water from the encircling rock to excavated ventilation galleries. This helps to estimate the structural integrity of the rock and the galleries for at least a hundred years. Humans have buried another legacy: 100 million landmines endanger the life of civilians, especially children. Landmines alter soil moisture and temperature which makes them detectable at the surface [Smits et al., 2013].

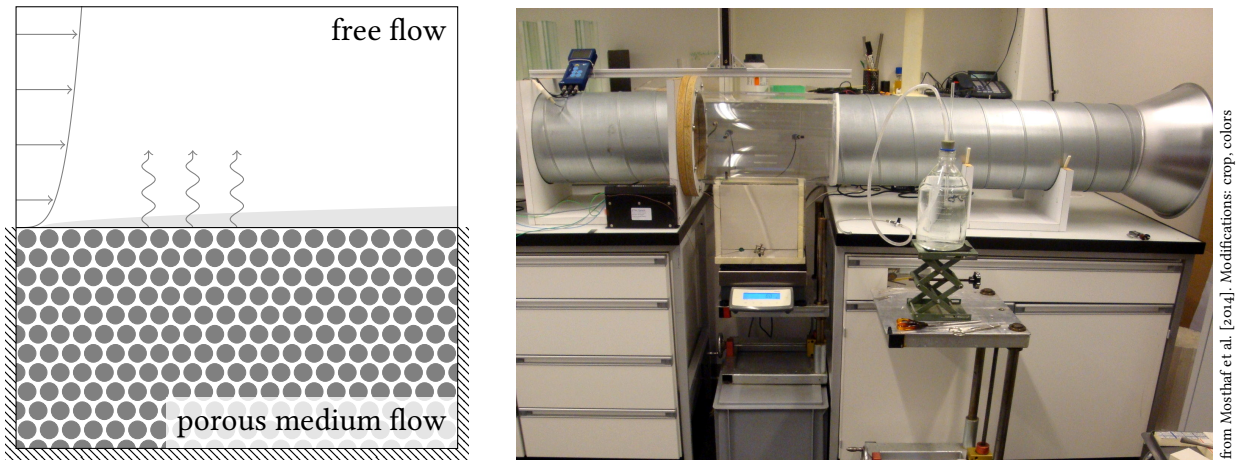

(a) (b)

Figure 1.1: General problem of coupled Navier-Stokes/Darcy flow (a) schematic diagram with evaporation from the porous medium and evolved boundary layer (b) laboratory experiment motivating our simulation, taken at ETH Zurich, group of Danny Or

The setup can also be applied to technical problems. The industrial drying of wood, brick, food and similar materials is energy consuming. For several countries, the related energy consumption accounts for 10% to 25% of total industrial energy consumption. Defraeye [2014] gives an overview on published research in this field. Better simulations could reduce the energy consumption and improve the quality of the dried goods. Closely related is refrigeration of food bulk [Verboven et al., 2006]. In some cases, the amount of energy required for evaporation is not a negative quality, it can be utilized as transpiration cooling of rocket engines to protect engine parts from too high temperatures for increased reliability and fuel economy [Dahmen et al., 2014]. In fuel cells, based on proton exchange membranes (PEM), the membranes are surrounded by a thin porous medium where as little as possible liquid water should remain, see figure 1.4. The liquid water blocks the gases for the proton exchange and must be transported away in the gas channel [Baber et al., 2012]. Cimolin and Discacciati [2013] model a ventilation channel inside a motorcycle helmet, see figure 1.2b. The channel transports fresh air to the comfort tissue for cooling and evacuation of sweat. It prevents overheating of the driver's head and fogging of the visor. Another group of applications are biological problems, for example, the simulation of a pre-lens tear film on a contact lens [Usha et al., 2013] or blood vessels surrounding organs and tissue [Discacciati and Quarteroni, 2009].

1.1 Classification

As various applications exist, there are plenty of publications describing the simulation of the coupled Navier-Stokes and Darcy flow to explore these evaporation processes. We are going to present the objectives of this work, related works using the Beavers-Joseph condition for the coupling, and alternative coupling approaches.

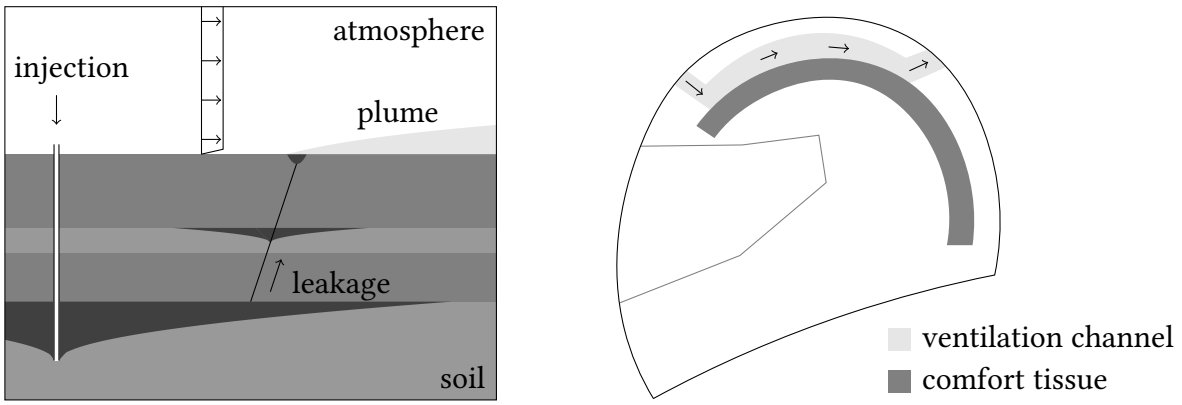

(a) (b)

Figure 1.2: Further applications for the setup (a) carbon dioxide stored in a geological formation, leakage leads to a CO_2 plume in the atmosphere (b) motorcycle helmet with an included channel for cooling next to the comfort tissue, after Cimolin and Discacciati [2013]

1.1.1 Objectives

We want to provide a numerical simulator to investigate evaporation of soil water under the influence of wind streaming along the surface. The simulator incorporates all relevant processes in the soil and atmosphere. The atmospheric processes are a Navier-Stokes flow of air with vapor transport. The processes included within the soil are a two-fluid-phase Darcy flow of water and air, the transport of one substance as a component of the other, and the evaporation of water. Both parts involve an energy balance so as to track the temperature, see figure 1.3.

The parts are coupled with a sharp interface using a Beavers-Joseph condition. We want to discretize the system of partial differential equations with robust numerical, grid-based schemes, and have chosen the finite volume method (FVM) and the marker and cell (MAC) scheme in order to do so. This enables simulations of realistic setups. The whole discretized system is linearized with Newton's method, resulting in a monolithic coupling without the need to iterate between atmospheric and soil parts to solve the system. The system of linear equations is either solved by a direct method, or uses an iterative method. The later performs a reordering of the matrix to make it diagonally dominant, preconditions with an incomplete LU factorization, and solves the system with an iterative Krylov subspace method. This is proposed by Duff and Koster [2001] and is successfully tested for various problems in Benzi et al. [2000].

With this, we demonstrate the capability to efficiently simulate lab experiments, a fuel cell, and a part of a geological repository for nuclear waste. These simulations include complex geometries and three-dimensional problems.

1.1.2 Related works

Several groups have performed experiments related to this coupled problem. Most experiments are confined to single-phase and isothermal setups, for example, the flow over a porous bed made up of regular cylinders [Prinos et al., 2003], velocity measurements close to the interface of a stack of spheres [Pokrajac and Manes, 2009], or particle image velocimetry (PIV) measurements

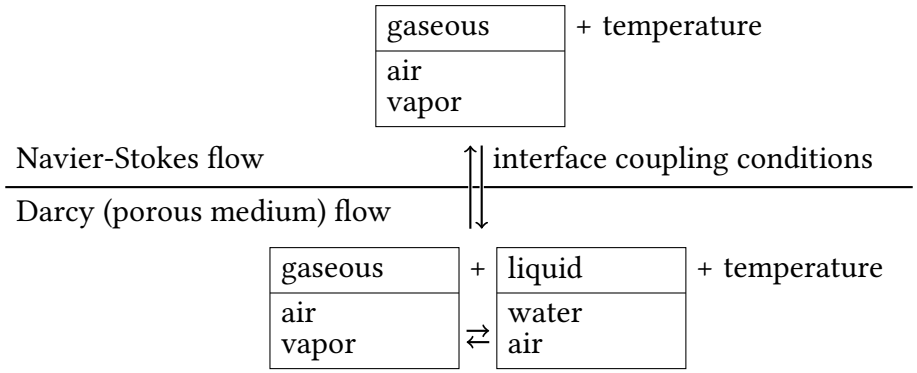

Figure 1.3: Phases and their components as they occur in the two subdomains. Each box stands for a phase with its components.

to understand better turbulence over porous media [Suga, 2016]. Dahmen et al. [2014] measure the temperature with an infrared camera. Davarzani et al. [2014] and Mosthaf et al. [2014] perform experiments using a wind channel over a porous, water-filled bed to measure data for simulations of evaporation. These experiments motivate the simulation setup of this work. Shahraeeni et al. [2012] identify several characteristics of the evaporation rate of such systems and explains possible reasons. Defraeye et al. [2016] survey the water content of a drying apple slice with neutron imaging.

From a mathematical point of view, the coupling of mass and momentum transfers with the Beavers-Joseph condition is a challenging problem. Discacciati and Quarteroni [2009] give an overview of more than a dozen analyses and further related experimental and applied works. Examples of such articles include an asymptotic analytic solution for a coupled problem [Jäger et al., 2001], a proof of existence and convergence of a weak scheme [Layton et al., 2002], and a coupling scheme for various discontinuous Galerkin methods [Kanschat and Rivière, 2010]. All of these works are limited to single-phase isothermal problems. But there are exceptions. In Çeşmelioğlu and Rivière [2012], the authors proof the existence of a weak solution of a coupled Stokes/Darcy problem with a component transport. And Ervin et al. [2015] examine a quasi-stationary Stokes/Darcy system again with a component transport. We are not aware of any paper presenting mathematical proofs concerning coupling and energy transport or two-fluid-phase Darcy flow.

Several works address the efficiency of coupled Stokes/Darcy simulations. Chidyagwai and Rivière [2011] propose the use of a two-grid method. Badea et al. [2010] compare different linearizations for the coupled problem and report the convergence of Newton's method to be inferior to the ones of a fix-point or a Richardson iteration. Iterative Dirichlet-Neumann coupling schemes between the two subdomains are examined by Discacciati [2004], resulting in a harsh limit concerning the time-step size. Numerical tests with our code base did not show an advantage of the iterative single-phase coupling over a monolithic coupling with respect to the computational effort, at least with a direct solver for the linear system [Ackermann, 2016]. A Robin-Robin coupling yields a better iterative coupling scheme [Discacciati et al., 2007, Birgle et al., 2017]. As the Navier-Stokes equation needs a finer temporal resolution, the coupled system can be calculated with coarse time steps and simulate the atmospheric part in-between more often with smaller time steps

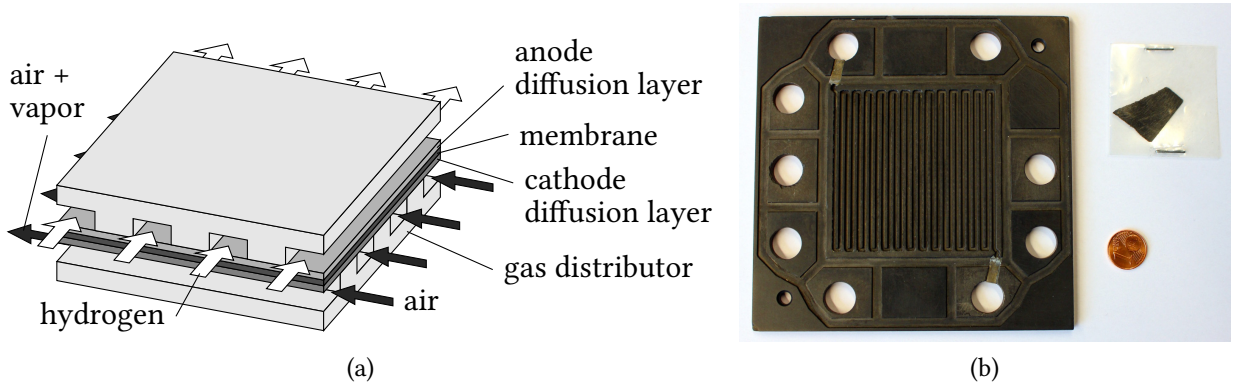

Figure 1.4: Fuel cell with gas distributor and porous diffusion layer (a) schematic diagram (b) left: gas distributor with included gas channel used in laboratory experiment; top right: porous diffusion layer, courtesy of University of Stuttgart, group of Gerhart Eigenberger

[Rybak and Magiera, 2014, Rybak et al., 2015]. Discacciati and Quarteroni [2004] introduce a Schur complement preconditioner for the coupled problem. More general preconditioners for coupled problems have been proposed, for example, in Howle et al. [2013]. There are publications using ILU methods as preconditioner for saddle-point problems arising from the pure Navier-Stokes equation without a coupling, but this solution strategy is known to have limitations [Zeng and Wesseling, 1995, Konshin et al., 2015].

Without the burden of analyzing the complex system of partial differential equations, applied scientists study coupled evaporation problems with numerical software. The review article from Defraeye [2014] presents 20 different implementations of Stokes/Darcy coupling to simulate drying, but many use simplifying assumptions compared to our setup. An early work is Salinger et al. [1994] simulating spontaneous ignition of coal stockpiles with a non-isothermal compositional coupling. Defraeye et al. [2012] present a non-isothermal two-phase compositional Darcy flow coupled to a non-isothermal Stokes flow. The main difference here comes from the coupling, where the flow in the porous medium is calculated first, the fluxes across the interface second, and the free flow third. Masson et al. [2016] have a similar setup, but pre-calculate the free flow and only solve the energy and the component transport coupled to the porous-medium flow. Compared to our setup, the work from Dahmen et al. [2014] does not include the vapor mass fraction transport in the free flow. Our work is the successor of another implementation based on DuMu^x [Mosthaf et al., 2011, Baber et al., 2012, Mosthaf et al., 2014, Fetzer et al., 2016]. The main difference is the used discretization scheme, namely a finite volume scheme compared to their equal-order scheme which tends to oscillations in the Stokes flow.

1.1.3 Alternative approaches

There are alternative approaches that are used to simulate a free-flow/porous-medium-flow coupling. We present a selection of approaches, see fig 1.5 for a schematic comparison.

The most straight forward method is a pore-scale simulation of the whole system without any coupling condition. This can be done with a Navier-Stokes discretization as in Chandesris et al.

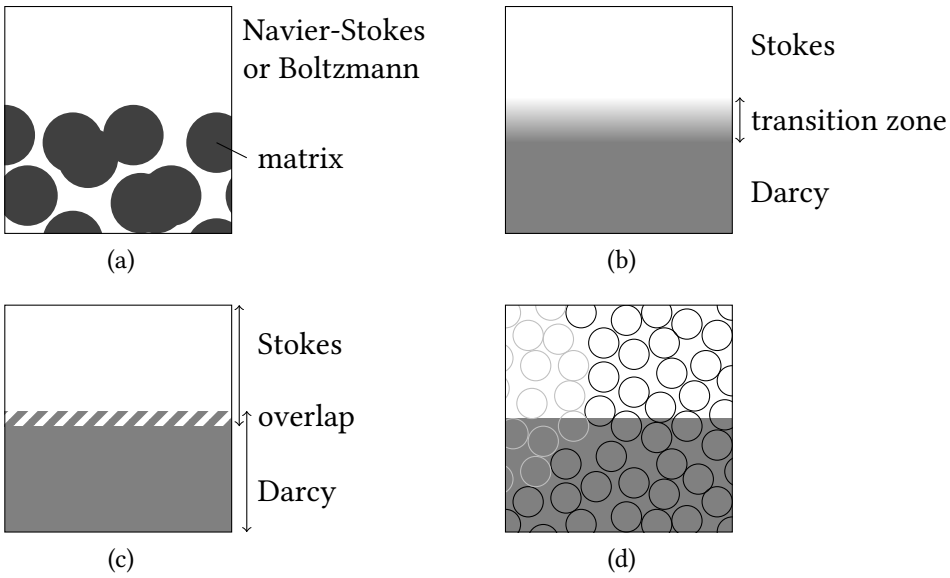

Figure 1.5: Alternative coupling approaches (a) pore-scale simulation (b) Brinkman (c) interface control domain decomposition (d) smoothed particle hydrodynamics

[2013] or by solving the discrete Boltzmann equation with a lattice Boltzmann method [Krafczyk et al., 2014]. For both variants, the pore geometry must be resolved which requires a fine grid and leads to a high computational demand. The pore geometry must be either simple or obtained from a computer tomography scan. These dependencies limit the domain size to small lab samples. Two-phase flow computations exacerbate the problem with the computational costs. Pore-scale simulations are often used to evaluate coupling concepts [Fattahi et al., 2016] or to obtain effective parameters for upscaled models [D'Hueppe, 2011].

The Brinkman equation [Brinkman, 1949] combines Darcy flow and Stokes flow. A parameter blends the portions of both equations. This leads to a transition zone between the free and the porous-medium flow. In numerical simulations, the transition zone must maintain a certain thickness. Krotkiewski et al. [2015] use the Brinkman equation to simulate a fractured porous medium obtained from a computer tomography scan. A comparison between an implementation using a Beavers-Joseph-type coupling and an implementation using a transition layer modeled by a Brinkman domain shows good agreement when the transition layers are small and have low permeabilities [Nield and Kuznetsov, 2009]. The Brinkman equation is easy to implement and is used in commercial codes [Cimolin and Discacciati, 2013]. The application of the Brinkman equation for larger domains is challenged by Nield [2009]. We are not aware of any work extending the Brinkman model to two-phase flows in the porous medium.

The interface control domain decomposition (ICDD) method uses overlapping subdomains. It is a recent idea, presented by Discacciati et al. [2016], to get rid of the Beavers-Joseph condition. In the overlapping region, the Stokes and the Darcy flow are present. This is physically justified, as the free flow enters the porous medium to some extent. The coupling is achieved by Dirichlet boundary conditions for pressure and velocity at the ends of the overlapping domain. The gap between the overlapping solutions is minimized. Compared to a Robin-Robin or Dirichlet-Neumann coupling, we expect that the ICDD leads to a better converging domain decomposition method.

A different way to simulate flow would use smoothed particle hydrodynamics (SPH) methods. These methods are not based on a mesh but represent the flow by a large number of small particles. The particles move similar to the fluid and maintain some of the fluid's properties, for example, its density. Shao [2010] presents an interaction of water inside and outside of a porous medium. Basser et al. [2016] use SPH to simulate a water tank with a porous bed where salt water displaces the less dense fresh water.

1.2 Outline

This chapter explains the motivation behind this work and outlines the goals of the work at hand. Chapter two introduces the basic physical concepts, for example, pressure, phases and porous media, and important processes like diffusion and evaporation. The third chapter describes the mathematical model, i. e., the relevant processes are modeled as mathematical equations. Especially partial differential equations are an important tool. In chapter four the equations are discretized to render a computational approximation possible, and the used schemes as well as the implementation are presented. Chapter five contains numerical results to demonstrate the capabilities of the implementation and its applications: We will simulate a laboratory experiment concerning soil-water evaporation, a part of a nuclear waste repository in a geological formation, and a section of a fuel cell. The final chapter concludes with the summary of results and an outlook.

וְאֵד יַעֲלֶה מִן־הָאָרֶץ וְהִשְׁקָה אֶת־כָּל־פְּנֵי־הָאֲדָמָה׃

Genesis, 2:6

2 Fundamentals

Before we dive into the coupling of different flow regimes, we will sort out the involved scales, introduce the basic terms and physical phenomena related to the physics of soil water evaporation. The basis of this chapter, and the sources for further reading, are the books White [1999], which gives more details about fluid mechanics, Bear [1972], which is a classic with respect to flow in porous media, and Helmig [1997], which describes multi-phase flows in porous media.

2.0.1 Scales

To describe and model the physics of soil water evaporation, we need to discuss different scales.

The molecular scale describes the molecules, i. e., the positions of all molecules and their interaction. In general, applications contain too many molecules to simulate them directly, for example, one mole of water weights approximately 18 grams but contains more than 10^{23} molecules. Nevertheless, the properties and the behavior of the molecules determine fluid properties like density, viscosity and wettability. The molecules are a discrete representation of the system.

The microscopic scale averages the molecules to create continuous quantities. The fluid phases, their properties and the pore geometries are resolved in a discrete way. The motion of the fluids is described by multiphase Navier-Stokes equations.

For the porous medium, we use in general the macroscopic scale, which integrates over numerous pores. The size of the averaged volume must be large enough to avoid quantities with fluctuating properties. It should be small enough to preserve influential features like low-permeability lenses. Such a volume is called a representative elementary volume (REV). The porous matrix and the phases are represented as porosity, saturations, pressures, and velocities which are averaged quantities.

Usual time scales for free flows are seconds or microseconds; for porous-medium flows the usual time scales span hours, days or even weeks. Given that each domain has an entirely different scale, coupling the domains is challenging, and results in an increase of computational effort.

2.1 Fluids

If a substance resists shear stress, it is a solid, otherwise in general a fluid. Fluids are further classified into liquids and gases, varying in the effect of cohesive forces. Liquids have strong intermolecular bonds, a definite volume and no fixed shape; in a gravitation field, they form a free surface. Gases have weak bonds resulting in small cohesive forces. They have no definite volume but spread apart until they are held by a confinement or they form a hydrostatic atmosphere. In our applications, we will be investigating all three realms, with air and vapor as gasses, water as a liquid, and the porous medium as a solid.

2.1.1 Phases and components

Two fluids do not necessarily blend, for example, rain drops don't mix with the surrounding air. Immiscible fluids form phases with distinct fluid-fluid interfaces between them. Within a phase, thermodynamical properties are locally homogenous with abrupt changes across the interfaces. We denote general phases with α. Miscible fluids form one phase, called a solution. In other words, a phase may consist of multiple components κ. Gases are miscible with other gases, just as the gas phase air is made up of different components. A system cannot have more than a single gaseous phase.

For the mixing ratio of a phase α we use the mass fraction

$$X_\alpha^\kappa \coloneqq \frac{m_\alpha^\kappa}{m_\alpha} \tag{2.1}$$

with the mass of the component m_α^κ and the total mass of the phase m_α. As already indicated by the name, the mass fractions total one

$$\sum_\kappa X_\alpha^\kappa = 1. \tag{2.2}$$

Likewise, a phase can be partitioned by the component's amount of substance $n_{\text{mole},\alpha}^\kappa$. This is called mole fraction and is defined as

$$x_{\text{mole},\alpha}^\kappa \coloneqq \frac{n_{\text{mole},\alpha}^\kappa}{n_{\text{mole},\alpha}} \tag{2.3}$$

with the phase's total amount of substance $n_{\text{mole},\alpha}$. The amount of substance describes the number of molecules. It is measured in moles. The mass fraction and the mole fraction are convertible via

$$X_\alpha^\kappa = \frac{x_{\text{mole},\alpha}^\kappa M^\kappa}{\sum_\iota x_{\text{mole},\alpha}^\iota M^\iota} \tag{2.4}$$

with the component's κ molar mass M^κ and ι iterating over all components of the phase α.

An example of the above concepts would be a glass of champagne. The glass is solid and inside the glass are a liquid and a gaseous phase. The liquid phase champagne has the components water, alcohol, dissolved carbon dioxide, and some more. The gaseous phase is found above the champagne's surface and within the gas bubbles which ascend toward the surface. The surface forms a clearly visible interface between the liquid champagne, the gas bubbles, and the gaseous phase above. Eventually the champagne goes stale, no more gas bubbles appear and the mass fraction of carbon dioxide in the champagne has dropped.

Gibbs' phase rule

$$\text{number of unknowns} = \text{number of components} - \text{number of phases} + 2 \tag{2.5}$$

indicates the number of unknowns required for a mathematical description of a system consisting of multiple phases and components.

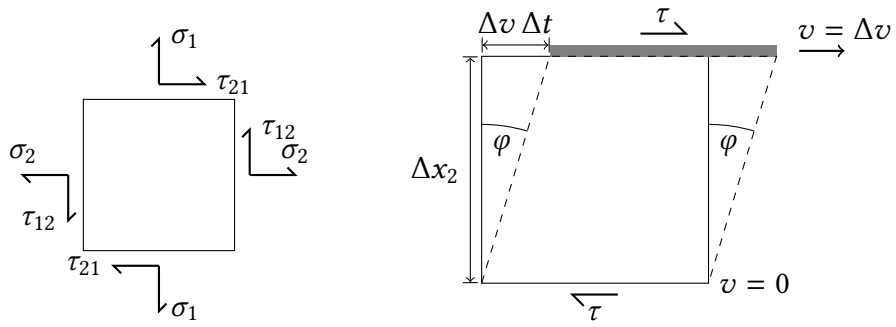

(a) (b)

Figure 2.1: (a) Components of the stress tensor σ in two dimensions (b) Shear deformation in a fluid, after [White, 1999]

2.1.2 Kinematics

The motion of a fluid is described by its velocity v, which is a vector field.

Inside a fluid the molecules exert forces on each other. On the averaged continuum scale, these internal forces are called stress σ and are expressed as a tensor

$$\sigma = \begin{pmatrix} \sigma_1 & \tau_{12} & \tau_{13} \\ \tau_{21} & \sigma_2 & \tau_{23} \\ \tau_{31} & \tau_{32} & \sigma_3 \end{pmatrix}. \tag{2.6}$$

The diagonal entries are normal stresses which describe compression or tension. The compression stress relates to pressure $p \coloneqq -\frac{1}{3}\sum_i \sigma_i$ which is scalar. Pressure differences and gradients drive fluid flows and are often more important than the absolute pressure level. The off-diagonal stress entries are called shear stresses τ and represent forces perpendicular to an infinitesimal cross section, for a two-dimensional example, reference figure 2.1a.

2.1.3 Fluid properties

A sheared fluid moves at a strain rate proportional to μ^{-1}. This property is called dynamic viscosity μ and is a measure for the fluid's resistance to deformation.

A fluid's mass per volume is called its density ϱ. Closely related to density is compressibility. If a fluid is compressed by a slightly increased pressure, the fluid's density has a strong pressure dependency and is called compressible. Incompressible fluids maintain their volume despite pressure changes. Compressibility must be considered when high velocities occur. Velocities below 30% of the speed of sound a are considered incompressible. Table 2.2 contains the values for the speed of sound in air and water. The speed of sound in air grows moderate at a rate of roughly $0.6\,\mathrm{m/s}$ per Kelvin of increased temperature [Siekmann and Thamsen, 2008]. For the applications we have in mind, we stay below 30% of these values by at least a factor of ten. In the following, we will always assume incompressible fluids.

The ideal gas law

$$\varrho = \frac{p}{R_{\mathrm{s,g}} T} \tag{2.7}$$

Table 2.2: Fluid properties of air and water at $p = 10^5$ Pa, after Siekmann and Thamsen [2008]

	Dynamic viscosity	Density	Speed of sound
Air	$18.0 \cdot 10^{-6}\,\mathrm{kg/ms}$	$1.188\,\mathrm{kg/m^3}$	$347\,\mathrm{m/s}$
Water	$1.002 \cdot 10^{-3}\,\mathrm{kg/ms}$	$998.2\,\mathrm{kg/m^3}$	$1\,400\,\mathrm{m/s}$
Remark	$T = 20°\mathrm{C}$	$T = 20°\mathrm{C}$	$T = 25°\mathrm{C}$

relates pressure p and temperature T with density ϱ. The specific gas constant $R_{\mathrm{s,g}}$ can be obtained by $R_{\mathrm{s,g}} = \frac{R}{M_{\mathrm{g}}}$ with the gas' molar mass M_{g} and the ideal gas constant $R = 8.314\,\mathrm{J/molK}$. Instead, the constant can be measured as $R_{\mathrm{s,g}} = c_{\mathrm{p}} - c_{\mathrm{V}}$ using the gas' specific heat for a constant pressure c_{p} and the gas' specific heat for a constant volume c_{V}.

In a mixture of gases, each component κ has a partial pressure p_{g}^{κ}. This is the hypothetical pressure of the component, if all other components were to be removed, while the volume and the temperature were kept constant. According to Dalton's law, the sum of partial pressures of all components equals the total pressure of the gas mixture

$$p_{\mathrm{mole,g}} = \sum_{\kappa} p_{\mathrm{g}}^{\kappa}, \tag{2.8}$$

assuming ideal gases. For an ideal mixture of gases, the ratio of partial pressures is the same as the ratio of the amount of substance

$$x_{\mathrm{mole,g}}^{\kappa} = \frac{p_{\mathrm{g}}^{\kappa}}{p_{\mathrm{g}}}. \tag{2.9}$$

Further, according to Henry's law, the partial pressure p_{g}^{κ} of a gas is proportional to the molar mass fraction of dissolved gas $x_{\mathrm{mole,g}}^{\kappa}$ in a liquid

$$x_{\mathrm{mole,g}}^{\kappa} = \frac{p_{\mathrm{g}}^{\kappa}}{H^{\kappa}}. \tag{2.10}$$

This law is limited to dilute solutions. The Henry coefficient H^{κ} is specific to the two substances, and depends on the temperature. It can be calculated for air and water as

$$H_{\mathrm{air,water}}^{\mathrm{a}}(T) = \frac{10^{10}}{0.8942 + 1.47 \exp\left(-0.04394\,1/\mathrm{K} \cdot (T - 273.15\,\mathrm{K})\right)}. \tag{2.11}$$

The formula results from a fitting to tabulated data [Finsterle, 1993].

For a liquid in contact with another substance, a free interfacial energy develops between them, because each phase has different inter-molecular attractions at the contact surface. A surface with free energy tends to contract, leading to interfacial tension. Effects of this include the surface tension and the tendency of small amounts of water to form drops.

When a shear stress τ shears a fluid element, like in figure 2.1b, common fluids like water and air approximately fulfill

$$\tau = \mu \frac{\mathrm{d}}{\mathrm{d}x_2} v_1. \tag{2.12}$$

These fluids are called Newtonian fluids.

2.1.4 Internal energy and temperature

For all materials, its molecules have a random movement which sums up to zero. Besides moving, molecules do also spin, vibrate, and move in other ways we will not further consider because they are related to chemical reactions or radioactivity.

Relative to the material's mass, this is subsumed as the material's specific internal energy u. According to the first law of thermodynamics, the specific internal energy for a closed system is constant under any transformation. If we consider the work to change the volume of the material as well, we get the specific enthalpy

$$h := u + \frac{p}{\varrho}. \tag{2.13}$$

For multiple components, the specific phase enthalpy is approximately the component specific enthalpies, weighted by the component mass fraction

$$h_\alpha = \sum_\kappa h_\alpha^\kappa X_\alpha^\kappa. \tag{2.14}$$

This relation is solely used for the gaseous phase. For the liquid phase enthalpy, we use the one of liquid water $h_\mathrm{l} = h_\mathrm{l}^\mathrm{w}$ because only small portions of air can dissolve in water.

The state changes consume additional energy, called enthalpy of vaporization and enthalpy of fusion. This share of the internal energy is referred to as latent heat. The remainder is the sensible heat. The temperature T quantifies the sensible heat. More sensible heat leads to higher temperatures, while the latent heat does not affect the temperature. The specific heat capacity c indicates how much the temperature is increased by added heat. Between two points with different temperatures a sensible heat flux establishes from the hotter point to the cooler one until the temperatures equalizes. A related material property is the thermal conductivity λ.

The specific enthalpy is described as a function of temperature and phase pressure. For liquid water and vapor we use the thermodynamic formulation given by the IAPWS [2007]. For air we use $h^\mathrm{a}(T) = 1005\,\mathrm{J/kg\,K}(T - 273.15\,\mathrm{K})$ [Kays et al., 2005].

If a variable has the same value throughout the whole system, it is in equilibrium. When the values change little in a small surrounding volume and a small slice in time, it is in local equilibrium. If local mechanical, thermal and chemical equilibrium occur together, it is called local thermodynamic equilibrium; with other words, pressure, temperature and component can be considered locally constant. In the following, we assume local thermal thermodynamic equilibrium. As a consequence, at a given point, all components, phases and the soil matrix have the same temperature. All movements are slow enough to allow the temperature to equilibrate. This holds across the coupling interface, too.

2.2 Porous media

A porous medium is a solid material that contains pores, which are connected to allow the fluid to move through the pores. Examples for porous media are soil, rock, biological tissue like human skin, food or wood, and manufactured materials like concrete or ceramics. When the pores contain n fluid phases, it is a $n+1$-phase system. From now on, we refer to fluid phases just as phases and explicitly name the solid phase.

We assume the matrix to be neutral, without sorption, dissolution or similar processes. Further, the matrix and the pores do not change, neither in their position nor their size. There are scenarios where these assumptions are not valid, such as a drying tomato, a flexing muscle, or a clogging filter.

2.2.1 Properties

Porous-media properties are difficult to obtain and are subject to high uncertainty. Measurements are limited to either small samples which are examined in a lab or to larger areas treated with pumping tests which cannot reveal heterogeneities. Computations on the microscale with a fully resolved pore geometry are resource consuming. A common approach is to average the quantities and solve the problem on the averaged macroscale. With the representative elementary volume (REV) technique, we smooth the physical properties which oscillates strongly in space. The averaging leads to a model with a predictive power that is easier to solve.

The porosity ϕ is characteristic for a porous medium. For a given volume V, it is the fraction not occupied by the matrix. For a formal definition, we use a characteristic function

$$\chi_{\text{pore}}(x) \coloneqq \begin{cases} 0 & x \in \text{solid matrix} \\ 1 & x \in \text{pore space} \end{cases}$$

for all $x \in V$, indicating pore space in the microscale. Integrating χ_{pore} over the volume of interest V defines the porosity

$$\phi \coloneqq \frac{1}{|V|} \int_V \chi_{\text{pore}}(\xi) \, \mathrm{d}\xi \tag{2.15}$$

which is a macroscopic quantity. The fluids cannot flow through isolated or dead-end pores; these are excluded by the definition of the effective porosity. Here, we always mean effective porosity when we use the term porosity.

The second characteristic and macroscopic value is the permeability k of the porous medium. It describes the ease of a fluid flowing through the pores. It is possible to have different permeabilities in different directions. Layered structures or the pore structure like in figure 2.3 are reasons for this. We will consider only isotropic permeabilities, which only depend on the location and are otherwise immutable. The permeability is sometimes called intrinsic permeability to distinguish it from the relative permeability introduced later.

2.2.2 Averaging

The crucial point in our definition of porosity (2.15) is the size of the volume V, the REV. If this volume is chosen too small, the averaged property ϕ still oscillates. If it is chosen too large, the averaging might smooth out relevant features. Usually a REV covers hundreds to thousands of pores.

An artificial example is the porosity calculation for a porous medium composed of periodic, same-sized circles, see figure 2.4. Averaging by a rectangular REV with the edge length a reveals a strong influence of the size a, that decreases for larger a. A good approximation of the theoretic limit $\lim_{a\to\infty}(\phi) = 1 - \pi/4 \approx 0.22$ is reached for modest sizes of a. Also notable are differences

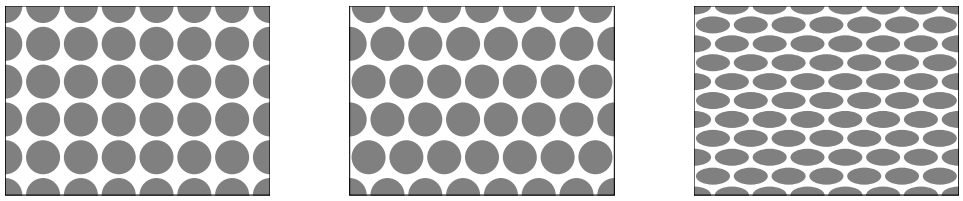

(a) (b) (c)

Figure 2.3: Porous media with the same porosity but different permeabilities (a) same permeability in x_1 and x_2 direction (b) interlaced grains, more permeable in x_1 than x_2 direction (c) distorted grains increase the anisotropy further

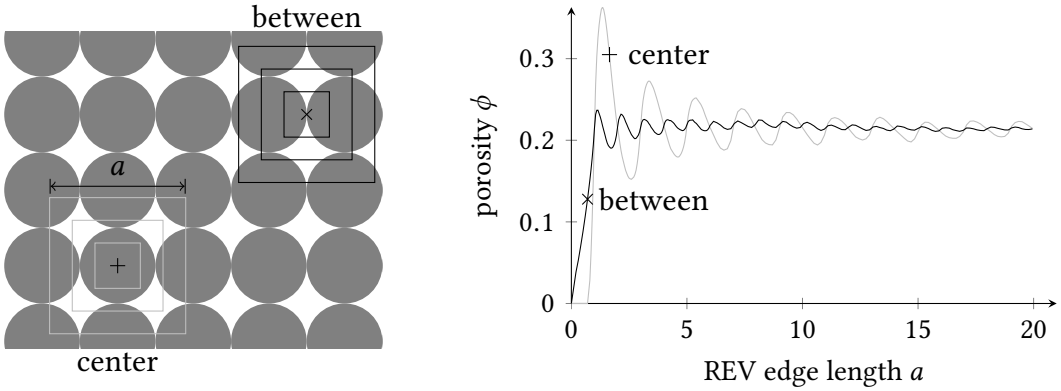

Figure 2.4: Averaging over the pore space yields the porosity, the dependency on the location diminishes with the growing size of the REV, after Holzbecher [1996]

in the porosity depending on the location, which again diminishes for larger a. Both effects are exaggerated by the regularity of this artificial porous medium, where real-world porous media will behave less strikingly. For our simulations, the size of the REV is of minor importance. We assume that the used values are measured in consideration of a suitable REV and that we can use the resulting function as if they were continuous [Holzbecher, 1996].

2.2.3 Fluids within porous media

If the pores are filled with immiscible fluids, the saturation S_α of a single fluid α describes the fraction of the pore space, filled with α. Similar to the definition of the porosity, we introduce a characteristic function

$$\chi_\alpha(x) \coloneqq \begin{cases} 1 & \text{phase } \alpha \text{ present at } x \\ 0 & \text{else} \end{cases}$$

for all $x \in V$. Again, we integrate χ_α over the volume of interest V to define the saturation

$$S_\alpha \coloneqq \frac{\int_V \chi_\alpha(\xi)\,\mathrm{d}\xi}{\int_V \chi_{\text{pore}}(\xi)\,\mathrm{d}\xi}. \tag{2.16}$$

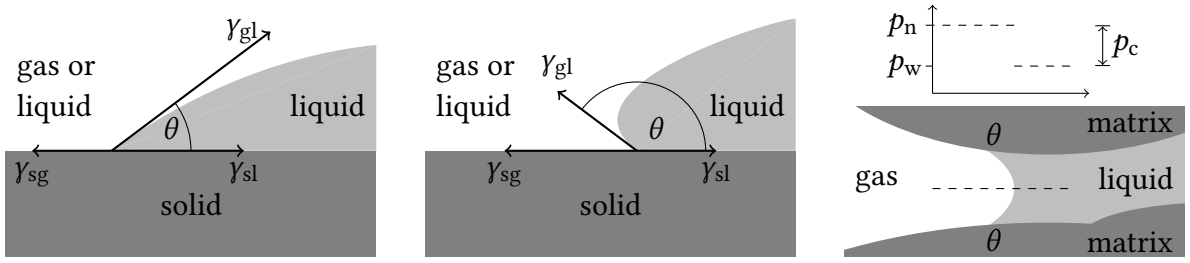

Figure 2.5: Interfacial tensions and contact angle θ for a (a) wettable drop on a surface (b) with interchanged wettabilities. (c) Partially water-filled pore, resulting in a pressure discontinuity.

Some fraction of a phase remains trapped in small pores or covering the grains as a thin film. This remaining fraction of the phase is called the residual saturation $S_{\alpha,\mathrm{r}}$ of a phase α. As this fraction does not affect the relevant processes, we treat it as part of the matrix and exclude it by using the effective saturation

$$S_{\alpha,\mathrm{e}} \coloneqq \frac{S_\alpha - S_{\alpha,\mathrm{r}}}{1 - \sum_\iota S_{\iota,\mathrm{r}}} \tag{2.17}$$

instead of the saturations without further distinction.

It is evident, that the fluids fill the complete pore space,

$$\sum_\alpha S_\alpha = 1. \tag{2.18}$$

We limit ourselves to porous-media systems containing two phases. Systems with more phases are common in petroleum engineering [Natvig and Lie, 2008] or groundwater remediation [Class and Helmig, 2002].

Within a porous medium, the interfacial tension between two immiscible fluids has additional effects. In contact with a solid wall, the surface and the wall draw a specific contact angle θ, see figure 2.5a and 2.5b. Young's equation for surface wetting

$$\cos(\theta) = \frac{\gamma_{sg} - \gamma_{sl}}{\gamma_{gl}} \tag{2.19}$$

describes $\cos(\theta)$ by the involved surface tensions γ. As a consequence, an equilibrium does not exist for $\gamma_{sg} - \gamma_{sl} > \gamma_{gl}$. Instead, the liquid spreads indefinitely over the solid wall. A fluid with an acute contact angle $\theta < \pi$ is called a wetting fluid, a fluid with an obtuse contact angle $\theta > \pi$ is a nonwetting one. The wettability depends on the both fluids and the solid, replacing one can change the wettability. For example, given the two fluids water and air on a piece of cloth, usually water is the wetting fluid. After the piece of cloth is treated with polytetrafluoroethylene (PTFE or Teflon), air acts as the wetting phase and water drops roll off. The piece of cloth becomes, to some extent, water-proof.

When two immiscible fluids meet within a pore, the pressure has a discontinuity at the interface between them, see figure 2.5c. This pressure difference depends on the interface curvature inside

the pore. It is called the capillary pressure p_c and is defined as

$$p_c := p_n - p_w \tag{2.20}$$

with p_n and p_w being the pressure of the nonwetting and the wetting phase respectively. The capillary pressure is always positive. In other words, the pressure on the convex side of an interface is smaller.

Despite the fact that the capillary pressure is defined at the pore level, we will use an averaged macroscopic capillary pressure henceforth. Similar to the properties of porous media presented above, the capillary pressure is difficult to measure, and only insufficient theoretical descriptions are known. A common approach is the capillary pressure–saturation relationship which expresses the capillary pressure as a function of the wetting phase saturation. The functions are theoretically derived and contain constants which have a physical meaning, but their value cannot be measured. Instead, the functions are fitted to measurements in pumping tests. Well known capillary pressure–saturation relationships are from Brooks and Corey [1964] and Van Genuchten [1980]. We will use the latter in this work and will present it in more detail. The function is

$$p_c(S_w) = \frac{1}{\alpha_{VG}} \left(S_w^{-\frac{1}{m_{VG}}} - 1 \right)^{\frac{1}{n_{VG}}} \tag{2.21}$$

with α_{VG}, m_{VG} and n_{VG} parameters to be determined. The inverse of α_{VG} is called the entry pressure and describes the minimum pressure difference needed to displace the wetting phase. Taken from the Mualem theory, it is common to use $m_{VG} = 1 - \frac{1}{n_{VG}}$. Usually n_{VG} is chosen between 2 and 5, it relates to the pore-size distribution. Figure 2.6a exemplifies the effect of the parameters.

Having two immiscible fluids percolating through the same porous medium does not mean they flow together like a boat on a river. The flow happens along paths of pores filled or partially filled with the same phase. In partially filled pores, the wetting phase coats the pores with a thin film, the other phase flows in the center of the pore. When the saturation drops, more and more paths become disconnected, impeding the motion of the phase. The relative permeability k_α reproduces this effect on an averaged scale. There are several models, which are often related to capillary pressure–saturation relationships. Again, the models introduced by Brooks and Corey [1964] and Van Genuchten [1980] are most often used. We present and will use the latter, which comprises of two scalar functions, one for each phase, dependent on the wetting phase saturation:

$$k_w(S_w) = \sqrt{S_w} \left(1 - \left(1 - S_w^{\frac{1}{m_{VG}}} \right)^{m_{VG}} \right)^2 \tag{2.22}$$

$$k_n(S_w) = \sqrt[3]{1 - S_w} \left(1 - S_w^{\frac{1}{m_{VG}}} \right)^{2m_{VG}}. \tag{2.23}$$

The square and cubic roots in the formulas are common choices and can be adjusted as they represent the connectivity of pores [Helmig, 1997]. Figure 2.6b illustrates the functions with different values for n_{VG}.

Sometimes the relative permeabilities are multiplied by the intrinsic permeability to get an overall permeability. The expression $\frac{k_\alpha}{\nu}$ is called mobility.

For a porous medium, the capillary pressure–saturation and relative permeability curves are ambiguous. The ones described above can only be obtained by a single drainage cycle, meaning,

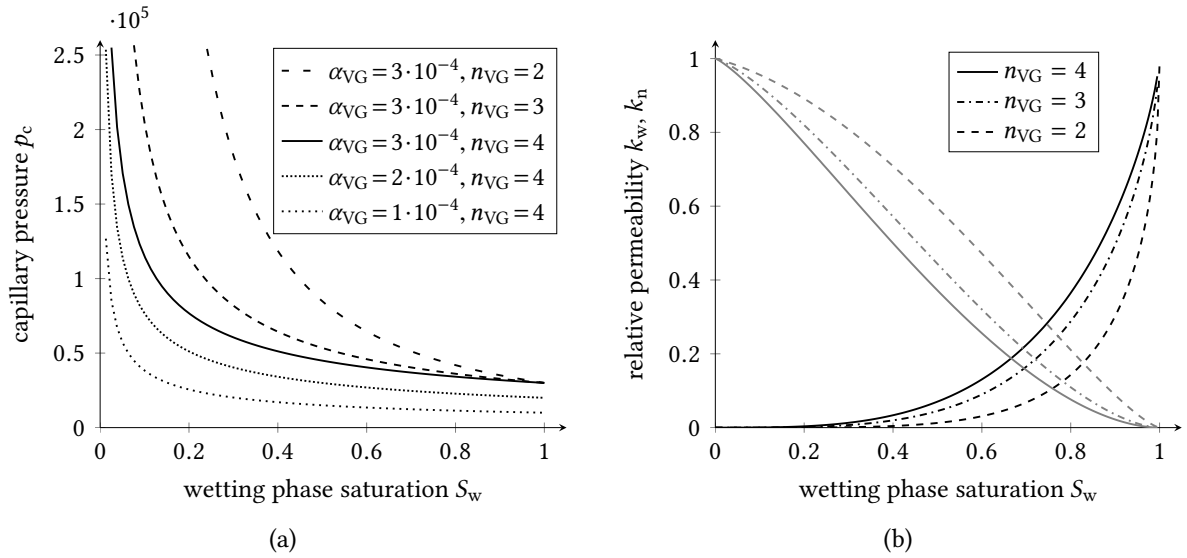

Figure 2.6: Van Genuchten model with different parameters for (a) capillary pressure–saturation relationship (b) relative permeabilites, black: for the wetting phase k_w, gray: for the nonwetting phase k_n

a reduction in the wetting fluid saturation. For the inverse process, called imbibition, the curve differs. The curve depends on past drainage and imbibition cycles. This hysteresis depends on several pore-scale effects. We neglect hysteresis in our applications as multiple drainage and imbibition cycles rarely occur.

The effective thermal conductivity of the porous medium filled with two phases λ_{pm} is calculated by a semi-empirical approach after Johansen [1975]. It interpolates between the effective thermal conductivity of the porous medium completely saturated with the non-wetting fluid and the one of the porous medium completely saturated with the wetting fluid. These two conductivities are obtained from the geometric means of the soil conductivity and the according fluid conductivities.

2.3 Occurring processes

Several processes are involved in the evaporation of soil water. Only when the relevant ones are captured, we will get the overall evaporation right.

2.3.1 Diffusion and advection

The processes of diffusion and advection influence the distribution of components. These two phenomena are building blocks that describe the processes behind component distributions or heat spreading. Further, they are so characteristic that different numerical discretizations must be applied.

Diffusion is a process driven by concentration differences of a component. The component diffuses from areas with a higher concentration to areas with a lower concentration. On the

molecular level, the Brownian motion causes molecular diffusion: Molecules move randomly around and statistically, more molecules leave the area of high concentration than enter. The exchange rate of the diffusive fluxes increases with a higher difference in concentration. The resulting effect on the macroscopic scale is called diffusion, too. It is described by the Fickian law $j = -D\,\mathrm{grad}(\omega)$, which relates the diffusive flux j with the gradient of a concentration ω, scaled by a diffusion coefficient D. The concentration ω can be a component within the phase or the temperature.

We assume equimolar component diffusion in the binary system, i. e., the component diffusion coefficients of a phase is the same as the diffusion coefficients of its components $D_\alpha = D_\alpha^{\mathrm{a}} = D_\alpha^{\mathrm{w}}$ and the gradients of the component molar mass fractions have the same absolute value while they are directed opposite: $\mathrm{grad}\left(x^{\mathrm{a}}_{\mathrm{mole},\alpha}\right) = -\,\mathrm{grad}\left(x^{\mathrm{w}}_{\mathrm{mole},\alpha}\right)$.

Advection describes the transport of particles, components, or temperature by the motion of the fluid. The term advection is often confused with—or not properly distinguished from—convection. Convection is the combination of advection and molecular diffusion [Delleur, 2006].

The description of advection in the porous medium is blurred by the averaged velocity on the pore scale. This effect is called mechanical dispersion and is not a physical transport process, but an effect caused by the averaging. Dispersion depends on the flow velocity, fluid properties and the porous medium. As this process blurs areas of large concentration gradient, it can be described similarly to the effects of diffusion.

On the macroscopic scale, we model diffusion and dispersion together with a macroscopic porous medium diffusion coefficient $D_{\mathrm{pm},\alpha} = \phi\tau_{\mathrm{pm}} S_\alpha D_\alpha$ with the pore tortuosity τ_{pm} [Helmig, 1997].

The binary diffusion coefficient is a property of the phase, $D_{\mathrm{l}} = 2.01 \cdot 10^{-9}\,\mathrm{m^2/s} \cdot \frac{T}{298.15\,\mathrm{K}}$ and $D_{\mathrm{g}} = 2.13 \cdot 10^{-5}\,\mathrm{m^2/s} \cdot \frac{p_{\mathrm{g}}}{10^5\,\mathrm{Pa}} \cdot \left(\frac{T}{273.15\,\mathrm{K}}\right)^{1.8}$.

2.3.2 Turbulence

The viscosity impacts the characteristics of a fluid flow which can be described using the dimensionless Reynolds number

$$Re \coloneqq \frac{\varrho}{\mu} v l, \tag{2.24}$$

a ratio of inertial forces to viscous forces. Along with the dynamic viscosity, the Reynolds number is calculated using a characteristic velocity v and a characteristic length l. The characteristic velocity and length are usually chosen at an important geometric feature. In a pipe flow, the velocity is the maximum velocity, and the length is the pipe diameter. In popular flow applications, one should employ common characteristic values to get comparable values. For example, the flow around an airfoil has the flight speed as the characteristic speed and the chord line, the straight line between the leading and the trailing edges, as the characteristic length.

Flows with small Reynolds numbers $Re < 1$ are flows with dominant viscous effects and are called creeping flows. Flows with moderate Reynolds numbers are laminar and show mild inerta effects, i. e., pressure and velocity vary locally without severe oscillations. Flows with high Reynolds numbers are turbulent flows. The critical Reynolds number indicating turbulent flows depends on the setup. For pipe flows it is $Re_{\mathrm{crit}} \approx 2300$. This value changes with pipe roughness and wiggles in inflow.

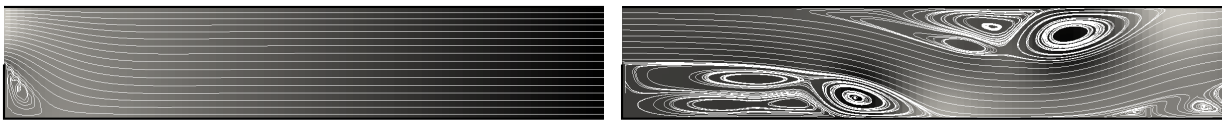

(a) laminar, $Re = 10$ (b) turbulent, $Re = 2\,500$

Figure 2.7: Examples for laminar and turbulent flow, the backward-facing step creates shear stresses on the fluid entering from the left. The white lines are stream lines, the background color indicates the pressure.

In this work, we have to consider turbulent flows as a back-of-the-envelope calculation shows: Estimating the Reynolds number for our applications using the properties of air from table 2.2, the characteristic values $l = 0.25\,\text{cm}$, $v = 0.1\,\text{m/s}$ and a pipe flow as a close enough model, we get $Re = 1.65 \cdot 10^6$, which is way bigger than Re_{crit}.

Turbulence is the motion of fluids with eddies in a wide range of scales. A turbulent flow shows a strong sensitivity of the fluid field and wall geometry changes to the point of seemingly random behavior. Originating from small waved disturbances that grow bigger, it is impossible to avoid turbulence in a world bearing imperfections. Turbulent flows manifest as unstable and fluctuating in a random and high-frequent manner. Only the turbulent flow in the example shown in figure 2.7 contains pressure oscillations and a multitude of eddies. Turbulence leads to enhanced mixing like for temperature or transported components. For more details concerning turbulent flows we refer to in the books of White [1999], Pope [2000] and Ferziger and Perić [2002].

The eddies form an energy cascade; large eddies decay into smaller and smaller ones and eventually dissipate into thermal energy. The larger eddies contain and transport a great deal of the kinetic energy, while smaller eddies have the effect of an additional viscosity. The dissipation into thermal energy happens at the Kolmogorov microscale which defines a length scale, a time scale and a velocity. We illustrate the diminutive size of the length scale using the example of a flat-cylinder wake with a moderate Reynolds number of $Re = 1\,840$. Near the cylinder, the Kolmogorov length scale η lays between 0.47 mm and 0.8 mm [Aronson and Löfdahl, 1993]. A thorough analysis of the Kolmogorov microscale is provided by Pope [2000]. The energy cascade is disputed, as it was never directly observed [Liu et al., 2014].

We are especially interested in turbulent effects near a plate or a wall, because of their relevance to our application. It is a classical experiment used by Ludwig Prandtl to develop the boundary layer theory over 100 years ago. When a fluid flows in parallel along a wall, like in figure 2.8, the shear stress influence the velocity profile perpendicular to the wall and a boundary layer forms of slower, laminar flow. The unavoidable wall roughness causes small wiggles which build up. At the transition point, or more likely the transition zone surrounding the point, small disturbances lead to turbulent behavior and the boundary layer breaks into two parts: The sublayer that remains laminar, but has a reduced thickness, and the turbulent boundary sublayer, which grows further. The turbulent boundary layer thickness δ is approximated as the wall distance where the velocity reaches 99% of the outer flow velocity v_∞. Relative to the space above the turbulent boundary layer, it remains tiny. In the example from above, it is in the sub-millimeter range.

Similar to the boundary layer formed by slower fluids near the wall, a thermal boundary layer forms above a wall with a different temperature, and a component boundary layer forms above a

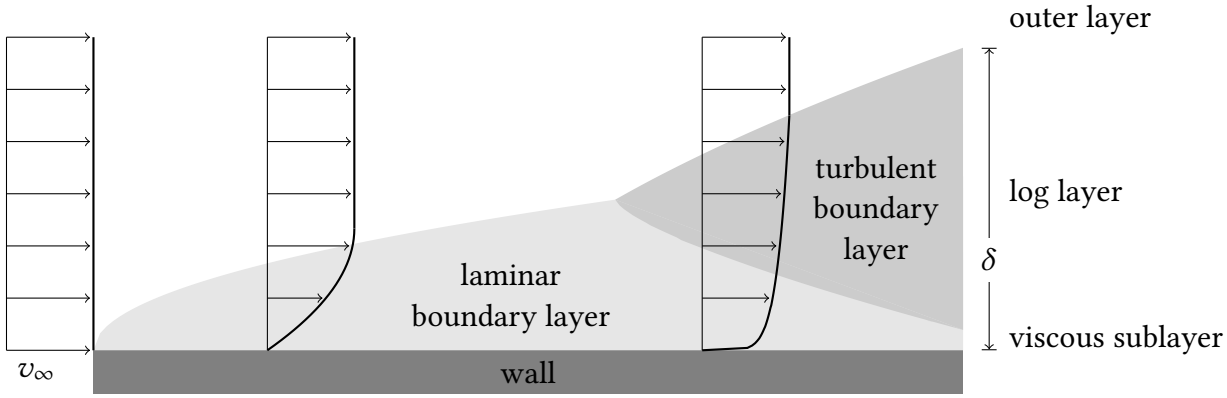

Figure 2.8: Flow alongside a wall results in boundary layers with a thickness δ, defined as the location where the velocity reaches 99% of v_∞.

wall giving off the component's substance. The thermal boundary layer is thinner compared to δ, and the component boundary layer is even thinner [Bird et al., 2007].

The boundary layers play a vital role in the process. Imagine water evaporates in the porous medium, cooler vapor diffuses towards the interface and enters the free flow. Once the boundary layer is cooled and saturated with the component, further evaporation is retarded. The laminar flow limits the turbulent influence from above and it reduces the mixing of the boundary layer fluid with the fluid above. Within the laminar flow of the boundary layer no enhanced mixing takes place.

2.3.3 Evaporation

Evaporation is the conversion from the liquid into the gaseous state. It occurs at the surface between a liquid and a gaseous phase. Molecules of the evaporating substance are crossing the interface in both directions. If the mass fraction of the evaporating substance is low enough in the gaseous phase, more molecules will move from the liquid to the gas. Otherwise, the gas is fully saturated. The evaporation becomes faster in a system with less saturated gas, because less molecules return to the liquid, and in a system with higher temperatures, because molecules have more kinetic energy to leave the liquid. In a closed system, the evaporation ends when the gas is fully saturated with the evaporating substance. The pressure when the gas is fully saturated is called vapor pressure $p^{\mathrm{w}}_{\mathrm{sat}}$ which can be described as a function of temperature [IAPWS, 2007]. In nature, air in the atmosphere is not fully saturated most of the time.

A curved interface between the liquid and the gaseous phase changes the saturated vapor pressure, which is described by the Kelvin equation. This effect occurs inside a porous medium for high capillary pressures. The Kelvin equation can be formulated as

$$p^{\mathrm{w}}_{\mathrm{sat,\,Kelvin}} = p^{\mathrm{w}}_{\mathrm{sat}} \exp\left(\frac{-p_c}{\varrho_{\mathrm{vapor}} R_{\mathrm{s,vapor}} T}\right). \tag{2.25}$$

The effect of the curved interface remains small unless the capillary pressure becomes large. If not stated otherwise, we neglect the effect.

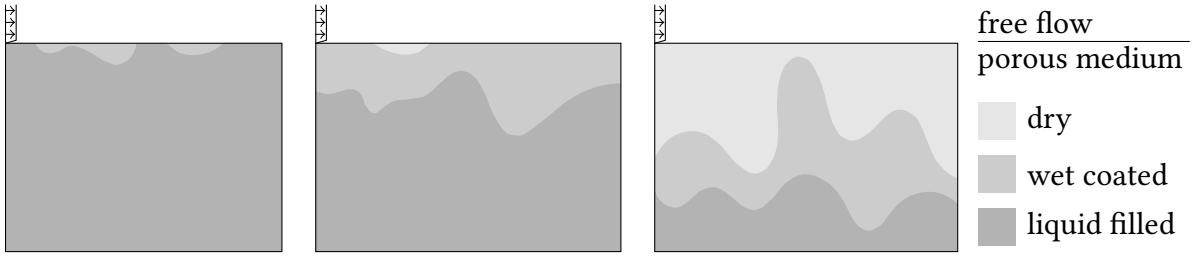

(a) stage 1 (b) stage 2a (c) stage 2b

Figure 2.9: Meaning of evaporation stages for water content in pores next to the interface

Evaporation must not be confused with boiling. Boiling means that the liquid is heated to its boiling point, where the liquid's vapor pressure reaches the pressure imposed from outside the liquid. Bubbles form within the liquid, as this processes happens within the whole liquid. The term vaporization sums up evaporation and boiling.

When a liquid vaporizes, it consumes additional energy to overcome the binding to other molecules. The bindings consist of van der Waals forces, electric dipole moments, et cetera. The amount of energy is called enthalpy of vaporization. Thus, vaporization has a cooling effect.

The opposite process to evaporation is condensation. During condensation, the above process is reversed. Condensation releases the enthalpy of condensation to the surroundings. This enthalpy has the same magnitude as the enthalpy of evaporation, but the opposite direction.

Living plants take water up and cause evaporation of water through their stomata. This is called transpiration. The combination of evaporation and plant transpiration is called evapotranspiration. Drying is the process of reducing the water content in a porous medium. In technical applications, drying is usually done by evaporation with the help of heat or dry air. The porous medium deforms during the process, changing its properties. For example, a shriveled apple has a lower porosity and a different pore size distribution, which influences further drying. We do not consider evapotranspiration or any deformation like shrinking or swelling.

2.3.4 Evaporation of soil water

The not fully saturated air over a water-filled soil drives evaporation directly from the soil to the atmosphere. Next to the soil, the air becomes more humid, retarding the evaporation. A vapor pressure gradient establishes perpendicular to the interface, causing diffusion into the atmosphere. If a wind blows over the soil, it takes the humid air away and the evaporation can materialize at a higher rate.

Eventually, pores run dry, first the smaller ones, and later the larger pores. The envelope of all water-filled pores defines the drying front. Examples are shown in figure 2.9. As mentioned earlier, evaporation takes place at the interface between the phases. Thus, the evaporation happens along the drying front. The cooling effect occurs there, too. With ongoing evaporation, the drying front drops further and it detaches from the interface to the atmosphere. Then the water evaporates completely inside the soil and the vapor is transported by diffusion towards the interface, where the wind takes the vapor away.

The evaporation rate q is the area-related rate of vapor-flow across the interface Γ between the

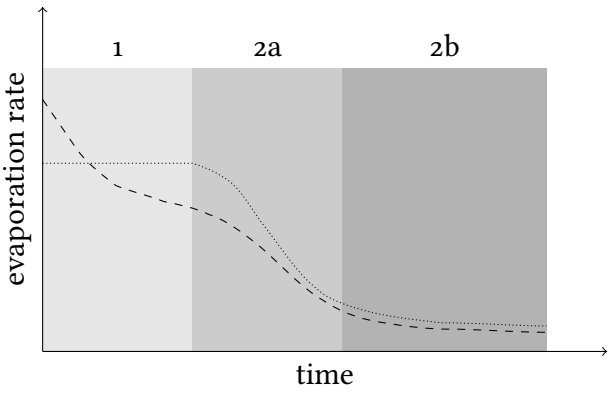

Figure 2.10: Qualitative evaporation rate graphs and characteristic stages of evaporation, dashed: high wind velocity with thin boundary layer, dotted: moderate wind velocity with thicker boundary layer, after Mosthaf et al. [2014]

porous medium and the atmosphere

$$q \coloneqq \frac{1}{|\Gamma|} \int_{\Gamma} \left(X_{\mathrm{g}}^{\mathrm{w}} v_{\mathrm{g}} + \frac{j_{\mathrm{ff}}^{\mathrm{w}}}{\varrho_{\mathrm{g}}} \right)^{\mathrm{ff}} \cdot n \, \mathrm{d}x \tag{2.26}$$

with the advective flux $X_{\mathrm{g}}^{\mathrm{w}} v_{\mathrm{g}}$, the diffusive flux $\frac{j_{\mathrm{ff}}^{\mathrm{w}}}{\varrho_{\mathrm{g}}}$, the normal n with respect to Γ, and the area of the interface $|\Gamma|$. The definition from equation (2.26) considers the interface's free-flow side. An equivalent definition can be formulated from the porous-medium flow side of the interface.

The evaporation rate is a key figure to describe the effect of the occurring evaporation. Plotting the evaporation rate against time results in characteristic graphs [Shahraeeni et al., 2012] similar to the schematic ones in figure 2.10. The velocity of the wind in the atmosphere has a major influence on the evaporation rate in the first stage, because it affects the boundary layer thickness. The graphs have features leading to a classification of different stages of evaporation. In stage 1, water evaporates at a high rate, from water-filled pores next to the interface into the atmosphere. Once the water level has dropped in the last pore at the interface, the vapor diffusion inside the pore towards the interface limits the amount of evaporating water. The evaporation rate falls, stage 2 is reached. [Lehmann et al., 2008, Shahraeeni et al., 2012].

Stage 2 can be split into stage 2a and stage 2b. During stage 2a, the water level drops, but the pores are still coated by water. Through the thin water film, water is transported towards the interface, but to a lesser extent [Yiotis et al., 2007]. By the time all pores at the interface are dried out, stage 2b begins, see figure 2.9. In contrast to other models, like pore network simulations, REV models cannot capture the effect of such water films [Prat, 2002]. We will not take the differences between the stages 2a and 2b into account.

The distinction between the evaporation stages 1 and 2 is important, because different processes dominate the evaporation. In stage 1, the evaporation happens at the interface and the evaporation is mainly affected by the free flow, which carries off the vapor in an advective transport process. The porous medium has a minor influence on the evaporation. In stage 2, the water evaporates at the water table inside the porous medium. Diffusive processes transport the vapor towards the interface; they are limiting the evaporation. The free flow plays a minor role in this stage.

Evaporation rates from lab experiments differ from the ideal one shown in figure 2.10. Mosthaf et al. [2014] discuss reasons for this discrepancy. Soil water evaporation is even more complicated than sketched in this subsection. Shahraeeni et al. [2012] describes several further mechanisms. A review of recent advances regarding this topic is given by Or et al. [2013].

Science is what we understand well enough to explain to a computer. Art is everything else we do.

Donald E. Knuth, 1996

3 Modeling

Partial differential equations (PDE) are a powerful and commonly used tool for the mathematical modeling of flow, or more generally, the modeling of various physical phenomena. First, we will give a brief introduction to PDEs. Second, we will outline the PDEs that describe the motion of fluids, the component transport, the heat equation and how they are linked to each other. Third, we will provide an overview of domain decomposition techniques which are used to combine the different types of flows, and lastly, we will state the conditions we utilize to couple the free flow to the porous-medium flow.

3.0.1 Partial differential equations

A partial differential equation is an equation containing an unknown function w and its partial derivatives. The solution of the PDE is to determine w to fulfill the equation. In general, PDEs can be written as

$$f\left(D^k w(x), D^{k-1} w(x), \dots, Dw(x), w(x), x\right) = 0 \tag{3.1}$$

where D^i is a differential operator of order i and $k \geq 1$ is the order of the PDE. We have PDEs of second order $k = 2$.

The function f is given as a sum of partial derivatives; some summands have a non-linear factor with regard to w. As we have more than one PDE, f becomes a system of PDEs and w is vector-valued. The unknown function $w : U \to \mathbb{R}^n$ with $U \subset \mathbb{R}^m$ is the element of an appropriate function space $W \ni w$, which is of infinite dimension. Usually W is some Sobolev or bounded variational space. Compared to the space of k times differentiable functions C^k, these spaces are richer and contain weakly differentiable functions. This allows for weak solutions of equations that otherwise have indifferentiable kinks or discontinuities, and the weak solutions can be used in the physical problems presented. Our system is transient, i. e., one of the dimensions of U is the time t.

We are only interested in those solutions fulfilling (3.1) which additionally match some boundary conditions on the boundary ∂U and a given initial solution at the initial time t_{init}. The problem of a transient PDE is only completely described when all data like material laws, the boundary and initial conditions are given. A problem is called well-posed, when (i) a solution exists, (ii) it has a unique solution, and (iii) the solution depends continuously on the data. In theory, we don't know if such a solution exists, as according proofs of existence for our complicated systems do not exist yet. On the other hand, in practice, numerical methods give approximated solutions which are useful and provides insight to the applications.

Overall we are facing a non-linear system of PDEs of second order. Some types of second order PDEs are so common that they are named: elliptic, parabolic and hyperbolic. We do not further use this classification, as our equations are not purely of these types. They are advection–diffusion

equations, which are of the form

$$\frac{\partial}{\partial t}\omega - \operatorname{div}(D \operatorname{grad}(\omega)) + \operatorname{div}(v\omega) = 0 \tag{3.2}$$

with the conserved quantity ω, like species concentration or temperature, diffusivity D, and the velocity field of the flow v. The term $\operatorname{div}(D \operatorname{grad}(\omega))$ represents the diffusion, different values of ω lead to a flow to balance the quantity. The term $\operatorname{div}(v\omega)$ represents the advection, driven by an externally driven motion of the fluids carrying ω away.

The most common types of boundary condition are Dirichlet, Neumann and Robin boundary conditions. The Dirichlet boundary condition restricts the solution to some given value $\omega = f_{\mathrm{D}}$ on ∂U. The Neumann boundary condition defines the value of the partial derivative with respect to the boundary normal $n_{\partial U}$ to some given value $\frac{\partial}{\partial n_{\partial U}}\omega = f_{\mathrm{N}}$. The Robin boundary condition is a linear combination of the former two conditions. For given values a, b and f_{R}, it restricts the solution to $a\omega + b\frac{\partial}{\partial n_{\partial U}}\omega = f_{\mathrm{R}}$ on ∂U. At every point along the boundary, one boundary condition must be postulated. It is also possible to have different types of boundary conditions on disjoint parts of the boundary; this is called a mixed boundary condition. The boundary conditions have to fulfill some regularity restrictions.

This subsection is based on Evans [2010] which is recommended for further reading related to the theory of PDEs.

In the following sections, we describe the models for the free-flow and the porous-medium-flow subdomains. We use the same models as the one presented in Mosthaf et al. [2011]. Vanderborght et al. [2017] gives an overview of different modeling concepts for evaporation from soil; Fetzer et al. [2017b] numerically evaluates the consequences resulting from simplifications and parametrizations.

3.1 Free flow

The general model for the motion of a fluid is the Navier-Stokes equation. In the eighteenth's century, ideal fluids were described by the Euler equation, neglecting viscous effects. In the first half of the nineteenth's century, several authors included the viscous term and formulated the Navier-Stokes equation. The mathematical theory evolved and the incompressible, two-dimensional case is well-covered by successful works. But for the incompressible, three-dimensional Navier-Stokes equation, proofs of existence and smoothness are still lacking [Fefferman, 2000].

The Navier-Stokes equation

$$\frac{\partial}{\partial t}\left(\varrho_{\mathrm{g}} v_{\mathrm{g}}\right) + \operatorname{div}\left(\varrho_{\mathrm{g}} v_{\mathrm{g}} v_{\mathrm{g}}^{\mathsf{T}}\right) - \operatorname{div}\left(\mu_{\mathrm{g}} \operatorname{grad} v_{\mathrm{g}}\right) + \operatorname{grad} p_{\mathrm{g}} + \varrho_{\mathrm{g}} g = 0 \tag{3.3}$$

conserves the momentum. The Navier-Stokes equation is vector-valued and can also be regarded as a system of scalar partial differential equations, one for each dimension. The primary variables of the Navier-Stokes equation are the velocities $v_{\mathrm{g},i}$ for the different directions x_i. Compared to the other relevant forces, the gravitational force $\varrho_{\mathrm{g}} g$ is small, due to the low density of the gas. For this reason, the gravitational force's effect in the free flow is neglected.

In the Navier-Stokes equation, the viscosity μ_{g} – or more precisely the reciprocal Reynolds number $1/Re$ – can be interpreted as a weighting factor of the viscous term $\operatorname{div}\left(\mu_{\mathrm{g}} \operatorname{grad} v_{\mathrm{g}}\right)$ relative

to the inertia term $\operatorname{div}\left(\varrho_g v_g v_g^\intercal\right)$. For low Reynolds numbers the inertia effects are dominated from viscous effects and the term can be dropped. The Navier-Stokes equation without the inertia term is called the Stokes equation.

Additionally, the mass conservation is ensured by the mass balance equation

$$\frac{\partial}{\partial t}\varrho_g + \operatorname{div}\left(\varrho_g v_g\right) = 0. \tag{3.4}$$

Here, the primary variable is the pressure p_g. Note that the pressure does not occur in the mass balance equation, because the density ϱ_g is incompressible. Neglecting temperature and component, the mass balance equation can be simplified to $\operatorname{div}(v_g) = 0$. In other words, the mass balance equation ensures that the velocity has zero divergence, thus, the velocity is a solenoidal vector field.

3.1.1 Derivation

Due to the importance of the Navier-Stokes equation for this work, we briefly present its derivation. This derivation, like the whole section about free flow, is based on White [1999].

To obtain the Navier-Stokes equation, we apply conservation laws for mass and momentum to an infinitesimally small control volume V. This volume is a cuboid with sufficiently small edge lengths $\xi_i > 0$ in the x_i direction, see figure 3.1.

Mass balance equation

We observe the flow through the surface ∂V. With small ξ_i, we assume a one-dimensional and orthogonal flow for every face. The inflow in the x_1 direction is $\varrho_g v_1 \xi_2 \xi_3$ and the outflow is $\left(\varrho_g v_1 + \frac{\partial}{\partial x_1}(\varrho_g v_1)\xi_1\right)\xi_2\xi_3$; analog for x_2 and x_3.

In the Reynolds transport theorem

$$\int_V \frac{\partial}{\partial t}\varrho_g \,\mathrm{d}x + \int_{\partial V} \varrho_g (v \cdot n)\,\mathrm{d}x = 0 \tag{3.5}$$

the second term describes inflow and outflow. Replacing these terms with the above flow terms leads to

$$\int_V \frac{\partial}{\partial t}\varrho_g \,\mathrm{d}x + \sum_{i=1}^{3}\left(\varrho_g v_i + \frac{\partial}{\partial x_i}(\varrho_g v_i)\xi_i\right)\frac{\xi_1\xi_2\xi_3}{\xi_i} - \sum_{i=1}^{3}\varrho_g v_i \frac{\xi_1\xi_2\xi_3}{\xi_i} = 0, \tag{3.6}$$

where the first sum is the outflow, and the second sum is the inflow. Because all ξ_i are small, we can approximate

$$\int_V \frac{\partial}{\partial t}\varrho_g \,\mathrm{d}x \approx \frac{\partial}{\partial t}\varrho_g \,\xi_1\xi_2\xi_3 \tag{3.7}$$

and simplify the equation to

$$\frac{\partial}{\partial t}\varrho_g \,\xi_1\xi_2\xi_3 + \sum_{i=1}^{3}\frac{\partial}{\partial x_i}(\varrho_g v_i)\,\xi_1\xi_2\xi_3 = 0. \tag{3.8}$$

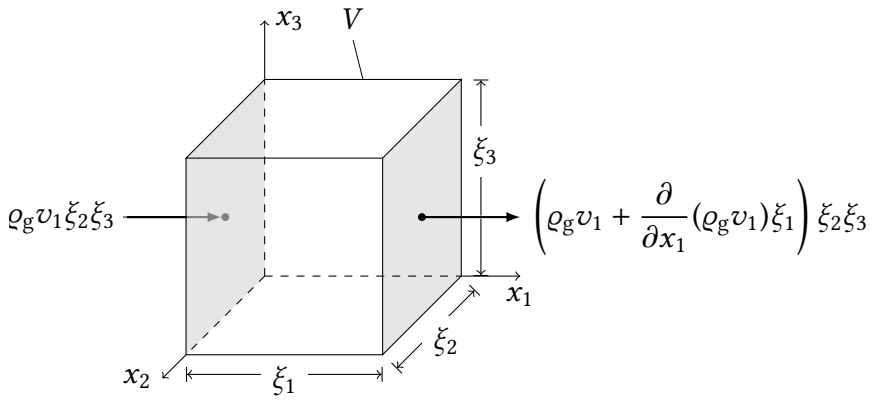

Figure 3.1: Control volume V with inlet and outlet mass flow through the x_1 faces

As all edge lengths ξ_i are positive, we can divide the whole formula by $\xi_1\xi_2\xi_3$, resulting in the equation of continuity

$$\frac{\partial}{\partial t}\varrho_g + \sum_{i=1}^{3} \frac{\partial}{\partial x_i}(\varrho_g v_i) = 0 \tag{3.9}$$

which is (3.4).

Navier-Stokes equation

We can handle the momentum mv for the control volume V in a similar manner. The momentum can be changed by a force $F = \frac{\partial}{\partial t}(mv)$. Newton's second law states that the force F is the same as the acceleration a of mass m, the well-known formula $F = ma = m\frac{\partial}{\partial t}v = m\frac{\partial^2}{\partial t^2}x$.

Two types of forces act on the control volume, body forces and surface forces. External fields like gravitation, electric and magnetic fields cause body forces, which act throughout V. Only the effect of gravity is shown in this derivation,

$$F_{\text{grav},j} = \varrho_g g_j \, \xi_1\xi_2\xi_3 \tag{3.10}$$

for the gravitational acceleration vector $g = (0, 0, -9.81)^\top$ and all spatial directions $j \in \{1, 2, 3\}$.

The stresses at the surface are depicted in figure 3.2a. A stress gradient causes a net force, the surface force is the sum of forces in one direction j, cf. figure 3.2b

$$F_{\text{surf},j} = \frac{\partial}{\partial x_j}\sigma_{jj} \, \xi_1\xi_2\xi_3 + \sum_{\substack{i=1 \\ i\neq j}}^{3} \frac{\partial}{\partial x_i}\sigma_{ji} \, \xi_1\xi_2\xi_3. \tag{3.11}$$

The pressure p and viscous stress forces τ compose the stress $\sigma_i = -p + \tau_{ii}$ which acts across the surface of the control volume ∂V. This leads to

$$F_{\text{surf},j} = \left(-\frac{\partial}{\partial x_j}p + \sum_{i=1}^{3} \frac{\partial}{\partial x_i}\tau_{ji}\right)\xi_1\xi_2\xi_3. \tag{3.12}$$

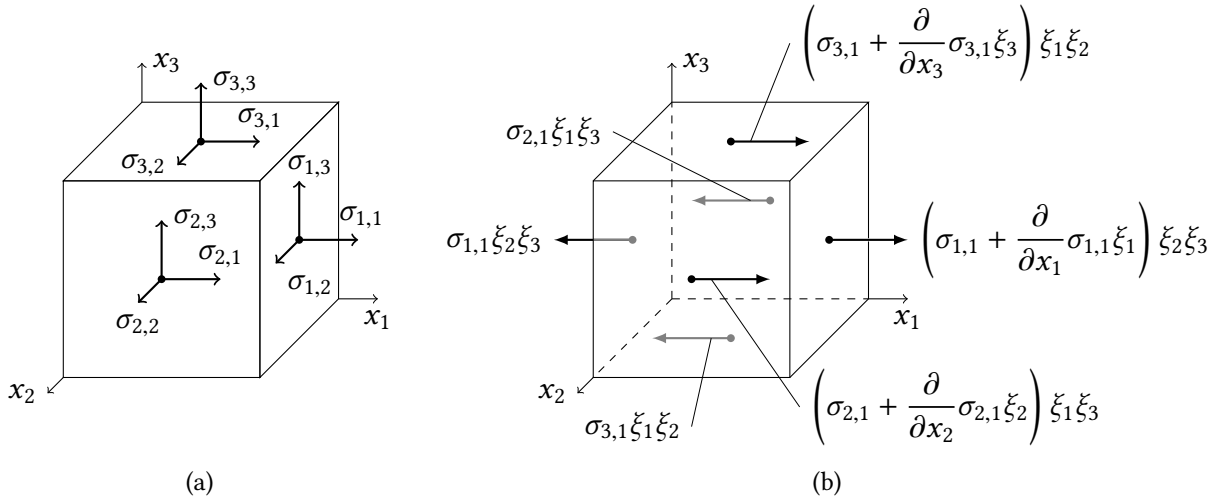

Figure 3.2: (a) Stresses on surface ∂V (b) surface forces in x_1-direction

The total of body and surface force is

$$F_{\text{total},j} = F_{\text{surf},j} + F_{\text{grav},j}. \tag{3.13}$$

We formulate the linear momentum relation for the control volume V similar to the equation of continuity, using the Reynolds transport theorem

$$F_{\text{total},j} = \frac{\partial}{\partial t}\int\limits_V v_j \varrho_\text{g}\,\mathrm{d}x + \sum_{i=1}^{3}\left(\varrho_\text{g} v_i v_j + \frac{\partial}{\partial x_i}(\varrho_\text{g} v_i v_j)\xi_i\right)\frac{\xi_1\xi_2\xi_3}{\xi_i} - \sum_{i=1}^{3}\varrho_\text{g} v_i v_j \frac{\xi_1\xi_2\xi_3}{\xi_i}. \tag{3.14}$$

The last term characterizes the momentum directed outwards, the term before the last one characterizes the momentum directed inwards. We use again the approximation $\frac{\partial}{\partial t}\int_V v_j\varrho_\text{g}\,\mathrm{d}x \approx \frac{\partial}{\partial t}(v_j\varrho_\text{g})\,\xi_1\xi_2\xi_3$ for small ξ_i and get

$$F_{\text{total},j} = \left(\frac{\partial}{\partial t}(v_j\varrho_\text{g}) + \sum_{i=1}^{3}\frac{\partial}{\partial x_i}(\varrho_\text{g} v_i v_j)\right)\xi_1\xi_2\xi_3. \tag{3.15}$$

Using the product rule

$$F_{\text{total},j} = \left(v_j\left(\frac{\partial}{\partial t}\varrho_\text{g} + \sum_{i=1}^{3}\frac{\partial}{\partial x_i}(\varrho_\text{g} v_i)\right) + \varrho_\text{g}\left(\frac{\partial}{\partial t}v_j + \sum_{i=1}^{3} v_i\frac{\partial}{\partial x_i}v_j\right)\right)\xi_1\xi_2\xi_3 \tag{3.16}$$

reveals the first term on the right hand side as the equation of continuity (3.9). We know it to be zero, thus:

$$F_{\text{total},j} = \varrho_\text{g}\left(\frac{\partial}{\partial t}v_j + \sum_{i=1}^{3} v_i\frac{\partial}{\partial x_i}v_j\right)\xi_1\xi_2\xi_3. \tag{3.17}$$

We substitute (3.10), (3.12) and (3.13) in the last equation, divide by $\xi_1\xi_2\xi_3$ and gain the differential momentum equation,

$$\varrho_\text{g} g_j - \frac{\partial}{\partial x_j}p + \sum_{i=1}^{3}\frac{\partial}{\partial x_i}\tau_{ji} = \varrho_\text{g}\left(\frac{\partial}{\partial t}v_j + \sum_{i=1}^{3} v_i\frac{\partial}{\partial x_i}v_j\right) \tag{3.18}$$

for all spatial directions $j \in \{1, 2, 3\}$.

In the considered case of a Newtonian fluid, viscous stresses τ are proportional to the viscosity μ and acceleration:

$$\varrho_\mathrm{g} g_j - \frac{\partial}{\partial x_j} p + \mu \sum_{i=1}^{3} \frac{\partial}{\partial x_i} \left(\frac{\partial}{\partial x_i} v_j + \frac{\partial}{\partial x_j} v_i \right) = \varrho_\mathrm{g} \left(\frac{\partial}{\partial t} v_j + \sum_{i=1}^{3} v_i \frac{\partial}{\partial x_i} v_j \right). \tag{3.19}$$

We shift around some partial derivatives on the left hand side

$$\varrho_\mathrm{g} g_j - \frac{\partial}{\partial x_j} p + \mu \left(\sum_{i=1}^{3} \frac{\partial^2}{\partial x_i^2} v_j + \frac{\partial}{\partial x_j} \underbrace{\sum_{i=1}^{3} \frac{\partial}{\partial x_i} v_i}_{=0} \right) = \varrho_\mathrm{g} \left(\frac{\partial}{\partial t} v_j + \sum_{i=1}^{3} v_i \frac{\partial}{\partial x_i} v_j \right), \tag{3.20}$$

and we identify one sum as the equation of continuity for incompressible fluids. The resulting equation is the same equation as (3.3).

3.1.2 Vapor mass fraction and energy

The vapor in the air is modeled as a component $\kappa = \mathrm{w}$. The transport of vapor mass fraction X_g^w is expressed by the vapor mass fraction balance equation

$$\frac{\partial}{\partial t} \left(\varrho_\mathrm{g} X_\mathrm{g}^\mathrm{w} \right) + \operatorname{div} \left(\varrho_\mathrm{g} X_\mathrm{g}^\mathrm{w} v_\mathrm{g} \right) + \operatorname{div} j_\mathrm{ff}^\mathrm{w} = 0 \tag{3.21}$$

with the primary variable X_g^w. The diffusive component fluxes are $j_\mathrm{ff}^\kappa = -D_\mathrm{g} \varrho_{\mathrm{mole,g}} M^\kappa \operatorname{grad} x_{\mathrm{mole,g}}^\kappa$. As we assume binary diffusion, the choice to have vapor as the transported component $\kappa = \mathrm{w}$ over air as the transported component $\kappa = \mathrm{a}$ is arbitrary.

Non-isothermal processes like heat fluxes are incorporated by the energy transport equation

$$\frac{\partial}{\partial t} \left(\varrho_\mathrm{g} u_\mathrm{g} \right) + \operatorname{div} \left(\varrho_\mathrm{g} h_\mathrm{g} v_\mathrm{g} \right) + \sum_{\kappa \in \{\mathrm{a,w}\}} \operatorname{div} \left(h_\mathrm{g}^\kappa j_\mathrm{ff}^\kappa \right) - \operatorname{div} \left(\lambda_\mathrm{g} \operatorname{grad} T \right) = 0 \tag{3.22}$$

with temperature T as the primary variable. Note that u and h are functions of the temperature. We do not include the effect of viscous dissipation in (3.22), meaning that we do not consider the fluid's kinetic energy that is transformed to thermal energy by internal friction. This effect can be neglected for the involved velocities around $1\,\mathrm{m/s}$ and air, as can be revealed in the following short calculation. Assuming that an air mass m, with a velocity of $v = 1\,\mathrm{m/s}$, dissipates its complete kinetic energy $E = {}^1\!/_2 m v^2 = {}^1\!/_2\,\mathrm{m^2/s^2}\, m$ to thermal energy, using a specific heat capacity for air $c_\mathrm{a} = 1005\,\mathrm{m^2/K\,s^2}$, the resulting temperature increase is $\Delta T = {}^E\!/_{m c_\mathrm{a}} \approx 0.0005\,\mathrm{K}$, which is negligibly small in comparison to other effects.

3.1.3 Boundary conditions

The commonly used boundary conditions for the Navier-Stokes equation deviate from Dirichlet and Neumann boundary conditions. Instead, they represent physical situations and are accordingly

named: Inflow, outflow, wall and symmetry boundary conditions. If a symmetry boundary condition is set, but the flow has no symmetric characteristic, the result becomes unphysical; similar for the outflow boundary condition. Even with the right choice of boundary conditions, they alter the solution in their proximity. As a consequence, the domains do not tightly enclose the region of interest: a startup and a runout section is often included in order to let the flow develop without influence of the inflow boundary condition, and to reduce artifacts from the outflow boundary condition, respectively.

Besides the Dirichlet and the Neumann boundary conditions, we use zero-gradient boundary conditions that demands a zero gradient of the primary variable in the direction normal to the boundary. The zero-gradient boundary condition is routinely used in applied sciences [Versteeg and Malalasekera, 2007] but is seldom mentioned [Chen, 2005, Freund and Stenberg, 1995] or analyzed [Heywood et al., 1996] in mathematical literature. This condition is also called outflow boundary condition.

The boundary conditions representing physical situations are combinations of Dirichlet, Neumann and zero-gradient boundary conditions [Versteeg and Malalasekera, 2007].

For the mass balance equation only two types of boundary equations are needed: Inflow and flux evaluation. The inflow is a Dirichlet boundary condition for the pressure. It is only set together with an outflow boundary condition in the Navier-Stokes equation or for simulations without outflow at one arbitrary spot to fix the pressure. The combination with the former is often called constant pressure boundary condition. The flux evaluation is set everywhere else and is defined by equation (3.4).

Dirichlet and Neumann boundary conditions would suffice to describe all problems for the vapor mass fraction and energy transport, too. For convenience, the boundary condition types from the Navier-Stokes equation are adopted and the boundary conditions are implemented according to their physical meaning. These conditions are only named differently, making the setup of free-flow problems more convenient with the right boundary conditions available. Here, we assume an adiabatic boundary condition for the wall. Other choices are a constant wall temperature or a heat flux through the wall, which would alter the boundary condition.

3.1.4 Turbulence

The direct numerical simulation (DNS) of the Navier-Stokes equation requires small time steps and a fine grid. In many cases, this is not computationally feasible, and the effect of turbulence is approximated on a coarser level.

The shear stress close to a wall leads to boundary layers and influences the perpendicular velocity profile, see figure 2.8. It is computationally expensive to resolve the thin boundary layer with a grid that is refined towards the wall. Near a wall, the general shape of the velocity profile is known to be first linear and then logarithmic. The no-slip condition at the wall is replaced with a known solution one element away from the wall. This is called a wall function for turbulent flow.

To simulate every tiny eddy is disproportionate when only quantitative conclusions should be drawn. In the case of a statistically steady flow, a variable ω can be split into a time-average mean value $\overline{\omega}$ and its fluctuations ω' as $\omega = \overline{\omega} + \omega'$. Applying the splitting to the Navier-Stokes equation results in the so-called Reynolds-averaged Navier-Stokes (RANS) equation. This equation remains similar to the Navier-Stokes equation, but most terms now contain averaged quantities.

As $\overline{\omega'} = 0$, many mixed terms cancel out or can be neglected. The remaining additional mixed term is the Reynolds stress $-\varrho_g \overline{v_1' v_2'}$ which accounts for the fluctuating velocity field. As we want to drop the small-scale variables, the Reynolds stress becomes an additional variable and we have to provide a closing condition for the under-determined system. A way to close the system is to use turbulence models that describe the Reynolds stress. Eddy-viscosity models take the effect of the small-scale turbulence into account by introducing an additional turbulent viscosity μ_t to the averaged Navier-Stokes equation. Algebraic models describe the turbulent viscosity as a function of the wall distance. More sophisticated models like the k-ε or the k-ω models use additional equations to include the kinetic energy k and related variables to describe the generation and the decay of turbulence.

A compromise between the detailed direct numerical simulation and the blurred Reynolds-averaging methods are the large eddy simulations (LES). Smaller eddies and their dissipation are treated in an averaged manner. Larger eddies are simulated directly because they are more energetic and transport more effectively.

More in-depth knowledge concerning wall functions and turbulence models can be found in Ferziger and Perić [2002], Pope [2000] and Wilcox [1998]. The origins, structure and modeling of turbulence remains an active field of research with vivid discussions [Liu et al., 2014, Spalart, 2015, Argyropoulos and Markatos, 2015]. We will not further deal with turbulence models, as Fetzer et al. [2016] already examine the use of different wall functions and turbulence models in a Navier-Stokes/Darcy coupling. Birgle et al. [2017] use a RANS model for the free flow, too.

3.2 Porous-medium flow

When the French hydraulic engineer Henry Darcy planned an improved water supply for his home town Dijon, he experimentally found the linear relationship between the specific discharge and the hydraulic gradient within a sand column [Darcy, 1856], called Darcy's law. Later, his one-dimensional law was generalized to more dimensions, extended to multiple immiscible and miscible flows, and expanded to include energy transport.

In the modern form we want to use, Darcy's law is

$$v_\alpha \coloneqq -\frac{k_\alpha}{\mu_\alpha} k \left(\operatorname{grad} p_\alpha - \varrho_\alpha g\right). \tag{3.23}$$

The specific discharge v_α is the flux per intersection, but for historical reasons, it is called Darcy velocity, or short, velocity. According to Darcy's law, it is proportional to the pressure gradient. The primary condition of Darcy's law is that the flow through the porous media must be creeping, $Re < 1$. After dividing the Darcy velocity by the porosity, we obtain the seepage velocity $\tilde{v}_\alpha \coloneqq \frac{v_\alpha}{\phi}$, which describes the average fluid velocity within the pore space. The continuity equation for hydrodynamics $\phi \frac{\partial}{\partial t} \varrho_\alpha + \operatorname{div}(\varrho_\alpha v_\alpha) = 0$ can be combined with Darcy's law (3.23) to form

$$\phi \frac{\partial}{\partial t} \varrho_\alpha - \operatorname{div}\left(\varrho_\alpha \frac{k_\alpha}{\mu_\alpha} k \left(\operatorname{grad} p_\alpha - \varrho_\alpha g\right)\right) = 0. \tag{3.24}$$

This is the groundwater equation and describes a single-phase Darcy flow in a porous medium. Here, the velocity term is replaced, and the flow is only driven by pressure differences.

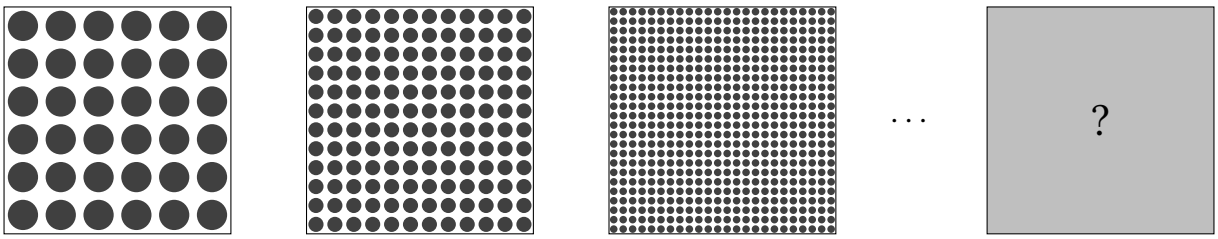

Figure 3.3: The idea of homogenization for an artificial porous medium, after Hornung [2012]

3.2.1 Derivation

For a long time, the theoretical reasoning of Darcy's law was based on averaging with the representative elementary volume (REV) technique. For example, the derivation of a non-isothermal multiphase flow system in a porous medium can be found in Hassanizadeh and Gray [1990].

Homogenization is an alternative approach to averaging. It was developed by mathematicians in the 1980s. One early example can be found in Keller [1980]. Similar to the averaging technique, homogenization can be used to obtain upscaled differential equations from small-scaled ones. Additionally, it can be used for rigorous mathematical proofs. Homogenization requires a scale separation which is not valid in many real-world porous media.

Let w^ε be a family of functions with the parameter $\varepsilon > 0$, which represents a length scale on the micro scale. For a porous medium, the parameter relates to the typical pore size, in the example given in figure 3.3, it describes the diameter of the soil matrix circles. Instead of using a single function, the limit $w \coloneqq \lim_{\varepsilon \to 0} (w^\varepsilon)$ is determined and used as the macroscopic differential function. With other words, we let the microscale tend to zero. The difficulties arise from finding the limit w. Nevertheless, many equations can be derived with the help of homogenization, like Darcy's law, the groundwater equation, its extension to two-phase flow, and thermal flow in porous media. Their derivation is too long and technical for this work, but can be found in Hornung [2012].

3.2.2 Two phases, two components and energy

In this application, we need to model a system with two immiscible phases where each phase has a component consisting of dissolved or evaporated substance from the other fluid. In this case, the groundwater equation lacks descriptive power, and we have to expand it. We begin with a system of two mass balance equations for the components $\kappa \in \{\mathrm{a}, \mathrm{w}\}$

$$\sum_{\alpha \in \{\mathrm{g},\mathrm{l}\}} \left(\phi \frac{\partial}{\partial t} \left(\varrho_\alpha S_\alpha X_\alpha^\kappa \right) - \operatorname{div} \left(\varrho_\alpha X_\alpha^\kappa \frac{k_\alpha}{\mu_\alpha} k \left(\operatorname{grad} p_\alpha - \varrho_\alpha g \right) \right) - \operatorname{div} \left(D_{\mathrm{pm},\alpha} \varrho_{\mathrm{mole},\alpha} M^\kappa \operatorname{grad} x^\kappa_{\mathrm{mole},\alpha} \right) \right) = 0. \tag{3.25}$$

The second term contains Darcy's law, and the third term includes the diffusion aroused by molar mass fraction differences, augmented by effects related to the porous medium.

Adding the two equations (3.25) for $\kappa = \mathrm{a}$ and $\kappa = \mathrm{w}$, together with (2.2) $X_\alpha^\mathrm{a} + X_\alpha^\mathrm{w} = 1$ and the

assumption of binary diffusion, we get the total mass balance equation

$$\sum_{\alpha\in\{\mathrm{g,l}\}} \left(\phi \frac{\partial}{\partial t} \left(\varrho_\alpha S_\alpha \right) - \operatorname{div} \left(\varrho_\alpha \frac{k_\alpha}{\mu_\alpha} k \left(\operatorname{grad} p_\alpha - \varrho_\alpha g \right) \right) \right) = 0. \tag{3.26}$$

Now, we have several options for describing the two-phase Darcy flow. Any two of the three equations (3.25) for $\kappa \in \{\mathrm{a}, \mathrm{w}\}$ and (3.26) suffice as a complete description. We choose the total mass balance and the component balance equation for the vapor component $\kappa = \mathrm{w}$ as it reduces the non-linearity compared to other choices and is convenient for the subsequent coupling.

Our system of equations has the unknowns S_l, S_g, p_l, p_g, and the mass fractions X^w_α. We can express two out of the four unknowns for pressures and saturations with equation (2.18) $S_\mathrm{l} + S_\mathrm{g} = 1$, and the definition of the capillary pressure (2.20) $p_\mathrm{c} \coloneqq p_\mathrm{n} - p_\mathrm{w}$ together with the capillary pressure–saturation relationship determined by Van Genuchten's formula (2.21). All pairs of these variables lead to valid formulations. We use the p_g–S_l formulation, as it is beneficial when the porous medium dries out and the water fluid phase vanishes. See Helmig [1997] for other formulations and their use cases.

The remaining unknown component mass fractions X^w_l and X^w_g can be expressed by primary variables. The mass fraction of dissolved air in water X^a_l can be expressed with Henry's law (2.10) $x^\mathrm{a}_{\mathrm{mole,g}} = \frac{p^\mathrm{a}_\mathrm{g}}{H^\mathrm{a}}$, where the Henry coefficient is computed with (2.11), the conversation from mole fraction (2.4), and the sum of mass fractions (2.2). We calculate the mass fraction of water vapor in air X^w_g with equation (2.9) $x^\mathrm{w}_{\mathrm{mole,g}} = \frac{p^\mathrm{w}_\mathrm{g}}{p_\mathrm{g}}$. If the liquid phase is present, a consequence from the local thermodynamical equilibrium is that the vapor in the air will be fully saturated. From this, we conclude that the partial pressure of the vapor component equals the vapor pressure $p^\mathrm{w}_\mathrm{g} = p^\mathrm{w}_\mathrm{sat}$, where the latter can be calculated as a function of temperature.

When the porous medium dries out, the liquid phase locally vanishes. This phase change simplifies the system, but invalidates the way we calculate X^w_g because the vapor component in air might be no longer fully saturated. We change the primary variable from S_l, which is known to be zero, to X^w_g [Class et al., 2002]. The variables are switched back once the partial pressure of vapor exceeds the vapor pressure $p^\mathrm{w}_\mathrm{g} > p^\mathrm{w}_\mathrm{sat}$. As this is done locally, different formulations can be used at the same time at different regions of the porous medium.

Similar to the free flow, we introduce an additional partial differential equation for the energy transport. It describes the heat transfer in the porous medium and the embedded fluids. Because the flow velocities and the soil grains are small, we can assume local thermal equilibrium, i. e., all fluid phases and the solid have locally the same temperature. Thus, we get a single energy balance equation

$$\sum_{\alpha\in\{\mathrm{g,l}\}} \phi \frac{\partial}{\partial t} \left(\varrho_\alpha S_\alpha u_\alpha \right) + (1-\phi) \frac{\partial}{\partial t} \left(\varrho_\mathrm{s} c_\mathrm{s} T \right) + \sum_{\alpha\in\{\mathrm{g,l}\}} \operatorname{div} \left(\varrho_\alpha h_\alpha v_\alpha \right) - \operatorname{div} \left(\lambda_\mathrm{pm} \operatorname{grad} T \right) = 0 \tag{3.27}$$

with the temperature T as the primary variable. The secondary variables u_α and h_α are functions of the temperature. The first two terms describe the temperature change over time in the fluid phases, and in the soil, respectively. The third term considers the advective energy transport of both phases, it includes the velocity according to Darcy's law. The forth term accounts for the heat conduction within the fluid phases and the porous medium.

3.3 Coupling

The sets of partial differential equations in the two subdomains are still isolated, despite the fact that they are adjoined at the interface. Proper coupling conditions establish the required connection between the properties of both subdomains. For example, the energy transport equations balance temperature differences within the domains; the same must happen across the interface to allow for a similar balancing.

The theory of coupling subdomains arose from the domain decomposition methods which originated nearly 150 years ago [Schwarz, 1870]. Domain decomposition is a technique to analytically solve partial differential equations on domains, which are too complicated to be solved directly. Therefore, the domain is decomposed into several simpler subdomains where solutions can be obtained and combined to get a solution for the whole domain. This approach remains relevant in today's computer-calculated approximations: The solution can be reused for recurring subdomains, meaning that subdomains can be solved more efficiently [Wheeler and Yotov, 1998] or in parallel, and fill-in from direct solvers can be reduced. The domain decomposition methods differ considerably, the most relevant distinctions are iterative and overlapping methods. Iterative methods solve the problem for the subdomain, communicate the result to adjacent subdomains and solve the problem again, until they converge. Some methods require a non-empty overlap between neighboring subdomains, cf. figure 1.5c, which often improves the convergence rate. Many domain decomposition methods can be identified with preconditioners for the linear systems of the discretized and linearized problems [Smith et al., 1996, Toselli and Widlund, 2004, Dolean et al., 2015].

Quarteroni et al. [1992] coined the term heterogeneous domain decomposition for applying domain decomposition methods to coupled problems with different kind of partial differential equations in the subdomains. This is in contrast to the domain decomposition theory above, which has the same partial differential equation on each subdomain. With the heterogeneous domain decomposition, some theoretical considerations and established algorithms can be utilized for coupled problems. One example is the deeper understanding of the coupling conditions. The coupling can be regarded as a Dirichlet-Neumann method, where a Dirichlet and a Neumann boundary problem is solved on the two subdomains adjacent to the coupling interface. The solution of the Neumann boundary problem is the boundary condition of the Dirichlet boundary problem and vice versa. The coupling conditions can be formulated accordingly. It is known that the Dirichlet-Neumann method converges slowly for some problems. The Neumann-Neumann method or the Robin-Robin method show better convergence. One can use this knowledge, formulate the coupling conditions accordingly, and use the faster method [Discacciati et al., 2007]. Heterogeneous domain decomposition highlights two types of applications: One can couple subdomains with inherently different physics like our Navier-Stokes/Darcy coupling, or one can use different models with different degrees of simplifications for the same physics. An example for the latter is Faigle et al. [2015] – they call it model adaptivity – where the surrounding of a subsurface CO_2 injection is modeled with a complex model and the far field with a simpler one. More general, Braack and Ern [2003] present a posteriori control of modeling and discretization errors using model adaptivity. Overlapping methods are also covered by the heterogeneous domain decomposition, e. g., in Discacciati et al. [2016]. In this work, we are only interested in the non-overlapping coupling of different physics.

3.3.1 Coupling conditions

The coupling defines the interplay of related quantities. We have four partial differential equations in the free-flow domain with the primary variables velocities $v_g = (v_1, v_2, \dots)^\intercal$, pressure p_g, vapor mass fraction X_g^w and temperature T, and three partial differential equations in the porous-medium-flow domain with the primary variables gas pressure p_g, a switch variable – in this case either water saturation S_l or vapor mass fraction in the gaseous phase X_g^w – and temperature T. The number of equations and their associated primary variables differ. The counterpart of a variable in the other domain is not obvious. Further difficulties arise from the pressure being of first order in the Navier-Stokes equation, while being of second order in the total mass balance equation in the porous medium.

Coupling conditions can be derived by REV averaging, e. g., Hassanizadeh and Gray [1989a] presents a framework to derive macroscopic coupling conditions from basic principles which is applied to a Stokes/Darcy coupling [Hassanizadeh and Gray, 1989b]. Based on the results from Beavers and Joseph [1967], Saffman [1971], Jäger and Mikelić [2000], and others, Layton et al. [2002] present a set of coupling conditions for single-phase mass and momentum. Mosthaf et al. [2011] extend the coupling conditions to include two-phase compositional Darcy flow and also include interfacial vapor and energy exchange. Fetzer et al. [2016] refines the energy exchange by accounting for diffusive component fluxes.

For the description of the coupling conditions at the interface Γ, we define the normal of the porous medium subdomain with respect to the interface n and the interface tangentials t_i, see figure 3.4a.

The coupling is based on the assumption of local thermodynamic equilibrium and the continuity of fluxes. From these we derive the mechanical, compositional and thermal coupling conditions. They are used as boundary conditions for the respective equations in the subdomains which form the coupling, see the following chapter describing the discretization, especially figure 4.4. An additional boundary condition is necessary for the tangential momentum of the free flow which is provided by the Beavers-Joseph-Saffman condition. The following subsections clarify these coupling conditions.

Mechanical equilibrium

The mechanical coupling is formed by the continuity of total mass fluxes

$$\left(\varrho_g v_g\right)^{\mathrm{ff}} \cdot n = \left(\varrho_g v_g + \varrho_l v_l\right)^{\mathrm{pm}} \cdot n \quad \text{on } \Gamma \tag{3.28}$$

and the continuity of normal stresses

$$n \cdot \left(\varrho_g v_g v_g^\intercal - \mu_g \operatorname{grad} v_g\right)^{\mathrm{ff}} n + p_g^{\mathrm{ff}} = p_g^{\mathrm{pm}} \quad \text{on } \Gamma. \tag{3.29}$$

The continuity of total mass fluxes (3.28) is another name for mass conservation across the interfaces, as it states that the mass leaving one subdomain must entirely enter the other subdomain. The porous medium contains two phases and the liquid phase passing the interface must be considered. We assume that the liquid water does not vanish, but instead, it instantly vaporizes when it reaches the free-flow region.

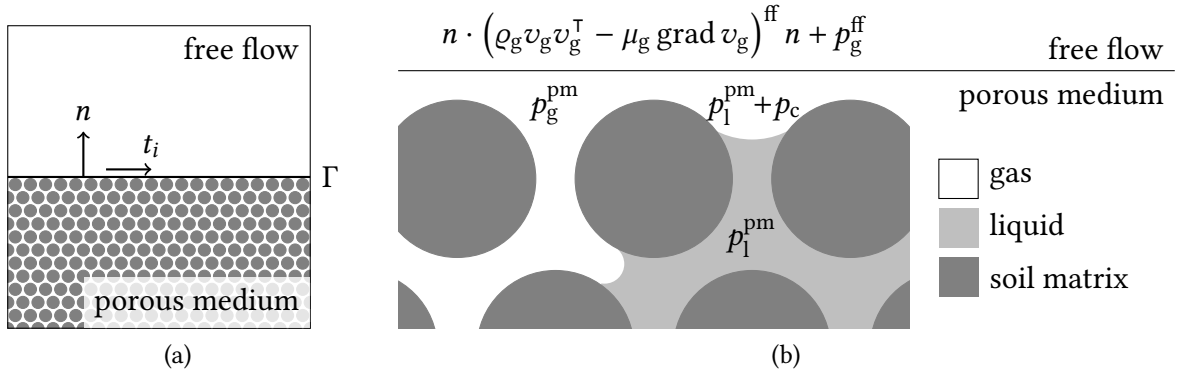

Figure 3.4: (a) Coupling setup with interface Γ, normal n and tangentials t_i (b) Interface condition in the normal direction: the continuity of normal stresses is only the porous gas pressure p_g^{pm} on the porous-medium side of the interface due to the capillary pressure in liquid-filled pores

At first sight, the continuity of normal stresses (3.29) surprises with a jump in gas-pressure at the interface between the subdomains. This is a result of the different models in the subdomains. Instead, we balance the normal stresses or, equivalently, normal forces. The free flow normal stress is $n \cdot \left(\varrho_g v_g v_g^\intercal - \mu_g \operatorname{grad} v_g\right)^{ff} n + p_g^{ff}$. In the porous-medium flow the viscous stresses are implicitly treated by Darcy's law. This leaves only the two phase pressures p_g^{pm} and p_l^{pm} to act on the interface. The capillary effect must be considered for liquid-filled pores and the actual pressure acting on the interface is $p_l^{pm} + p_c$. Depending on the phase presence, only one of the pressures acts at a position $x \in \left\{\xi \in \Gamma | \chi_{pore}(\xi) = 1\right\}$ on the interface, $\chi_g(x) p_g^{pm} + \left(1 - \chi_g(x)\right)\left(p_l^{pm} + p_c\right)$, see also figure 3.4b. With (2.20) and the definition of χ_g, the expression is just p_g^{pm}.

Beavers-Joseph-Saffman condition

A boundary condition for the tangential momenta in the Navier-Stokes equation is necessary. In the early 1960s, it was common to assume no-slip conditions. In their seminal work, Beavers and Joseph [1967] present measurements and conclude to use the Robin boundary condition

$$\left(\alpha_{BJ}\left(v_g^{ff} - \tilde{v}_g^{pm}\right) - \sqrt{k}\ \operatorname{grad} v_g^{ff}\, n\right) \cdot t_i = 0 \quad \text{on } \Gamma \tag{3.30}$$

including the tangential seepage velocity $\tilde{v}_g^{pm} \cdot t_i$ from the porous medium and a slip parameter α_{BJ}. The Beavers-Joseph slip condition leads to a non-zero free-flow velocity tangential to the interface. The use of Robin boundary conditions for the Navier-Stokes equation is not uncommon, as it is also proposed as a way to describe wall functions [Utyuzhnikov, 2008].

In a theoretical analysis, Saffman [1971] simplifies the Beavers-Joseph condition to

$$\left(\alpha_{BJ} v_g^{ff} - \sqrt{k}\ \operatorname{grad} v_g^{ff}\, n\right) \cdot t_i = 0 \quad \text{on } \Gamma, \tag{3.31}$$

arguing that the seepage velocity, in comparison to the free-flow velocity, is small and can be neglected. This is the Beavers-Joseph-Saffman condition and will be used in this work. As a

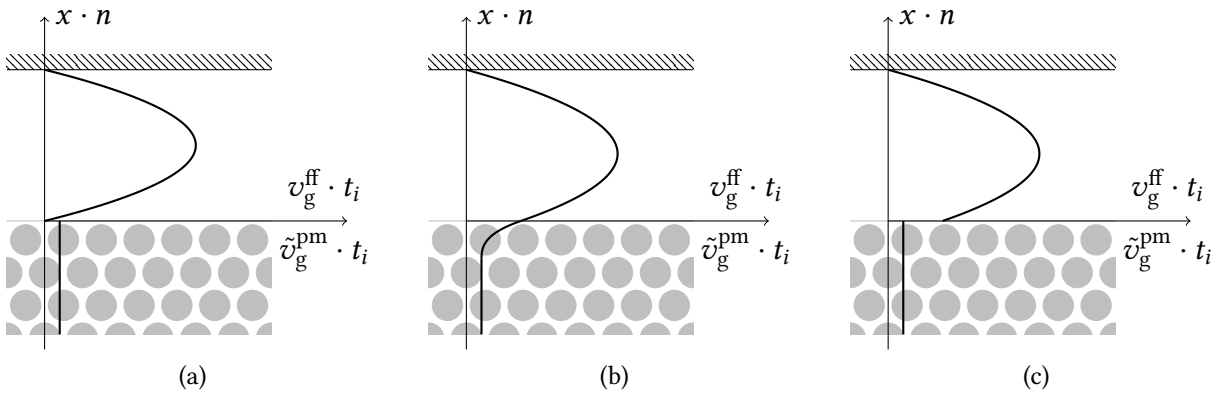

Figure 3.5: Comparison of tangential momentum coupling conditions, the profiles of the tangential velocities are plotted (a) no slip (b) the Beavers-Joseph condition, after Bear [1972] (c) with the Saffman simplification.

consequence of dropping the term $\tilde{v}_g^{pm} \cdot t_i$, this coupling condition is independent of the flow in the porous medium. This makes it a boundary condition with the only remaining link to the porous medium maintained by $\sqrt{k}/\alpha_{BJ}$.

There exist other simplifications of (3.30) in lieu of the one proposed by Saffman. For example, Jones [1973] suggests extending the simple shear velocity $\frac{\partial}{\partial n} v^{ff}$ to the shear stress $\frac{\partial}{\partial n} v^{ff} + \frac{\partial}{\partial t_i} v^{ff}$. Jones' simplification lacks experimental and theoretical backing [Das et al., 2002, Nield, 2009], but is in use.

To compare the different boundary conditions, the effects of the no slip, the Beavers-Joseph condition, and the Beavers-Joseph-Saffman condition are sketched in figure 3.5. The seepage velocity is only altered by the Beavers-Joseph condition, but the effect is exaggerated in the figure for the sake of clarity. For low permeabilities and low porosities, the seepage velocity has a more pronounced kink towards the interface and the free flow influence reaches only a couple of pores deep into the porous medium. For higher permeabilities and higher porosities, when the free flow penetrates the porous medium and causes such high seepage velocities that the flow is no longer creeping, the Beavers-Joseph condition is no longer valid. This can be modeled with Forchheimer flows as shown in De Lemos [2009]. In general, the Beavers-Joseph condition was derived for tangential flow only. A historical overview regarding the Beavers-Joseph condition is given by Nield [2009]. Reviews of alternative coupling approaches without the Beavers-Joseph condition can be found in Alazmi and Vafai [2001] and Furman [2008].

The Beavers-Joseph slip parameter α_{BJ} depends on the porous medium and must be determined experimentally. Beavers and Joseph [1967] report α_{BJ} to be in the range of 0.1 and 4 for their experiments. Some authors rank the influence of the parameter low, but Fetzer et al. [2016] compare $\alpha_{BJ} \in \{0.01, 1, 100\}$ and notice different slip velocities in the order of α_{BJ}. As this affects the boundary layer, it alters the evaporation rate, too. For the setup we have in mind, we lack the data for α_{BJ} and hence stick to $\alpha_{BJ} = 1.0$.

The Beavers-Joseph condition covers only single-phase flows. The case of multiple phases in the porous medium have not been investigated as far as we know. We follow Mosthaf et al. [2011] and assume no slip for water-filled pores, as the viscosity of water exceeds the one of air by two

orders of magnitude. Technically, this introduces a dependency of the water saturation S_l for α_BJ, which we are going to ignore for this work because it has little effect on the evaporation rate [Fritsch, 2016].

Jäger and Mikelić [2000] prove that the Saffman condition is mathematically justified, i. e., the Stokes/Darcy coupling with the Beavers-Joseph-Saffman condition leads to a well-posed problem for the free flow. The proof is based on homogenization and only considers a steady state. Cao et al. [2010] show the same for the Beavers-Joseph condition without the Saffman simplification and also for time-dependent problems.

Compositional equilibrium

Usually the thermodynamic equilibrium contains the chemical equilibrium, which states a locally continuous chemical potential. The chemical equilibrium is defined for a locally constant pressure which is violated by the pressure jump in (3.29). To solve this, we need instead a continuous mass fraction across the interface.

The compositional coupling persists of the continuity of mass fractions

$$X_\mathrm{g}^{\mathrm{w,ff}} = X_\mathrm{g}^{\mathrm{w,pm}} \quad \text{on } \Gamma \tag{3.32}$$

and the continuity of component fluxes

$$\left(\varrho_\mathrm{g} X_\mathrm{g}^\mathrm{w} v_\mathrm{g} + j_\mathrm{ff}^\mathrm{w}\right)^\mathrm{ff} \cdot n = \sum_{\alpha\in\{\mathrm{g,l}\}} \left(\varrho_\alpha X_\alpha^\mathrm{w} v_\alpha - D_{\mathrm{pm},\alpha}\varrho_{\mathrm{mole},\alpha} M^\mathrm{w} \operatorname{grad} x_{\mathrm{mole},\alpha}^\mathrm{w}\right)^\mathrm{pm} \cdot n \quad \text{on } \Gamma. \tag{3.33}$$

As for equation (3.21), the determination to use the vapor mass fraction $\kappa = \mathrm{w}$ is arbitrary, and the diffusive component flux is $j_\mathrm{ff}^\mathrm{w} = -D_\mathrm{g}\varrho_{\mathrm{mole,g}} M^\mathrm{w} \operatorname{grad} x_{\mathrm{mole,g}}^\mathrm{w}$.

Thermal equilibrium

The thermal coupling is simplified by the assumption of local thermal equilibrium within the subdomains. The coupling consists of the continuity of temperature

$$T^\mathrm{ff} = T^\mathrm{pm} \quad \text{on } \Gamma \tag{3.34}$$

and the continuity of heat fluxes

$$\left(\varrho_\mathrm{g} h_\mathrm{g} v_\mathrm{g} + h_\mathrm{g}^\mathrm{w} j_\mathrm{ff}^\mathrm{w} + h_\mathrm{g}^\mathrm{a} j_\mathrm{ff}^\mathrm{a} - \lambda_\mathrm{g} \operatorname{grad} T\right)^\mathrm{ff} \cdot n = \left(\varrho_\mathrm{g} h_\mathrm{g} v_\mathrm{g} + \varrho_\mathrm{l} h_\mathrm{l} v_\mathrm{l} - \lambda_\mathrm{pm} \operatorname{grad} T\right)^\mathrm{pm} \cdot n \quad \text{on } \Gamma. \tag{3.35}$$

Alternative thermal coupling approaches are reviewed in Alazmi and Vafai [2001].

Properties, extensions and assumptions

As the coupling conditions describe the fluxes across the interfaces, the coupling is mass conservative. The coupling interface has no thickness, does not store any quantity, makes no resistance to the normal transport of thermodynamic quantities, and both sides of the interface are in a local thermodynamic equilibrium. Regarding the classification explained in Hassanizadeh and Gray [1989b], we have a simple interface.

The coupling conditions were developed for laminar flow and do not reflect turbulent effects. For porous materials which are 200 times more permeable than ours, an experiment of turbulent flow over a porous bed together with according simulations revealed that the flow characteristics on top of the porous medium is more of a mixing layer than a boundary layer [Prinos et al., 2003]. Hahn et al. [2002] propose different boundary conditions, matching results obtained by a direct numerical simulation. The findings include less friction, a reduction of turbulence, and a thinner boundary layer in some cases. For lower permeabilities, these effects diminish. The turbulent flow does only slightly affect the flow in the porous medium, especially when the results from Chan et al. [2007] are extrapolated for lower permeabilities. De Lemos [2009] simulates turbulent flows both outside and inside the porous medium. The influence of roughness and approaches to model its effect are investigated by Fetzer et al. [2016].

As there is no consensus yet on how to include turbulent effects in the coupling conditions, and primarily low permeabilities and porosities occur in our applications, we do not alter the coupling conditions. As long as the viscous sublayer is above the porous medium, the flow conditions next to the interface remain laminar.

For low permeabilities, it is possible to neglect the pressure jump and the Beavers-Joseph condition altogether. Instead, a continuous pressure and the no-slip condition result in a less difficult coupling. For example, this is done by Masson et al. [2016].

To summarize the underlying assumptions of our model: We assume binary diffusion, following Fick's law, occurs throughout the system, and that all fluids behave as Newtonian fluids, without any dilatation, and further that the system maintains a local thermodynamic equilibrium. We also assume that the free flow consists of a single compositional gaseous phase, that the gases are incompressible, and that we can neglect gravitational forces. We assume that the velocities in the free flow near the interface remain small. Regarding the porous media, we assume that the media has a rigid soil matrix, that flow inside the pores is creeping with $Re < 1$, and that it contains two immiscible compositional phases.

In the good old days physicists repeated each other's experiments, just to be sure. Today they stick to Fortran, so that they can share each other's programs, bugs included.

Edsger W. Dijkstra, 1975

4 Discretization

Compiling all of the previous chapter's equations results in a system of nonlinear partial differential equations (PDE). For certain plain Navier-Stokes or Darcy problems analytic solutions of the resulting systems exist. It would be an involved task to describe the system analytically including various coupled equations and plenty of non-linear, regularized physical relationships. For the coupled one-phase Stokes/Darcy system, problems with known solutions have been constructed, e. g., by Chidyagwai and Rivière [2011], but not for more complicated problems.

Numerical mathematics offers tools to get approximated solutions for these complicated systems. First, we separate time from space and solve them separately; this is called the method of lines [LeVeque, 2002]. Second, we approximate the spatially continuous, time independent problem with a discrete method; we choose the finite volume method (FVM). Third, the time is discretized by an implicit Euler method to obtain a series of spatial discretizations. Fourth, we linearize the discrete problem with Newton's method. Finally, we solve the gained system of linear equations.

The partial differential equations introduced in the last chapter are balance equations of the form

$$\frac{\partial}{\partial t} w - \operatorname{div}\left(f(w)\right) = q \tag{4.1}$$

on a domain Ω. They conserve a quantity w, that can be pressure, momentum or energy, for example. In an integrated form and after applying the divergence theorem, the equation takes the form

$$\int_\Omega \frac{\partial}{\partial t} w - \int_{\partial\Omega} f(w) \cdot n_\Omega = \int_\Omega q. \tag{4.2}$$

and states that the changes of w inside Ω are the normal fluxes over the surface $\partial\Omega$ and the source term q.

4.1 Spatial

To start, we shelve the storage term $\frac{\partial}{\partial t} w$ and discretize the space. We divide the domain Ω into rectangles Ω_i, each called an element or a control volume. They do mutually not overlap or the overlap of two different elements is of co-dimension one. In the latter case it is called a face or an intersection. Equation 4.2 holds true for each element Ω_i. For two adjacent elements, the outflow $\int_{\partial\Omega_i} f(w) \cdot n_{\Omega_i}$ of one element is the inflow of the other element. We replace w by an averaged value $\omega = \frac{1}{|\Omega_i|} \int_{\Omega_i} f(w)$ and keep this value at the center of the element. As the solution w or the discrete solution ω is unknown, it is called a degree of freedom. Instead of calculating the flux between two adjacent elements Ω_i and Ω_j with an integral along their face, the flux is

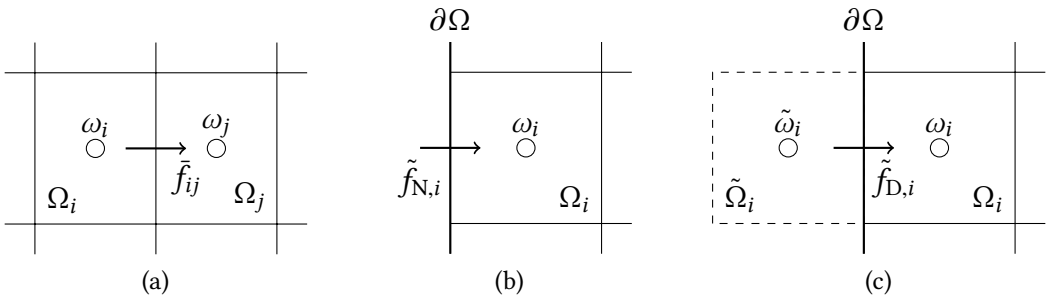

Figure 4.1: Cell-centered finite volume flux (a) between two grid elements (b) for Neumann boundary condition (c) for Dirichlet boundary condition between boundary grid element and ghost element $\tilde{\Omega}_i$

approximated by $\bar{f}_{ij}(\omega_i, \omega_j)$, see figure 4.1a. The numerical flux

$$\bar{f}_{\mathrm{diff},ij}(\omega_i, \omega_j) = \frac{\omega_i - \omega_j}{\left|x_i - x_j\right|} \tag{4.3}$$

with x_i, the location of the degree of freedom in Ω_i, and the Euclidean distance $|\cdot|$, is the most simple approximation for the diffusive parts of f. This numerical flux is called the two-point flux approximation. When discretizing advective terms, that are governed by the velocity v_{ij} at the face, the use of the upwind scheme

$$\bar{f}_{\mathrm{up},ij}(\omega_i, \omega_j, v_{ij}) = \begin{cases} \omega_i & \text{if } v_{ij} \cdot \left(x_i - x_j\right) < 0 \\ \omega_j & \text{else} \end{cases} \tag{4.4}$$

will result in a stable scheme. This can be interpreted physically as the fluid transporting the quantity ω in the direction of the velocity. The upstream value determines the flux across the face.

Instead of writing the flux $\bar{f}_{\mathrm{diff},ij}$ and $\bar{f}_{\mathrm{up},ij}$ between two adjacent elements Ω_i and Ω_j, we sum the fluxes for a singe element Ω_i with respect to all its neighbors N_i as

$$\sum_{j \in N_i} \left(\bar{f}_{\mathrm{diff},ij} \left(\omega_i, \omega_j\right) + \bar{f}_{\mathrm{up},ij}(\omega_i, \omega_j, v_{ij}) \right). \tag{4.5}$$

The finite volume method describes fluxes between the elements. Boundary conditions are incorporated as fluxes over the domain boundary $\partial\Omega$. For Neumann boundary conditions, which specify a flux across $\partial\Omega$, the flux value is implemented as an additional flux $\tilde{f}_{\mathrm{N},i}$ for Ω_i, see figure 4.1b. Dirichlet boundary conditions specify the value of ω at $\partial\Omega$. To fulfill this boundary condition we introduce a ghost element $\tilde{\Omega}_i$ that is mirrored at $\partial\Omega$. The ghost value $\tilde{\omega}_i$ for the ghost element is chosen in such a way, that the linear interpolation between ω_i and $\tilde{\omega}_i$ matches the Dirichlet boundary condition. Then the flux across the boundary $\tilde{f}_{\mathrm{D},i}$ can be evaluated similar to the flux between two inner elements, see figure 4.1c. Robin boundary conditions are a weighted combination of an absolute value of ω and a flux value. In this case, we use a solution-dependent Neumann boundary condition for our implementation. Depending on the current value of ω_i, we calculate the according flux $\tilde{f}_{\mathrm{R},i}$ to match the given boundary condition.

A more extensive description of the finite volume method can be found in books dedicated to this topic, like LeVeque [2002] or Mazumder [2015]. The latter examines all three types of boundary conditions in more detail.

We use the finite volume method to discretize the component transport of the free flow (3.21), the total mass balance equations of the Darcy flow (3.26), the balance equation for the component mass of the Darcy flow (3.25), and the energy transport equations (3.22), (3.27). For all equations we use the same regular rectangular grid. Each grid element has one degree of freedom for each primary variable, and these degrees of freedom coincide in the element's center.

The discretization is implemented in the form of local operators. A spatial local operator adds up all contributions from the equations for a single element, an intersection with the two adjacent elements, or a boundary face with the attached element. The advantage is that the implementation is generic and close to the mathematical formulation. Assembling the global residual can be done in a general way with a grid traversal. On the contrary the concept negatively limits the stencil of the implemented operator, because only variables from neighboring elements can be made dependent.

4.1.1 Navier-Stokes

A similar finite volume discretization for the Navier-Stokes equation (3.3), where the degrees of freedom for velocities are located in the element centers together with degrees of freedom from the mass balance equation (3.4) yields an unstable method. It is easy to construct an example with large, unphysical oscillations like the checkerboard-style pressure solution presented in Versteeg and Malalasekera [2007]. From the theory of finite elements, it is known that the function space representing the velocity must be richer than the one representing the pressure. This is a consequence of stability proofs which involves the inf-sup condition, sometimes called Ladyshenskaja-Babuška-Brezzi (LBB) condition. A common approach which fulfills the inf-sup condition are methods with mixed finite elements. Mixed finite elements have additional degrees of freedom and their normal components are continuous across interfaces [Chen, 2005]. The lowest order case is one degree of freedom in the element center for the pressure, and one degree of freedom per face for the normal velocity component. For rectangular elements, the scheme can be interpreted as a finite difference or finite volume scheme on a staggered grid, then called the marker and cell (MAC) scheme [Harlow and Welch, 1965]. It took almost 30 years to provide the error analysis for this scheme [Nicolaides, 1992, Nicolaides and Wu, 1996]; a more recent proof, provided by Kanschat [2008], interprets the MAC scheme as a Discontinuous Galerkin method. In this work, it is used as a finite volume method, as sketched in figure 4.2: The velocity components are normal to the interface and their degrees of freedom are moved half an element towards the edges of the pressure control volume. All secondary variables, like density or viscosity, do not depend on the velocity and remain in the element centers. With the velocity components at the interfaces, it is natural to use them for the upwind direction at the faces of the primary grid.

For each velocity component, a finite volume discretization on a secondary, staggered grid is constructed. Instead of constructing these grids explicitly, we deduce the geometric information of the secondary elements from the primary grid. For example, the location of the degree of freedom for a normal velocity is a face center in the primary grid.

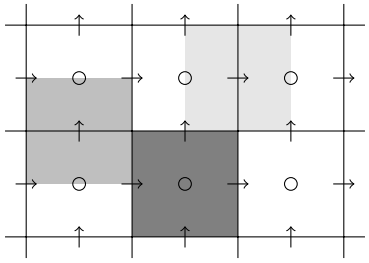

Figure 4.2: Degrees of freedom in the MAC scheme: arrows indicate velocities, circles all other primary variables, gray areas are the corresponding control volumes from the secondary grid, the black lines form the primary grid

4.1.2 Coupling Navier-Stokes and Darcy

During the discretization of the free-flow and the porous-medium-flow regions, the degrees of freedom are located at the element centers, except for those of the free-flow velocities. Instead of having two grids side by side, a single grid is used and cut into two parts along the coupling interface Γ. On one part of the grid, the Darcy flow and the heat equation are approximated, whereas on the other part, the free flow, the component transport, and the heat equation are simulated, see figure 4.3a. At the interface we have to apply the coupling conditions in a discrete form. For the implementation, we use a special local operator, called the coupling operator, which includes two elements sharing the coupling interface as their common face. We have to consider this restriction in our coupling scheme. We already published our coupling scheme in Grüninger et al. [2017], and adopt some paragraphs in the following.

For the Navier-Stokes equation (3.3), the two coupling conditions, continuity of normal stresses (3.29) and the Beavers-Joseph-Saffman condition (3.31), are realized as boundary conditions. In particular, the continuity of the normal stresses (3.29) is a Neumann boundary condition for the normal momentum. The Neumann flux value is the porous medium pressure integrated over the interface. As p_g^{pm} at the interface is not available from the discretization, we use the pressure from the adjacent porous-medium element center. The Beavers-Joseph-Saffman condition (3.31) is a Robin-type boundary condition for the tangential momentum of (3.3). It is implemented as a solution-dependent Neumann boundary condition. The i-th tangential velocity at the interface $v_g^{ff} \cdot t_i\big|_\Gamma =: v_{g,\Gamma,t_i}^{ff}$ is not a primary variable, figure 4.3b shows the position of the tangential velocities. It occurs in (3.31) and we use it for approximating the derivative of the tangential velocity in the normal direction $\operatorname{grad}\left(v_g^{ff}\right) n \cdot t_i \approx \left(v_{g,t_i}^{ff} - v_{g,\Gamma,t_i}^{ff}\right) \frac{2}{\Delta x}$, to get the discrete equation

$$\alpha_{BJ} v_{g,\Gamma,t_i}^{ff} - \sqrt{k}\left(v_{g,t_i}^{ff} - v_{g,\Gamma,t_i}^{ff}\right)\frac{2}{\Delta x} = 0. \tag{4.6}$$

Solving for

$$v_{g,\Gamma,t_i}^{ff} = \frac{2 v_{g,t_i}^{ff}\sqrt{k}}{2\sqrt{k} - \alpha_{BJ}\Delta x}, \tag{4.7}$$

we can calculate the approximation of $\operatorname{grad}\left(v_g^{ff}\right) n \cdot t_i$ which is the Neumann boundary condition for the tangential momentum, because $\varrho_g v_g^{ff} v_g^{ff,\intercal}$ vanishes in the proximity of the interface.

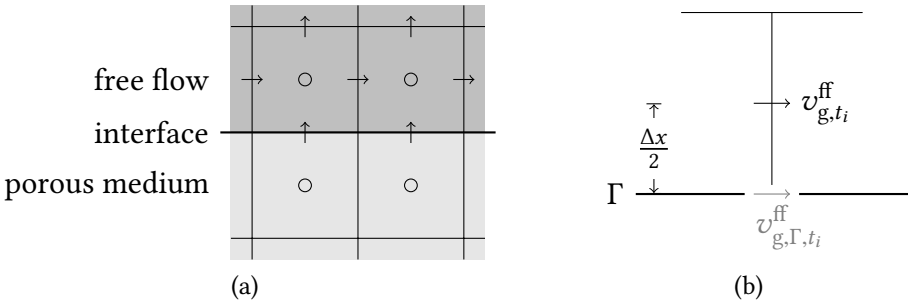

Figure 4.3: Coupling of grid parts discretizing the free and porous-medium flow. (a) A single grid is split at the interface with different discretizations on both subdomains. (b) Tangential velocity at the interface as used by the discretized Beavers-Joseph-Saffman condition.

The free-flow mass balance equation (3.4) requires no coupling condition and the mass flux $\varrho^{\mathrm{ff}}_{\mathrm{g}} v^{\mathrm{ff}}_{\mathrm{g}}$ is calculated on the corresponding finite volume face at the interface.

For the total mass balance equation in the porous-medium subdomain, the continuity of the total mass fluxes (3.28) is used as a Neumann boundary condition. The Neumann flux value is the free-flow momentum $\varrho^{\mathrm{ff}}_{\mathrm{g}} v^{\mathrm{ff}}_{\mathrm{g}} \cdot n$ and resides directly at the interface.

In principle, we would like to apply a standard two-point flux approximation, with harmonic averaging, in order to discretize the continuity of mass fractions (3.32) and the diffusive parts of the vapor component flux (3.33). The latter proves to be difficult due to the different terms occurring on both sides of the equation, especially since direct relationships between the individual terms are unknown. Therefore, we evaluate the free-flow part of (3.33) to calculate the interface flux, which is imposed as a Neumann boundary condition for both component transport equations (3.21) and (3.25). The partial derivative of the vapor component molar mass fraction in the normal direction to the interface is approximated with a finite difference including both values located at the element centers: $\operatorname{grad} x^{\mathrm{w}}_{\mathrm{mole,g}} \cdot n \approx \left(x^{\mathrm{w,ff}}_{\mathrm{mole,g}} - x^{\mathrm{w,pm}}_{\mathrm{mole,g}} \right) \frac{1}{\Delta x}$. The value for the Neumann boundary conditions is calculated as $\varrho^{\mathrm{ff}}_{\mathrm{g}} X^{\mathrm{ff,w}}_{\mathrm{g}} v^{\mathrm{ff}}_{\mathrm{g}} - D^{\mathrm{ff}}_{\mathrm{g}} \varrho^{\mathrm{ff}}_{\mathrm{mole,g}} M^{\mathrm{w}} \left(x^{\mathrm{w,ff}}_{\mathrm{mole,g}} - x^{\mathrm{w,pm}}_{\mathrm{mole,g}} \right) \frac{1}{\Delta x}$.

As for the transport of the vapor component, the same argument is applicable to the energy exchange described by the continuity of temperature (3.34) and the continuity of heat fluxes (3.35). Equation (3.35) contains an additional difficulty: The diffusive terms from the free-flow side $h^{\mathrm{w}}_{\mathrm{g}} j^{\mathrm{w}}_{\mathrm{ff}}$ and $h^{\mathrm{a}}_{\mathrm{g}} j^{\mathrm{a}}_{\mathrm{ff}}$ are incorporated in the porous-medium thermal conductivity λ_{pm} on the other side. As the relationship between the diffusive terms remains unknown, it is not clear how to treat the terms when averaging. Again, the flux is evaluated from the free-flow part of the heat fluxes (3.35) using the approximated gradient across the interface for $\operatorname{grad} T \cdot n$ and $\operatorname{grad} x^{\mathrm{w}}_{\mathrm{mole,g}} \cdot n$.

The relationship between the subdomain equations and their boundary conditions—derived from the coupling conditions—is summarized in figure 4.4.

Alternative coupling discretizations

In Fetzer et al. [2017a], we investigate alternative coupling conditions which have additional degrees of freedom at the interface. The following is a modified excerpt from the publication. The porous-medium pressure $p^{\mathrm{pm},\Gamma}_{\mathrm{g}}$ is not directly used to calculate fluxes inside the porous

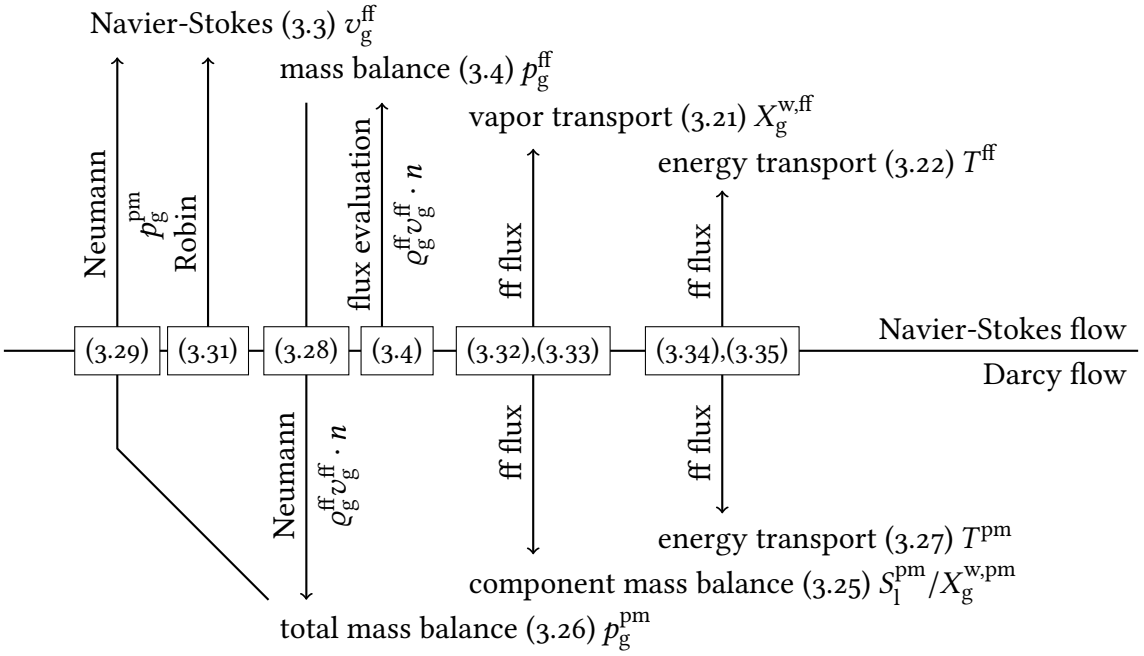

Figure 4.4: Coupling conditions between the subdomain equations with their associated primary variables. Each arrow represents a boundary condition applied to the equation it points at. The two-point flux approximation of the coupling condition's free-flow side is applied to both sides, and is indicated in the diagram by the shorthand *ff flux*.

medium towards the interface. Instead, the mass fluxes entering or leaving the porous medium are specified via the continuity of total mass fluxes (3.28). Regarding the continuity of normal stresses (3.29), both pressures $p_g^{ff,\Gamma}$ and $p_g^{pm,\Gamma}$ are unknown. The position of the pseudo degrees of freedom are shown in figure 4.5a. The pressure values differ due to the different model concepts and the assumption of continuity of normal stresses. Determining $p_g^{pm,\Gamma}$ is necessary to couple the free-flow momentum balance equation with flow processes inside the porous medium.

The simple momentum coupling introduced above assumes $p_g^{pm,\Gamma} = p_g^{pm}$. For a fine enough discretization, this should be a good approximation of the gas pressure at the interface. Coarser grids or higher fluxes lead to an underestimated pressure at the interface, and thus a too low flow resistance at the interface. Further, no pressure can be predicted around corners of the porous media that protrude into the free flow, as depicted in figure 4.5b. We present three different methods to improve the determination of $p_g^{pm,\Gamma}$.

For the total momentum coupling, $p_g^{pm,\Gamma}$ is recalculated using Darcy's law (3.23) and the continuity of total mass fluxes (3.28),

$$\left(\varrho_g v_g\right)^{ff} \cdot n = \left(\sum_\alpha \varrho_\alpha \frac{k_\alpha k}{\varrho_\alpha \nu_\alpha} \left(\frac{p_\alpha^\Gamma - p_\alpha}{(x^\Gamma - x) \cdot n} - \varrho_\alpha g \cdot n \right) \right)^{pm} . \tag{4.8}$$

The liquid saturation $S_l^{pm,\Gamma}$ and thus the liquid pressure at the interface $p_l^{pm,\Gamma}$ are unknown. Therefore, no difference in the liquid phase saturation is assumed, $S_l^{pm,\Gamma} = S_l^{pm}$. This simplification results in the same pressure difference for both phases $p_l^{pm,\Gamma} - p_l^{pm} = p_g^{pm,\Gamma} - p_g^{pm}$ and therefore

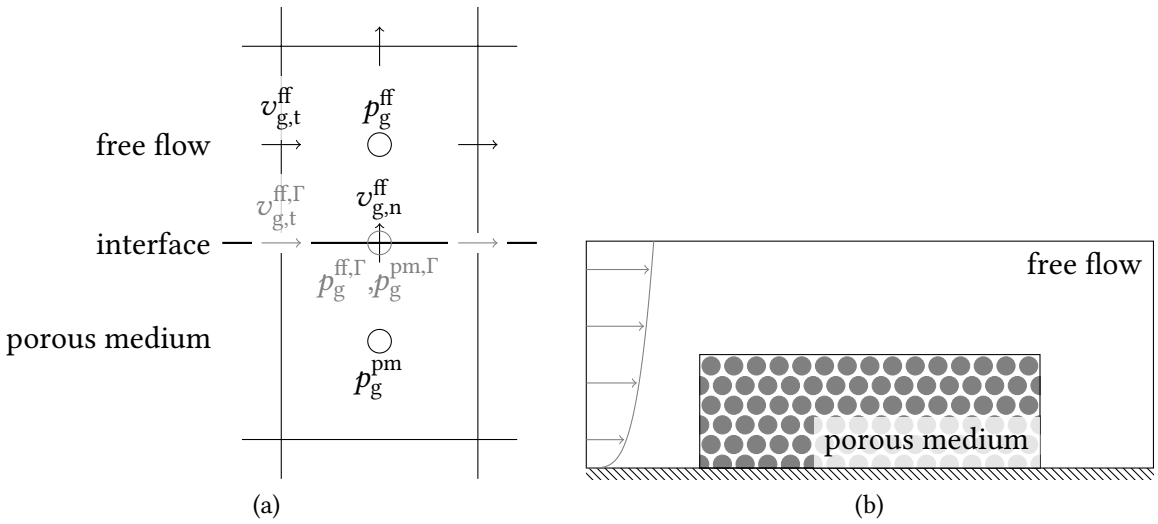

Figure 4.5: Alternative coupling discretizations (a) Location of degrees of freedom and pseudo degrees of freedom at the coupling interface, the latter have the superscript Γ and are printed in gray. (b) When the porous medium extends into the free flow, the flow through the porous medium might becomes unphysical, especially at the corners.

the gradients contributing to the liquid and gas phase flux are equal. With that, we calculate the interface gas pressure as

$$p_g^{pm,\Gamma} = \frac{\left(\varrho_g v_g \cdot n\right)^{ff} + \left(\sum_\alpha \frac{k_\alpha k}{\nu_\alpha} \varrho_\alpha g \cdot n\right)^{pm}}{\sum_\alpha \frac{k_\alpha k}{\nu_\alpha}} \left(x^{pm,\Gamma} - x^{pm}\right) \cdot n + p_g^{pm}. \tag{4.9}$$

When we neglect gravitational forces, the porous medium and its discretization are given. With this, the lowest gas pressure and highest gas velocity along the interface occur in areas of small flow resistances $\left(\sum_\alpha {}^{k_\alpha}/_{\nu_\alpha}\right)^{-1}$ which are found at $S_l = 1$.

For the gas momentum coupling approach, the free flow gas is not allowed to transfer momentum to the liquid phase. This means the liquid terms in (4.9) are dropped and the gas pressure at the interface becomes

$$p_g^{pm,\Gamma} = \frac{\left(\varrho_g v_g \cdot n\right)^{ff} + \left(\frac{k_g k}{\nu_g} \varrho_g g \cdot n\right)^{pm}}{\frac{k_g k}{\nu_g}} \left(x^{pm,\Gamma} - x^{pm}\right) \cdot n + p_g^{pm}. \tag{4.10}$$

As opposed to the first alternative approach, a fully liquid saturated system acts as an impermeable barrier. No additional assumptions about the liquid state have to be made. Now, the lowest resistance $\left({}^{k_g}/_{\nu_g}\right)^{-1}$ and thus the highest velocities occur for $S_l = 0$.

To make as few assumptions concerning interface conditions as possible, we present the coupling via an interface solver. For each primary variable, we introduce a pseudo-unknown at the interface. These pseudo-unknowns are $p_g^{pm,\Gamma}$, $X_g^{w,ff,\Gamma}$, $S_l^{pm,\Gamma}$ or $X_g^{w,pm,\Gamma}$, $T^{ff,\Gamma}$, and $T^{pm,\Gamma}$. Assuming local thermodynamic equilibrium, two of them can be eliminated: $X_g^{w,ff,\Gamma} = X_g^{w,pm,\Gamma}$, or $X_g^{w,ff,\Gamma} = f\left(S_l^{pm,\Gamma}, p_g^{pm,\Gamma}\right)$, and $T^{ff,\Gamma} = T^{pm,\Gamma}$. The three necessary equations are (3.28), (3.32) and

(3.35). In contrast to the above mentioned assumptions, $S_\mathrm{l}^{\mathrm{pm},\Gamma} = S_\mathrm{l}^{\mathrm{pm}}$ is no longer required. This means the pressure gradients of the liquid and of the gas phase might differ. Further, the gradients driving the diffusive and conductive fluxes can now be built without using quantities from the other subdomain. The diffusive fluxes in (3.32) and (3.35) can be expressed by

$$j_\alpha^\kappa = -D_\mathrm{g}\, \varrho_{\mathrm{mole,g}} M^\kappa \frac{x_\alpha^{\mathrm{w},\Gamma} - x_\alpha^{\mathrm{w}}}{(x^\Gamma - x)\cdot n}, \tag{4.11}$$

the conductive fluxes in (3.35) are given by

$$-\lambda_\mathrm{g}\, \mathrm{grad}\, T = -\lambda_\mathrm{g} \frac{T^\Gamma - T}{(x^\Gamma - x)\cdot n} \tag{4.12}$$

for both subdomains. To calculate the fluxes across the interface, this system of equations has to be solved with Newton's method. If the method has converged, the pseudo-unknown $p_\mathrm{g}^{\mathrm{pm},\Gamma}$ is used to calculate all fluxes. In comparison to all previous coupling methods, this method is able to consider co-current flow of liquid and gas for estimating the normal momentum flux and thus the interface gas pressure.

We will not use these alternative approaches in this work as the simple method works for our applications [Grüninger et al., 2017] and does converge for finer grid cells [Fetzer et al., 2017a].

4.2 Temporal

Using the finite volume method to discretize the space, we have a system of semi-discrete equations of the form

$$\frac{\partial}{\partial t}\omega_i + \sum_{j\in N_i} \left(\bar{f}_{\mathrm{diff},ij}\left(\omega_i, \omega_j\right) + \bar{f}_{\mathrm{up},ij}\left(\omega_i, \omega_j, v_{ij}\right)\right) = 0 \tag{4.13}$$

for each element Ω_i. This is a system of ordinary differential equations (ODE) with respect to the time t. The continuous time is replaced by discrete points called time steps t^k with $t^0 < t^1 < \ldots < t^{\mathrm{end}}$ where the time step size is defined as $\Delta t^k := t^k - t^{k-1}$. The superscript on any variable indicates, that the value is evaluated at the time step with the same index, for example, $\omega^k := \omega|_{t^k}$. The time step size is determined adaptively depending on the number of Newton steps. The time step size cannot grow beyond a maximum time step size $\Delta t^{\max}$ that is given as a parameter. If the time step size falls below a given minimum, the simulation aborts.

The partial derivative in the storage term is approximated with a backward finite difference

$$\frac{\omega_i^k - \omega_i^{k-1}}{\Delta t^k} + \sum_{j\in N_i} \left(\bar{f}_{\mathrm{diff},ij}\left(\omega_i^k, \omega_j^k\right) + \bar{f}_{\mathrm{up},ij}\left(\omega_i^k, \omega_j^k, v_{ij}^k\right)\right) = 0. \tag{4.14}$$

This is called the backward Euler method, which is an implicit method because the solution for the new time step ω_i^k cannot be calculated directly from local data using the last time t^{k-1}. All variables build a nonlinear system that must be solved. The implicit Euler method has the largest stability region of all the ODE solvers, in particular as it is L-stable [LeVeque, 2002]. The method does not impose any restriction on the time step size.

4.3 Linearization

Let u_ω be a vector for all degrees of freedom with u_{ω_i} as the degree of freedom for ω from the i-th grid element Ω_i. Further, let u be the vector for all degrees of freedom for all primary variables from both subdomains

$$u \coloneqq \left(u_{v_{1,\mathrm{ff}}}, u_{v_{2,\mathrm{ff}}}, \ldots, u_{p_{\mathrm{ff}}}, u_{X_{\mathrm{ff}}}, u_{T_{\mathrm{ff}}}, u_{p_{\mathrm{g,pm}}}, u_{s_{\mathrm{pm}}}, u_{T_{\mathrm{pm}}}\right)^\mathsf{T}. \tag{4.15}$$

Equation (4.14) postulates the property of the balance equation in a discrete way: the change over time, the flux over the faces, and contribution from sources must add up to zero. Using the right hand side of the equation, we define the element residual

$$r_i\left(\omega_i^{k-1}, \omega_i^k\right) \coloneqq \frac{\omega_i^k - \omega_i^{k-1}}{\Delta t^k} + \sum_{j \in N_i} \left(\bar{f}_{\mathrm{diff},ij}\left(\omega_i^k, \omega_j^k\right) + \bar{f}_{\mathrm{up},ij}\left(\omega_i^k, \omega_j^k, v_{ij}^k\right)\right) \tag{4.16}$$

and the residual $r\left(u^{k-1}, u^k\right)$ with the entries $r\left(u^{k-1}, u^k\right)_i \coloneqq r_i\left(u_i^{k-1}, u_i^k\right)$. The residual indicates the quality of u^k as an approximation for the discrete system. For zero entries, it is a perfect approximation. For small entries, the approximation can be good enough. For large absolute values, it is clearly not a suitable approximation.

We use Newton's method: From an approximation of the solution $u^{k,l}$, we calculate the Jacobian matrix for the residual

$$J_r\left(u^{k-1,l}, u^{k,l}\right) \coloneqq \left(\frac{\partial}{\partial u_j^{k,l}} r\left(u_i^{k-1,l}, u_i^{k,l}\right)\right)_{i \in \{1,\ldots\}, j \in \{1,\ldots\}}. \tag{4.17}$$

The Jacobian matrix' entries are partial derivatives with respect to all unknowns; they describe how the value of an unknown is influenced by other unknowns. By solving the linear system

$$J_r\left(u^{k-1,l}, u^{k,l}\right) z^{k,l} = u^{k,l}, \tag{4.18}$$

we obtain the update vector $z^{k,l}$. The next approximation of the solution is

$$u^{k+1,l} = u^{k,l} - z^{k,l}. \tag{4.19}$$

The Newton step is then repeated until the approximation is sufficient. For linear problems only a single Newton iteration must be performed.

There are several possibilities to measure the quality of the current approximation: the difference of two subsequent solutions $\left\|u^{k+1,l} - u^{k,l}\right\| = \left\|z^{k,l}\right\|$, the size of the residual $\left\|r\left(u^{k-1}, u^k\right)\right\|$, the reduction of the residual's size compared to the initial residual's size $\frac{\left\|r\left(u^{k-1}, u^k\right)\right\|}{\left\|r\left(u^0, u^1\right)\right\|}$, or the maximum of all residual entries $\max_i\left(r_i^k\right)$. Here, a combination of the last two is used: The Newton's method finishes successfully when either the residual reduction is lower than 10^{-7} or the maximum entry is smaller than 10^{-5}. Depending on the simulation, other values are more suitable.

The number of Newton iterations ζ^k until the method finished successfully is used to adapt the next time step size Δt^{k+1}. A simulation parameter is the target number of Newton iterations ξ. If

the number of iterations remain below the target number $\zeta^k < \xi$, the time step size is increased to $\Delta t^{k+1} = \Delta t^k \left(1 + \frac{\xi - \zeta^k}{1.2\xi}\right)$. If the number of iterations exceed the target number $\zeta^k > \xi$, the time step size is reduced to $\Delta t^{k+1} = \Delta t^k \left(1 + \frac{\zeta^k - \xi}{\xi}\right)^{-1}$. If the Newton method does not converge, we half the time step size and restart the Newton method. We do the same if non-physical values like a negative saturation appears or if solving the linear system fails.

4.4 Solving the system of linear equations

Each Newton iteration performs the assembly of the Jacobian and the solution of a large system of linear equations. To simplify the notation from (4.18), we use $Az = b$. For the examples in this work, the number of unknowns η in the system lies in the range of 10 000 to 100 000. The upper limit is marked by the available computer hardware and computing time. Solving this linear system is computationally expensive.

The matrix A is sparse; in other words, most of its entries are zero and the number of nonzero entries is of linear complexity $O(\eta)$ instead of the possible quadratic complexity $O\left(\eta^2\right)$. This structure can be exploited to solve the system faster. Depending on the numbering of the degrees of freedom, the nonzero entries are usually along the diagonal in a structure of bands, see figure 4.6 for an example. The matrix is nonsymmetric.

The discretizations of the two coupled subdomains are visible in the block structure of A, with the free-flow part in the upper left and the porous-medium-flow part in the lower right. Both parts are only coupled with few entries in the large off-diagonal blocks. For two-dimensional problems, the number of nonzero entries in the off-diagonals is $O\left(\sqrt{\eta}\right)$ and $O\left(\eta^{2/3}\right)$ for three-dimensional ones.

One submatrix is of special interest because it differs from the others and requires special care in the process of solving the overall linear system. The linearized system for the incompressible Navier-Stokes equation (3.3) and the mass balance equation (3.4) forms a saddle point problem of the type

$$\begin{pmatrix} \bar{A} & B \\ C & 0 \end{pmatrix}. \tag{4.20}$$

For symmetric problems $\bar{A}$ is symmetric and $B = C^\intercal$. The zero block is caused by the assumed incompressibility of the fluids. It is common to refer to a saddle point problem as nonsymmetric or generalized, if $\bar{A}$ is not symmetric, but $B = C^\intercal$ remains [Bramble et al., 2000, Krzyzanowski, 2001]. Such problems arise amongst others from discretizations of mixed finite elements. From our problem, we get even less symmetric linear systems, as $\bar{A}$ is not symmetric and additionally $B \neq C^\intercal$. Saddle point problems are hard to solve, most iterative algorithms, which are well-suited for other types of matrices, break down or show poor convergence. Standard iterative methods developed for saddle point problems, like the Uzawa algorithm [Chen, 2005], only work for symmetric matrices. Benzi et al. [2005] thoroughly deal with saddle point problems, partially also with nonsymmetric ones. Most algorithms are not directly applicable and there is no obvious ready-to-use linear solver, beside direct methods.

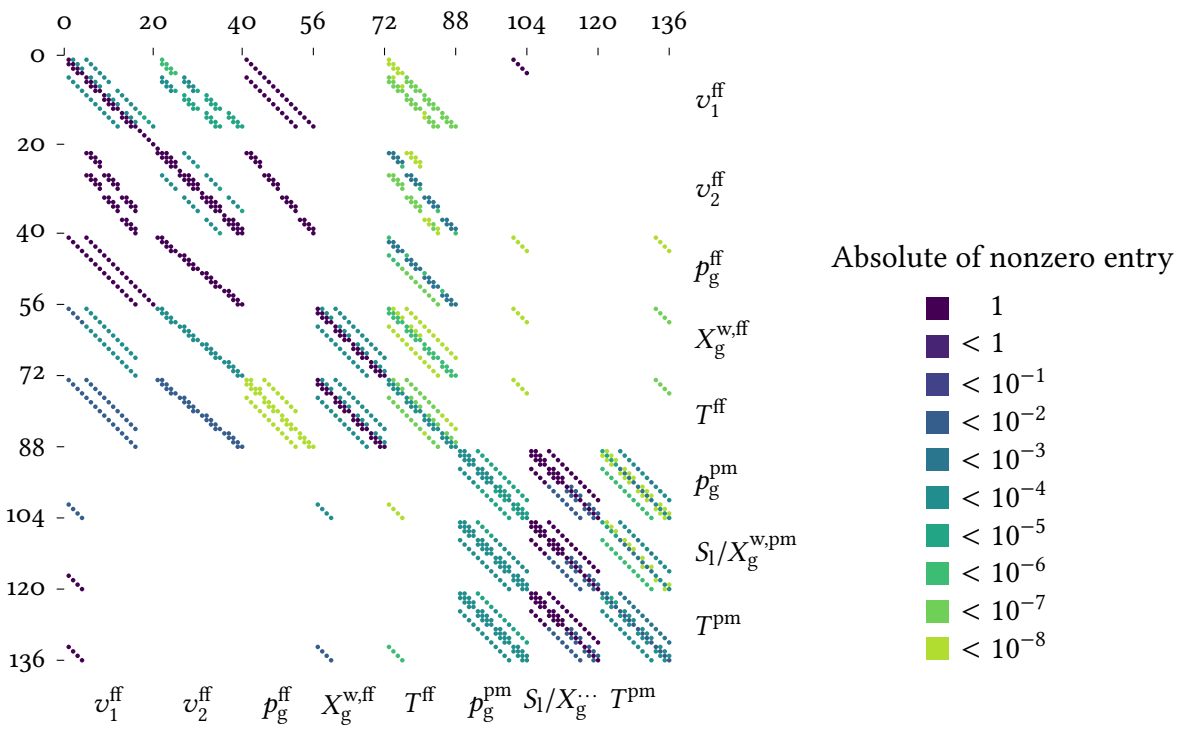

Figure 4.6: Structure of an exemplary matrix obtained from a discretization of a coupled system with 4×4 elements per subdomain, row-scaled for visualization; the number of nonzero entries is 1541, the original condition number was $1.2 \cdot 10^{12}$; visible are the block structure, the saddle point problem in the v^{ff} and $p_{\mathrm{g}}^{\mathrm{ff}}$ blocks, the nonsymmetry like the blocks for $p_{\mathrm{g}}^{\mathrm{ff}}$ and T^{ff}.

4.4.1 Direct linear solvers

Gaußian elimination is a numerically robust algorithm for solving a system of linear equations. It directly solves the linear system. It has a large memory footprint and, if naïvely implemented, its computational complexity is cubic $O\left(\eta^3\right)$. If the band structure with the band width ω is exploited, it can be reduced to $O\left(\omega\,\eta^2\right)$. The idea is to eliminate the entries below the diagonal for each row i by adding multiples of the i-th row. The resulting system with an upper right matrix is solved by backward substitution. The method is prone to fill-in, which is a phenomenon of initially zero entries becoming nonzero during the elimination of entries further left. Fill-in can be reduced by reordering the degrees of freedom. We use two different direct linear solvers, UMFPack [Davis, 2004] and SuperLU [Demmel et al., 1999]. Both compute an LU decomposition $A = LU$ with L an lower triangular matrix and U an upper triangular matrix where L stores the coefficients of the elimination procedure. The two algorithms try to identify or to create dense blocks which are independent from other parts of the matrix and can be solved fast with BLAS routines. UMFPack is a multifrontal method, i. e., dense submatrices are created for the parts where the factorizing is active, while the submatrices are related by an elimination tree. SuperLU uses supernodes which are adjacent columns with the same zero pattern. We refer to Davis et al. [2016] for an explanation of similarities and differences between the algorithms.

Multithreaded algorithms like SuperLU_MT open up the computational power of multiple threads without requiring multiple copies of the matrix, but their capability to so solve large systems is bound by their high memory usage. Initially, the use of graphics processing units (GPU) for direct linear solvers has not shown good results [Vuduc et al., 2010], but promising algorithms were published in the last couple of years [Davis et al., 2016]. The use of multi-core parallel direct solvers which distribute the problem over several nodes and communicate intermediate results between the nodes is out of this work's scope. It could be beneficial when the grid and the matrix assembly are already distributed. Recent advances in sparse direct solvers like memory-aware scheduling techniques, low-rank approximations, and distributed/shared memory hybrid programming are covered in Agullo et al. [2013] and Davis et al. [2016]. There is no specialized direct solver for saddle point problems [Benzi et al., 2005].

4.4.2 Iterative linear solvers

Iterative methods for linear systems generate sequences of approximations which converge towards the solution. A single iteration typically requires one or more matrix-vector multiplications as the most expensive operation. For sparse matrices, this is of linear complexity $O(\eta)$. For large matrices, good iterative methods outperform direct solvers because the number of iterations needed for convergence grows only moderately when η is increased. Numerous iterative methods are published; the book Saad [2003] gives an excellent overview of iterative methods for sparse linear systems. Unfortunately only few methods can be used for nonsymmetric saddle point problems. Two common iterative Krylov subspace methods, suitable for nonsymmetric systems, are the Generalized Minimal Residual method (GMRES) with restarts and the Bi-conjugate Gradient stabilized method (BiCG-stab).

GMRES minimizes in the i-th step the residuum's Euclid norm $\|Az - b\|_2$ with respect to an affine Krylov subspace $z_0 + \text{span}\left(\left\{r_0, Ar_0, A^2r_0, \ldots, A^{i-1}r_0\right\}\right)$, with the initial solution z_0 and the initial residual $r_0 \coloneqq Az_0 - b$. The construction of the Krylov subspace requires to construct orthonormal basis vectors. To reduce the effort, restarts are used which dismiss all base vectors and start with a new, empty Krylov subspace. With exact arithmetic and without the restarts, GMRES is a direct method and yields a solution after η iterations. It is commonly used as an iterative method with an adequate preconditioner, with far less than η steps, and with restarts after every 20 to 40 iterations.

The conjugate gradient method minimizes $1/2\, z^\intercal Az - bz$ which is equivalent to solving the original linear system. The gradient for the minimization problem at z_i is $-r_i \coloneqq Az_i - b$. Instead of directly using a gradient descent, the conjugate gradient is used, meaning that the directions of the descent d_i are conjugated and for all $i \neq j$ it holds that $d_i^\intercal Ad_j = 0$. One generalization for nonsymmetric matrices is the Biconjugate Gradient (BiCG) method which involves $A^\intercal$. As the resulting method is unstable, BiCG-stab performs a single GRMES iteration for stabilization after every BiCG iteration. Again, this method is commonly combined with a preconditioner.

To improve the convergence of iterative methods a preconditioner P is multiplied from left and the iterative method is applied to $PAz = Pb$ instead. The preconditioned system should converge faster compared to the original one. An ideal preconditioner would be $P = A^{-1}$ but obviously such a preconditioner is difficult to obtain. A preconditioner can be constructed from a simplification of A which can be cheaply inverted. An example is the diagonal matrix D_A which provides

the Jacobi preconditioner D_A^{-1}. Here, preconditioners can be based on two approaches: Purely algebraic techniques or methods incorporating knowledge about the structure of the problem and its discretization.

Problem-specific preconditioners

In many applications, the block structure of a saddle point problem can be utilized to construct efficient methods. The problem at hand has even more structure as the coupling leads to almost empty off-diagonal blocks.

We rewrite $Az = b$ in a blocked form—which must not be confused with the saddle-point structure given in equation (4.20)—as

$$\begin{pmatrix} \bar{A} & B \\ C & D \end{pmatrix} \begin{pmatrix} z_1 \\ z_2 \end{pmatrix} = \begin{pmatrix} b_1 \\ b_2 \end{pmatrix} \tag{4.21}$$

with $\bar{A} \in \mathbb{R}^{\eta_1 \times \eta_1}$, $D \in \mathbb{R}^{\eta_2 \times \eta_2}$, and $\eta = \eta_1 + \eta_2$. Multiplying the upper row from left by $-C\bar{A}^{-1}$ gives $-Cz_1 - C\bar{A}^{-1}Bz_2 = -C\bar{A}^{-1}b_1$. Adding it to the lower row results in

$$\left(D - C\bar{A}^{-1}B\right) z_2 = b_2 - C\bar{A}^{-1}b_1, \tag{4.22}$$

where $S \coloneqq D - C\bar{A}^{-1}B$ is the Schur complement of $\bar{A}$ in A. It is known that for an invertible A also S is invertible. Iterative methods are not suitable to solve a system including S, because in general, S is dense [Smith et al., 1996].

After solving the equation (4.22) for z_2, we can solve

$$\bar{A}z_1 = b_1 - Bz_2 \tag{4.23}$$

for z_1, to obtain the complete solution vector. Instead of solving a system of the size $\eta \times \eta$, we solve one of the size $\eta_2 \times \eta_2$ and one of the size $\eta_1 \times \eta_1$. Inverting $\bar{A}$ is expensive and any method computing the inverse $\bar{A}^{-1}$ renders useless for faster solving. When we solve (4.22) and (4.23) with iterative methods, we only require the effect of $\bar{A}^{-1}$ and $-C\bar{A}^{-1}B$ on a vector. We can use an inner iterative method for this calculation without explicitly inverting $\bar{A}$ or computing S.

We examine three advantageous splits of A along its block structure. First, we can split the matrix into a free-flow and a porous-medium-flow part, cf. figure 4.7a. Second, it is beneficial to split off the saddle point problem due to its difficult solution, cf. figure 4.7b. Third, we can separate the free-flow mass balance equation and its diagonal zero block from all other equations which are diagonally dominant, cf. figure 4.7c. Considering the first two splits, we cannot expect these methods to be faster than a direct solver, as we are lacking an iterative method for the saddle point problem; thus, we have to invert $\bar{A}$. The third split looks more promising, as $\bar{A}$ is diagonally dominant and can be solved with BiCG-stab or GMRES. Further, $D = 0$ simplifies the computation of S. The crux is in the computation of equation (4.22); without an explicit S, the usual preconditioners cannot be applied directly. For some problems, approximations of S^{-1} can be constructed [Benzi et al., 2005], but we are not aware of such an approximation suitable for our problem.

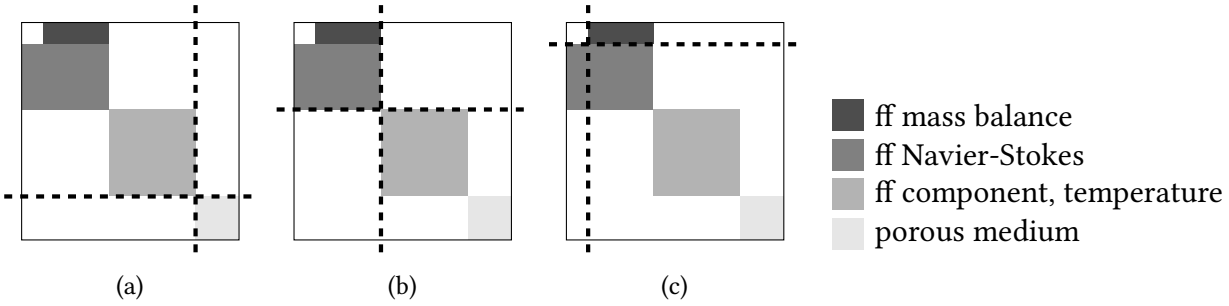

Figure 4.7: Advantageous splits of the linear system along its block structure (a) split free flow from porous-medium flow (b) split off saddle point problem (c) split empty diagonal block from diagonal-dominant block. Note the altered blocking order in the saddle point problem compared to (4.20).

A similar problem arises for the preconditioner $\begin{pmatrix} \bar{A} & 0 \\ 0 & S \end{pmatrix}^{-1}$ for the overall system. It is motivated by a block triangular factorization step on the block structure

$$A = \begin{pmatrix} \bar{A} & B \\ C & D \end{pmatrix} = \begin{pmatrix} I & 0 \\ BA^{-1} & I \end{pmatrix} \begin{pmatrix} \bar{A} & 0 \\ 0 & S \end{pmatrix} \begin{pmatrix} I & A^{-1}C \\ 0 & I \end{pmatrix}. \tag{4.24}$$

Setting up this preconditioner requires as much effort as solving the original problem [Benzi et al., 2005].

These Schur complement methods are sometimes called substructuring methods or non-overlapping domain decomposition methods. They can be viewed as disjoint substructures of the original problem which are solved independently and coupled to obtain an overall solution. For problems with strong advection, standard iterative substructuring methods do not perform well. Promising results with more sophisticated methods are published [Toselli and Widlund, 2004], but these are out of scope for this work.

Furthermore, overlapping domain decomposition methods have overlapping substructures and show better results for nonsymmetric problems with advection and larger Reynolds numbers [Toselli and Widlund, 2004].

Multigrid methods are designed for solving large systems of discretized partial differential equations. Krylov subspace methods converge slower for larger systems but in the direction of A's larger eigenvectors, called high-frequency modes. The low-frequency modes are difficult to damp and slow down the convergence of iterative methods. On a coarser grid a fraction of the low-frequency modes are mapped to high-frequency ones, which can be quickly damped. The restriction to a coarser grid, applying some solver iterations, and prolonging the solution to the original grid is usually repeated, sometimes in a recursive manner. The convergence of these geometric multigrid methods is faster, but the implementation needs access to the grid management.

Algorithms that utilize the blocking structure arising from the coupling of two physical subdomains are rare, especially for nonsymmetric problems. Howle et al. [2013] propose to use D as a preconditioner for the Schur complement S.

Algebraic preconditioners

The preconditioners purely based on algebraic techniques are black-box methods which aim for general applicability ignoring A's block structure. Examples of these types of preconditioners are the Jacobi preconditioner, the Incomplete LU factorization (ILU), and the Algebraic Multigrid methods (AMG). They can be applied to any system but some show bad convergence or breakdowns for saddle point problems because the corresponding matrices lack diagonal dominance [Benzi et al., 2005]. The ILU factorization is a LU decomposition restricted to the sparsity pattern of the matrix. This limits the fill-in and the computational complexity of the algorithm. An extension allows some fill-in, to trade higher computational effort for an improved preconditioner. The ILU(1) factorization extends the sparsity pattern from A to A^2, the ILU(k) factorization to A^{k+1}. The performance of ILU factorization can be improved by the ILU method with threshold (ILUT), which drops less important entries from the LU decomposition step. As a trivial example, ILU(0) drops all entries that are not in the sparsity pattern of A. Another approach keeps the p largest entries. This conserves the most important entries but also limits the growth of the preconditioner. ILUT breaks for zero-diagonal entries, precluding it for our saddle point problems. The ILU method with threshold and pivoting (ILUTP) avoids zeros on the diagonal by reordering rows and storing the permutation in an additional array, while preserving the overall costs to those of ILUT [Saad, 2003].

Algebraic Multigrid methods are a generalization of the multigrid methods. They lift the restriction of requiring access to the grid management, as the coarse level is derived from the linear system itself. For Galerkin methods with higher ansatz spaces, the easiest approach is to coarsen the degrees of freedom for one element by a single degree of freedom [Saad, 2003]. This does not work for our finite volume method which has only one degree of freedom per element. Alternative approaches represent the matrix as a weighted graph, identify aggregates with strong connections, and replace them with single degrees of freedom [Blatt, 2010]. These AMG methods are no longer problem-specific preconditioners.

Reordering and scaling techniques do not necessarily improve convergence behavior, but improve or create necessary features for further preconditioner or solver steps. A simple scaling is to divide all entries of a row by their diagonal entry, which is the Jacobi preconditioner, or an appropriate vector norm. A reordering changes the order of A's row and columns to move nonzero entries to the diagonal or reduce the bandwidth of a matrix which reduces fill-in. A reduced fill-in improves the quality of ILU factorizations as they miss fewer entries. The reverse Cuthill-McKee algorithm treats A as the adjacency matrix of a graph and does a breadth-first traversal sorted by increasing node degree, see figure 4.8a for an example. A simple reordering is pivoting which moves large entries to the diagonal. A more sophisticated approach is MC64, that is part of the Harwell Subroutine Library (HSL) and was called Maximum Product on Diagonal (MPD) algorithm when it was first published [Duff and Koster, 1999]. The goal is to permute the matrix to get entries with large absolute values to the diagonal. This is achieved by a representation of the matrix in a bipartite graph, with one part for rows and the other for columns. A nonzero entry in row i and column j leads to an according connection in the bipartite graph. A bipartite matching is performed, i. e., as many nodes and edges as possible are selected to maximize the nodes with a single edge, all others have no edges. This subset of edges determines the diagonal entries and the associated matrix permutation. With weights for the edges, larger entries are preferred for the

diagonal [Duff and Koster, 2001]. We give an example of how MC64 works in figure 4.8b; note the large bandwidth of the resulting matrix.

Germane to our linear system

We apply some of the more promising algorithms presented in this subsection to our problems. Some methods are provided by the Dune iterative solver template library (Dune-ISTL, Blatt and Bastian [2007]), like bindings to the direct solvers UMFPack and SuperLU. Also iterative methods like BiCG-stab and GMRES are implemented. For the preconditioners, we use the Jacobi preconditioner, ILU factorization, and the AMG method described above [Blatt, 2010]. None of the combinations of preconditioner and iterative methods work satisfactorily. Without further preconditioner or the Jacobi preconditioner, convergence breaks quickly. With ILU the first few Newton steps can be solved, but eventually the convergence rate approaches 1. The use of AMG as a preconditioner shows unexpected high initial errors around 10^{16}, causing the method to stop too early with an error of about 10^8. It is possible that the method could be tweaked to improve the stopping criterion. Additionally, AMG offers a plethora of parameters which we did not all try. Deeper knowledge might help to find a better set of parameters.

Numerical tests with damped overlapping block Jacobi and Gauß-Seidel methods do diverge. The Schur complement methods with the three different splitting strategies are outperformed by the direct solvers in the range of 100s and 1000s. We do not further consider these methods.

The reverse Cuthill-McKee reordering did not show speedups for ILU preconditioners and we do not follow up its use.

Encouraged by the performance of the ILU factorization, we found publications of other groups which used ILUTP with great success for systems similar to the one we have: Konshin et al. [2015] provides an analysis of ILU with threshold for nonsymmetric saddle-point matrices with $B = C^\intercal$. Duff and Koster [2001] introduces a combination of MC64 and an ILUTP preconditioner to solve various sparse matrices which are known to be difficult to solve. ILUTP reduces the large bandwidth created by MC64 by the tendency of dropping entries distant to the diagonal. In a test with further problems, Benzi et al. [2000] confirmed the general applicability of the resulting method. We use an implementation from Li and Shao [2011] which includes MC64, but the ILUTP preconditioner has a different dropping strategy to accommodate the use of supernodes. The performance of this algorithm for our problems will be presented in the following chapter.

4.5 Implementation

The basis for this implementation are the frameworks Dune and DuMu^x; for more information, see figure 4.9. The Distributed and Unified Numerics Environment (Dune) is a modular C++ framework for grid based discretizations of partial differential equations. It is rooted in the community of applied Mathematics but has users from applications as electro-physics, weather forecasting, petroleum prospecting and biomechanics. The idea of Dune is to offer a common interface for various advanced grid managers [Bastian et al., 2008b,a]. Since then, a module for solving linear systems has been developed, Dune-ISTL, along with a module providing local functions, and a whole ecosystem of additional modules has been grown. This project relies on

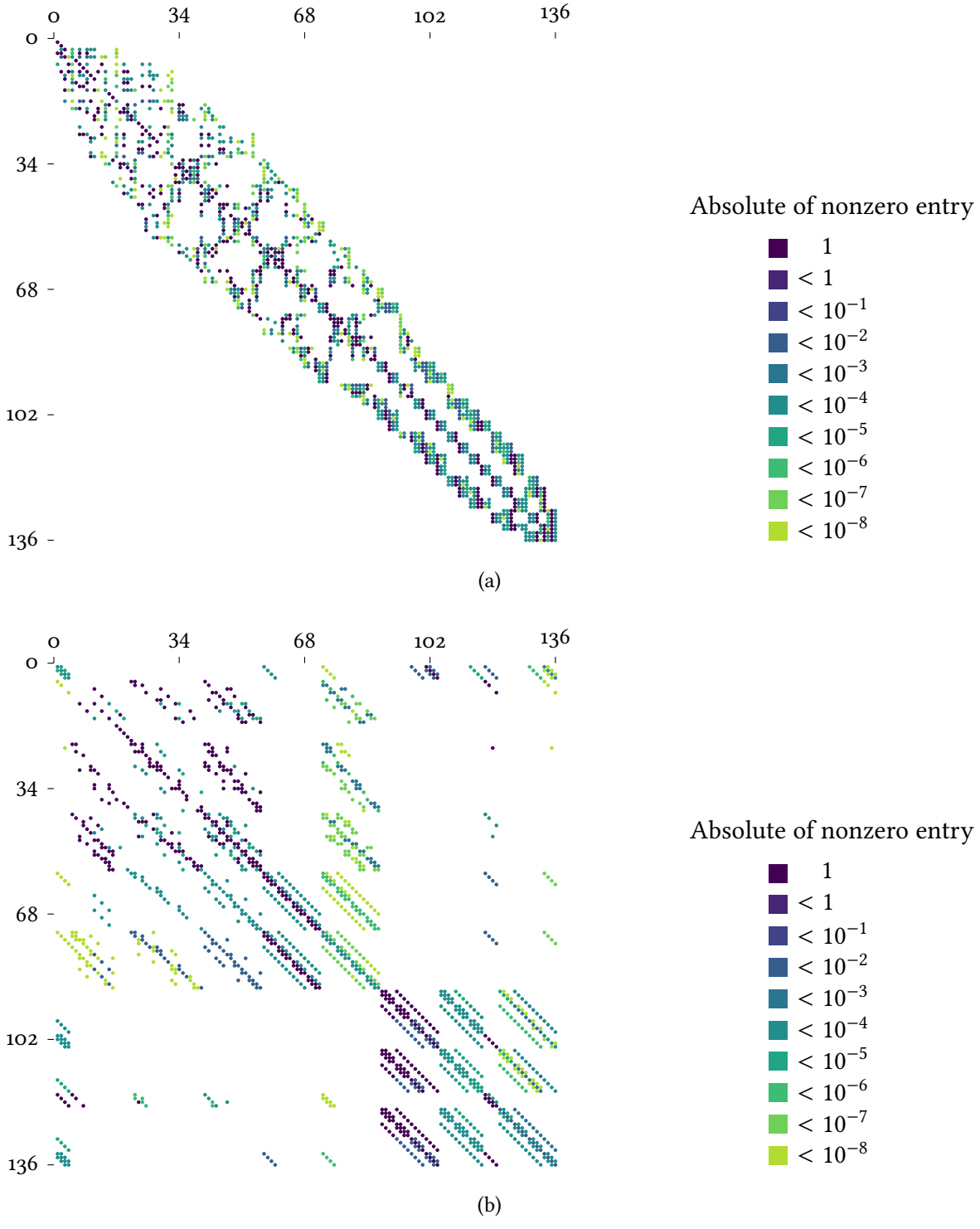

Figure 4.8: Exemplary matrix from figure 4.6 after applying reordering algorithms (a) reverse Cuthill–McKee (b) MC64

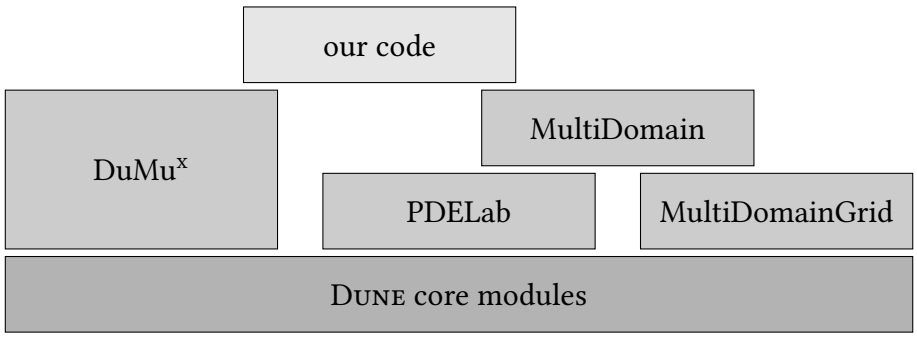

Figure 4.9: The software basis is composed of different DUNE modules

DUNE's release 2.4 [Blatt et al., 2016] and its YaspGrid in the tensor-grid mode for the grading towards the coupling interface and free-flow walls.

DuMu^x, DUNE for Multi-{Phase, Component, Scale, Physics, ...} flow and transport in porous media, is an application module based on DUNE. It provides robust solvers for multi-phase flow in porous media, optionally with component and energy transport. Various material laws are implemented to calculate fluid properties, fluid matrix interactions, changes to the aggregate state and much more [Flemisch et al., 2011]. DuMu^x in version 2.11 [Ackermann et al., 2017], without some late commits, is used with its cell-centered finite volume discretization of the two-phase compositional non-isothermal Darcy flow. The free-flow and coupling local operators also use the implemented material laws for air and water.

On top of DUNE, DUNE-PDELab offers a way to implement discretizations for systems of partial differential equations which can be expressed as weighted residual formulation. This includes finite volume, finite element and discontinuous Galerkin methods, with the restriction that they can be formulated to require at most face-neighbors. Rapid prototyping of new discretizations, code re-use, and a small performance overhead are goals of PDELab. A PDELab program consists of two parts, a local operator and the driver code. The local operator describes the discretization of the PDE per element or face with two adjacent elements. The driver code sets up the grid, the function spaces and the actual problem including the initial values, boundary conditions and used coefficients [Bastian et al., 2010]. We use PDELab to implement the MAC scheme, mainly because it supports mixed degree of freedom handling for element and intersection centers. The cell-centered finite-volume scheme for component and energy transport in the free flow had to be implemented in PDELab to gain a local operator for the whole system of PDEs in the free-flow region.

DUNE-MultidomainGrid is a DUNE meta-grid which means it internally uses another grid and alters it, while conforming to the DUNE grid interface itself. MultidomainGrid can take sub-domains from a grid and offers them as DUNE grids. Further, MultidomainGrid provides iterators for inner boundaries [Müthing and Bastian, 2012, Müthing, 2015]. This is used by DUNE-Multidomain, a module on top of DUNE-PDELab, for solving multi-physics and multi-domain problems. The sub-domains from MultidomainGrid get assigned PDELab local operators and the user has to implement a special local operator according to the coupling conditions. DUNE-Multidomain assembles the matrix with the entries for both sub-domains and the coupling [Müthing, 2015].

To solve the monolithic sparse linear system, we use DUNE-ISTL [Blatt and Bastian, 2007] and

Figure 4.10: Logos of the used software frameworks DUNE and DuMu^x

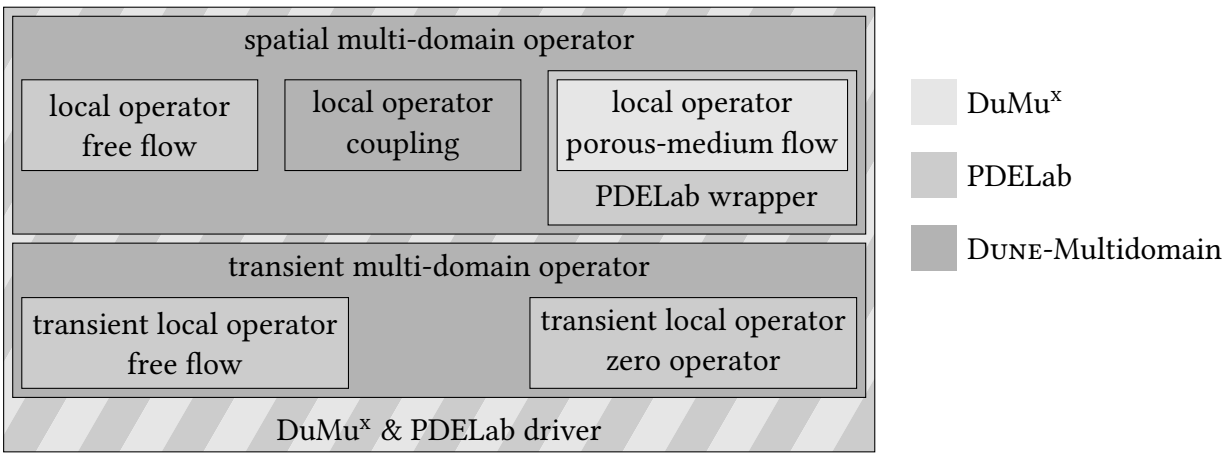

Figure 4.11: Software structure of our monolithic coupled free-flow/porous-medium-flow simulator for evaporation processes

the direct solvers UMFPack [Davis, 2004] from SuiteSparse 4.4 or SuperLU [Demmel et al., 1999].

The description of our implementation is already published as Grüninger et al. [2017]; this subsection contains direct textural adoptions.

4.5.1 Structure

The monolithic concept requires a tight integration of the free-flow and the porous-medium simulator. The subdomain simulators share data structures like vectors, utilize the same material laws, and are controlled by a common Newton's method and a common time stepping. DUNE is chosen as the common basis, but the differences between the discretization modules PDELab and DuMu^x mean that adjustments must be made. The general structure is made up of the local operators for the free-flow and the porous-medium subdomains and coupling operators, see figure 4.11.

The local operator for the free-flow region was developed for this work and uses the material laws from DuMu^x. DUNE-Multidomain can directly use this. The porous medium local operator is part of DuMu^x. It is not aware of the subdomain and needs modified classes to suppress the generation of superfluous fluxes across the interface, which would adulterate the entries in the residual and the Jacobian matrix. Further, we create a wrapper class, taking the form of a PDELab local operator which hands over the data from the DuMu^x local operator. DuMu^x adds the contributions from the storage terms in the generation of the Jacobian matrix. PDELab uses a distinct transient local operator to describe the effect from the storage term. We address this by

synchronizing the time stepping and providing a zero transient local operator for the wrapped DuMu^{x} local operator.

The coupling local operator is limited to an element on every side of the coupling interface. This limitation is considered when forming the discrete coupling conditions. In the driver code user parameters are read in, the material laws are initialized, the grid with the function spaces are set up, the initial conditions are loaded, and the Newton's iteration and the time stepping begin. Dune-Multidomain collects all contributions to the residual and calculates the Jacobian matrix. The linear system is solved, the current solution is updated, and copied to DuMu^{x} to evaluate the variable switch in the Darcy subdomain.

4.5.2 MAC local operator

The marker and cell scheme can be interpreted as a cell-centered finite volume method for the pressure combined with cell-centered finite volume methods on staggered grids, shifted by half an element, for the velocities. Discretizing equation (3.4) with the pressure as a primary variable is straight forward with a cell-centered finite volume method. Avoiding multiple explicit staggered grids, we piece the contributions from the momentum balance equation (3.3) together as volume or skeleton terms on the primal grid. We follow the naming from PDELab, where volume terms denote element contributions and skeleton terms are contributions from the vertex between two elements. Volume terms can only depend on degrees of freedom from the same element, skeleton terms are restricted to degrees of freedom from the two adjacent elements.

For a discretized domain, equation (3.3) can be formulated as

$$\int_{\tilde{V}} \frac{\partial}{\partial t}\left(\varrho_{\mathrm{g}} v_{\mathrm{g}}\right) + \int_{\partial\tilde{V}} \left(\varrho_{\mathrm{g}} v_{\mathrm{g}} v_{\mathrm{g}}^{\mathsf{T}}\right) \cdot n_{\partial\tilde{V}} - \int_{\partial\tilde{V}} \left(\mu_{\mathrm{g}} \operatorname{grad} v_{\mathrm{g}}\right) \cdot n_{\partial\tilde{V}} + \int_{\partial\tilde{V}} p_{\mathrm{g}} n_{\partial\tilde{V}} = 0, \tag{4.25}$$

when it is discretized by a finite volume scheme for an element $\tilde{V}$ on the according staggered grid, its boundary $\partial\tilde{V}$, and the normal with respect to the boundary $n_{\partial\tilde{V}}$. We have to express the terms regarding the staggered grid element $\tilde{V}$ by contributions from an element of the primal grid V. Without loss of generality, we use the two-dimensional case as depicted in figure 4.12 together with the terms left, right, upper and lower. By primal grid, we mean the grid used for the mass balance equation which we have as a Dune grid. As the momentum balance equation is shifted by half an element, we have to distinguish two cases: (a) The face normal is directed in the same direction as the velocity, the flux is within an element of the primal grid, cf. figure 4.12a. (b) The face normal is orthogonal to the velocity, the flux crosses the faces of the primal grid and it cannot be accounted for by a volume term, cf. figure 4.12b.

The storage term $\int_{\tilde{V}} \frac{\partial}{\partial t}\left(\varrho_{\mathrm{g}} v_{\mathrm{g}}\right)$ is split between the volume terms of two elements on the primal grid. The contribution of an element V on the primal grid to the residuum is $\frac{1}{2}|V|\frac{\partial}{\partial t}\left(\varrho_{\mathrm{g}} v_{\mathrm{g,left}}\right)$ for the velocity degree of freedom located on the left, cf. figure 4.12a.

For the inertia term $\int_{\partial\tilde{V}} \left(\varrho_{\mathrm{g}} v_{\mathrm{g}} v_{\mathrm{g}}^{\mathsf{T}}\right) \cdot n_{\partial\tilde{V}}$ we have the two cases. (a) v_{g} is co-directed to $n_{\partial\tilde{V}}$. The flux across the edge is a volume term $\Delta x_2 \varrho_{\mathrm{g}} v_{\mathrm{g,avg}} v_{\mathrm{g,up}}^{\mathsf{T}} \cdot n_{\partial\tilde{V}}$ in the primal grid for the left half. As the velocity is not located in the middle of V, one velocity is replaced by the averaged velocity, and the other velocity is obtained via an upwind scheme with respect to the averaged velocity. (b) v_{g} is normal to $n_{\partial\tilde{V}}$. The contributions are considered as skeleton terms. One primal grid volume

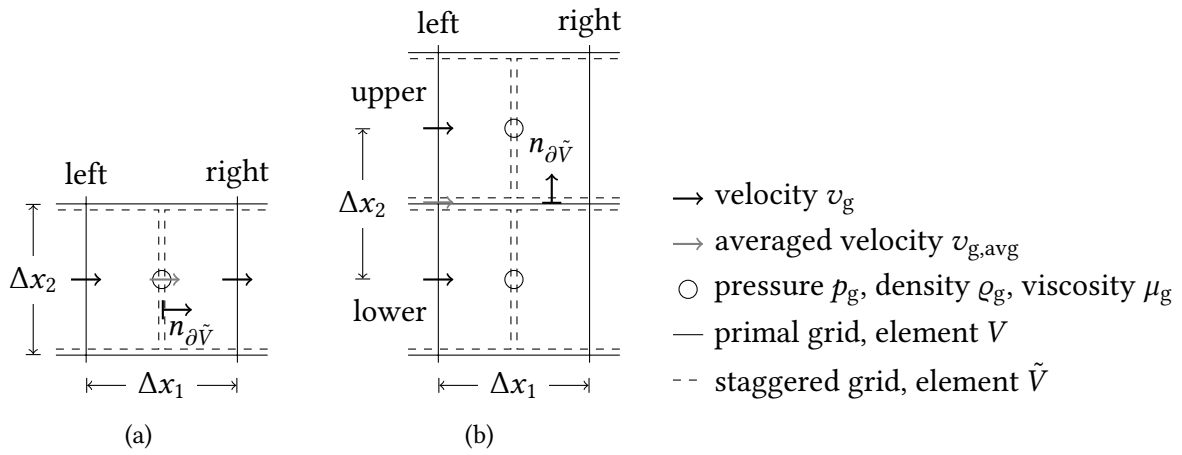

Figure 4.12: Discretization with MAC scheme for momentum balance equation (a) velocity direct in same direction as the face normal (b) velocity normal to face normal

is covered by two velocity control volumes halves, cf. figure 4.12b. In the two adjacent elements, four velocities in the considered direction are present, but we need only two for the contributions from the parts on the left. This results in $\frac{1}{2}\Delta x_1 \varrho_g v_{g,\text{left}} v_{g,\text{left}}^\intercal \cdot n_{\partial\tilde{V}}$ with one averaged velocity; for the density and the other velocity we use an upwind scheme.

The viscous term $-\int_{\partial\tilde{V}} \left(\mu_g \operatorname{grad} v_g\right) \cdot n_{\partial\tilde{V}}$ also requires the distinction of cases. (a) v_g is co-directed to the normal $n_{\partial\tilde{V}}$. The gradient is the partial derivative in the direction of the velocity which is approximated by a finite difference. The contribution to the volume term is $-\Delta x_2 \mu_g \frac{1}{\Delta x_1}\left(v_{g,\text{right}} - v_{g,\text{left}}\right)$. (b) v_g is normal to $n_{\partial\tilde{V}}$. The contribution for the primal grid is considered as a skeleton term. The gradient is the partial derivative in the direction normal to the velocity. This leads to $-\frac{1}{2}\Delta x_1 \mu_g \frac{1}{\Delta x_2}\left(v_{g,\text{upper}} - v_{g,\text{lower}}\right)$ with an averaged viscosity.

The pressure term $\int_{\partial\tilde{V}} p_g n_{\partial\tilde{V}}$ is considered to be the volume term $\Delta x_2 p_g n_{\partial\tilde{V}}$.

The other free-flow balance equations for mass, vapor mass fraction and energy are discretized with a cell-centered finite volume method. All occurring fluxes cross faces on the primal grid and are implemented as skeleton terms.

4.5.3 Reproducibility

We believe scientific software should be as free as science itself. Thus, Dune and DuMu^x are open source software frameworks. It seems natural to publish research codes in addition to plain results. A fraction of the code developed for this thesis became part of Dune, DuMu^x, or one of the other used modules, as the changes are of wider interest.

DuMu^x-pub has hosted all codes used for scientific articles and Ph. D. theses written in the Department of Hydromechanics and Modelling of Hydrosystems, University of Stuttgart since 2014. It collects the code as Dune modules in a public Git repository. Every module provides an install script and it describes the necessary third party software together with their used versions. Interested researchers and follow-up Ph. D. students can base their own research on the code, or can use it to compare their own work with our published approaches and tested codes. We hope

to mitigate the problems with reproducibility in our field of science [Hutton et al., 2016].

Everything needed to follow our decisions for the model, the setup of our test cases, and to reproduce our numerical results, can be found at DuMu^x-pub, too. The code is published under the terms of the GNU Public License (GPL) version 2 or, at your option, any later version. The module can be downloaded with Git from `https://git.iws.uni-stuttgart.de/dumux-pub/Grueninger2017a.git` and it provides the script `installGrueninger2017a.sh` that downloads and compiles all required DUNE and DuMu^x modules. The `README.md` contains further information concerning the executables and how to reproduce the numerical results that will be presented in the next chapter of this work.

Dans un monde toujours plus complexe, les scientifiques ont besoin des deux outils: des images aussi bien que des nombres, de la vision géométrique aussi bien que de la vision analytique.

Benoît Mandelbrot, 2005

5 Numerical results

Our goal is a further investigation of the evaporation experiments conducted by Mosthaf et al. [2014]. Further, we are going to showcase the versatility of our implementation by simulating a nuclear waste repository, and demonstrate the implementation's capability to model fuel cells, with complex geometries in three dimensions.

5.1 Soil water evaporation

The laboratory experiment from Mosthaf [2014] aims to measure various aspects of soil-water evaporation and to simulate the experiment for comparison. The complete setup and results from the measurements are described in Mosthaf [2014] and Mosthaf et al. [2014]. Figure 1.1b shows a photograph of the experiment.

The free flow is developed within a horizontal pipe with a diameter of $d = 0.25\,\mathrm{m}$. A propeller creates a constant flow of air. Below the pipe is a box, isolated with styrofoam panels from the outside. The dimensions of the box are $(0.25\,\mathrm{m})^2 \cdot 0.08\,\mathrm{m}$. The box is filled with a sand, which has known properties, and is saturated with water. It resides on a balance to measure its weight. The evaporated water mass is measured by tracking the mass loss.

5.1.1 General setup

The accompanying simulations from Mosthaf et al. [2014] are limited to Stokes flow in the free flow, with a simple boundary layer model limiting the evaporation rate by a higher vapor concentrations next to the interface. In Fetzer et al. [2016], the setup is extended to a Navier-Stokes flow with turbulence models. We are going to execute direct numerical simulations considering laminar flows. We want to investigate flows with Reynolds numbers 0.5, 5, 50, 500, and 2500, which are below or close enough to the critical value $Re_{\mathrm{crit}} \approx 2300$.

After the coupling, the pipe has only a short outlet to save degrees of freedom. It is long enough to get a glimpse of the vapor plume and to reduce the influence of the outflow boundary condition. Overall, the pipe is eight meters long. This does not match the actual experiment which had a shorter pipe and higher Reynolds numbers, but is sensitive and is akin to other pipe flow experiments, for example, the one from Laufer [1954].

If not stated otherwise, we use the following physical properties. The fluid properties for water follow the proposition of the International Association for the Properties of Water and Steam [IAPWS, 2007]. For air, we assume an ideal gas with the constants from Reid et al. [1987]. In the free flow, density and viscosity are independent of pressure and temperature. The binary diffusion coefficient is pressure-independent. The porous-medium properties are $\phi = 0.41$, $k = 2.65 \cdot 10^{-10}\,\mathrm{m}^2$, $\varrho_{\mathrm{s}} = 2700\,\mathrm{kg/m^3}$, $\tau_{\mathrm{pm}} = 0.5$ [Carman, 1937], $\lambda_{\mathrm{s}} = 5.26\,\mathrm{W/m\,K}$, $c_{\mathrm{s}} = 790\,\mathrm{J/kg\,K}$, and

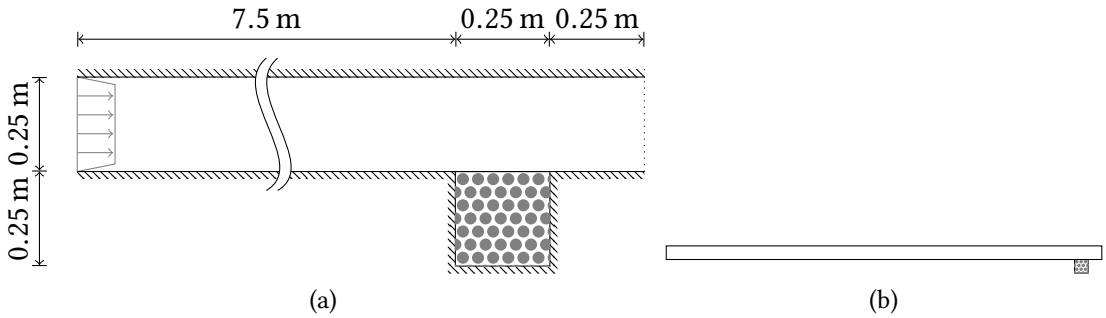

Figure 5.1: Setup of the experiments with a pipe above a sand-filled and fully water-saturated box (a) dimensions and boundary conditions with inflow on the left, outflow on the right and no-flow everywhere else (b) complete and to scale geometry of the pipe and the box

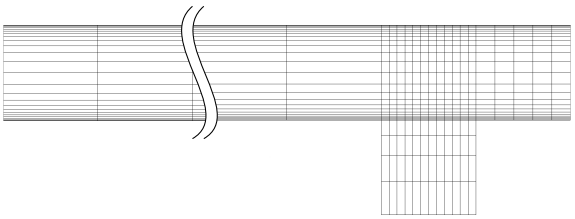

Figure 5.2: The grid for the evaporation pipe, for clarity only every fifth grid elements in vertical direction is drawn

$g = (0, \ldots, -9.81\,\mathrm{m/s^2})^\intercal$. With the Van Genuchten model we describe k_α and p_c using the constants $S_\mathrm{l,r} = 0.005$, $S_\mathrm{g,r} = 0.01$, $n_\mathrm{vG} = 8$ and $\alpha_\mathrm{vG} = 6.371 \cdot 10^{-4}\,1/\mathrm{Pa}$. For better convergence, the functions from the Van Genuchten model are regularized with a linear approximation for saturations below 1% and above 99%. The initial values for the free flow are $v^\mathrm{ff}_\mathrm{g,init} = (0.436, 0)^\intercal\ \mathrm{m/s}$, $p^\mathrm{ff}_\mathrm{g,init} = 10^5\,\mathrm{Pa}$, $X^\mathrm{ff}_\mathrm{init} = 0.0005$, $T^\mathrm{ff}_\mathrm{init} = 298.15\,\mathrm{K}$ and for the porous medium $p^\mathrm{pm}_\mathrm{g,init} = 10^5\,\mathrm{Pa}$, $S_\mathrm{l,init} = 0.5$, $T^\mathrm{pm}_\mathrm{init} = 298.15\,\mathrm{K}$ with both phases present. The initial time step size is $t^\mathrm{init} = 4\,\mathrm{s}$, the time step size is limited to $300\,\mathrm{s} = 5\,\mathrm{min}$, and the simulations ends at $t^\mathrm{end} = 18\,000\,\mathrm{s} = 5\,\mathrm{h}$.

The setup is depicted in figure 5.1. The pipe with the free flow is in the upper part. Wall boundary conditions are indicated by a hatching, inflow by the velocity profile and outflow by a dotted line. The porous medium is below. To distinguish the porous medium from the free flow the area is covered by gray circles. The gray circles are unrelated to the actual soil matrix. Neumann boundary conditions are marked by the same hatching used for the wall boundary conditions. The grid is shown in figure 5.2.

The evaporation cools down the surrounding of the interface, see figure 5.3b. The porous medium dries from the top and the vapor forms a boundary which shrinks over time as the evaporation decreases, see figure 5.3a. Most of the water evaporated in the first half hour and the upper part of the porous medium dries out. Later, with less evaporation, the differences in the water saturation between the forth and the fifth hour are barely visible.

We estimate the evaporation rate as defined by equation (2.26), but consider the porous-medium flow side of the interface using equation (3.33) and calculate the difference in water mass within

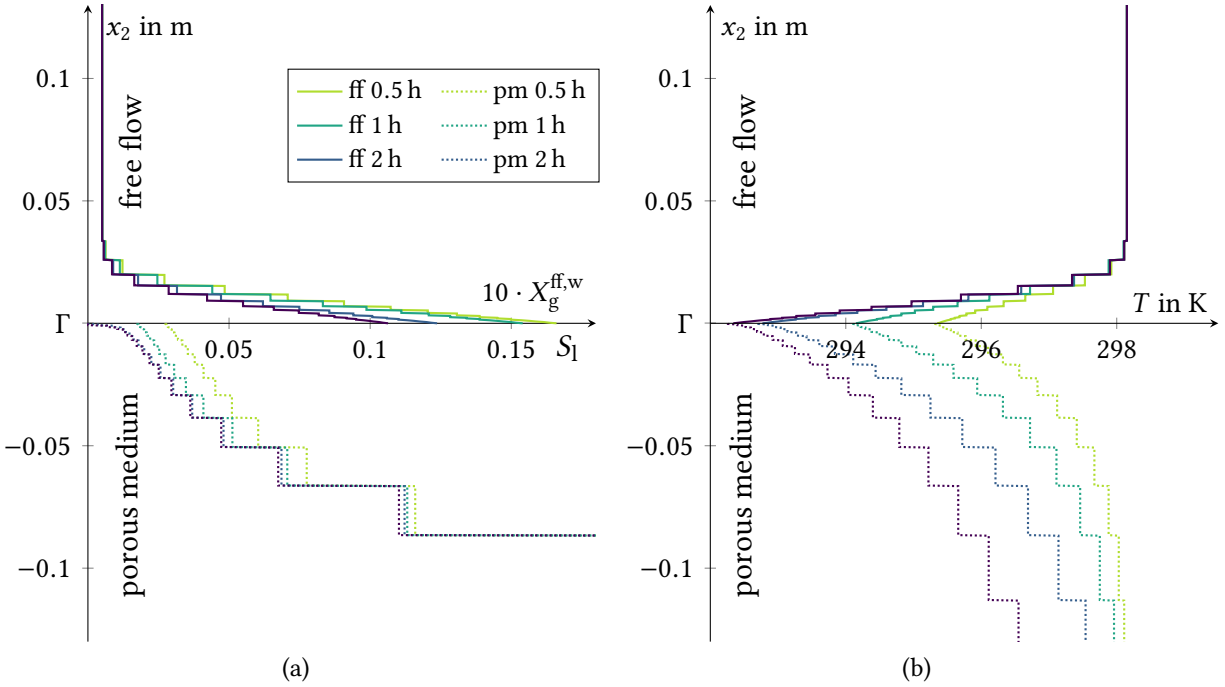

Figure 5.3: Development of some primary variables over time, cross-section at $x_1 = 7.74\,\text{m}$, interface at $x_2 = 0$ (a) saturation of liquid phase S_l in porous medium, vapor mass fraction $X_a^{ff,w}$ scaled by 10 in free flow (c) temperature T

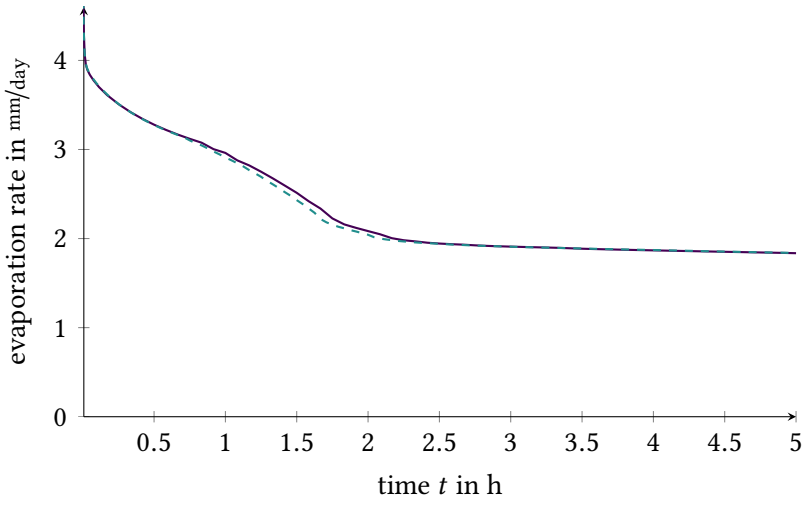

Figure 5.4: Evaporation rate for evaporation pipe test case, comparison with simulation on a refined discretization (dashed) with twice as many grid cells per dimension in the free flow

the porous medium between two subsequent time steps, divided by the time step size

$$q^i \approx \frac{\sum_{\alpha\in\{\mathrm{g,l}\}} \phi \frac{\partial}{\partial t}\left(\varrho_\alpha^i S_\alpha^i X_\alpha^{\mathrm{w},i}\right) - \sum_{\alpha\in\{\mathrm{g,l}\}} \phi \frac{\partial}{\partial t}\left(\varrho_\alpha^{i-1} S_\alpha^{i-1} X_\alpha^{\mathrm{w},i-1}\right)}{\Delta t^i}. \tag{5.1}$$

This is valid when mass enters or leaves the porous medium only via the interface by evaporation and not through the other boundaries.

The resulting evaporation rate over time for the example at hand is plotted in figure 5.4. We compare the evaporation rate with one obtained with a refined discretization: The initial and the maximum time step sizes are halved, and the free-flow grid has twice as many elements in each dimension. The evaporation rates match well, indicating that the coarse grid is fine enough. The difference after the first hour can be attributed to the changes in drying behavior given the changes in the horizontal porous-medium element size.

5.1.2 Influence of the Reynolds number

We simulate the evaporation pipe case for different Reynolds numbers. While keeping the velocity constant, we used a fixed viscosity in equation (3.3) to adjust the Reynolds number. For laminar flow regimes, the evaporation decreases with an increasing Reynolds number, see figure 5.5. Somewhere near $Re = 500$ it reaches a minimum, and for larger values, slightly more water evaporates. The reason for this is, that the different viscosities influence both the velocity near the coupling interface, cf. figure 5.6a, and the vapor mass fraction near the coupling interface, due to different lateral diffusion, cf. figure 5.6b. The product of those two values determines how much vapor is transported away, which is the limiting factor in stage 1. Larger values in figure 5.6c lead to higher evaporation rates in the first hour in figure 5.5.

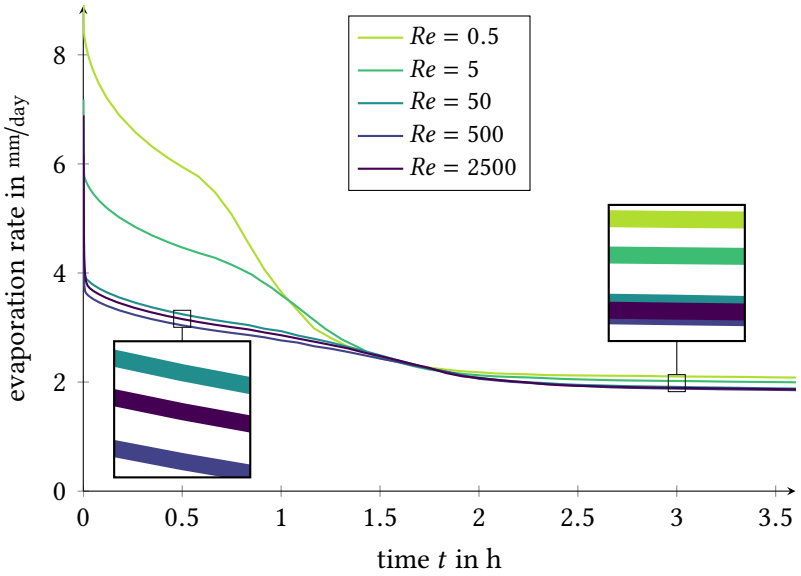

Figure 5.5: Evaporation rate depending on the Reynolds number

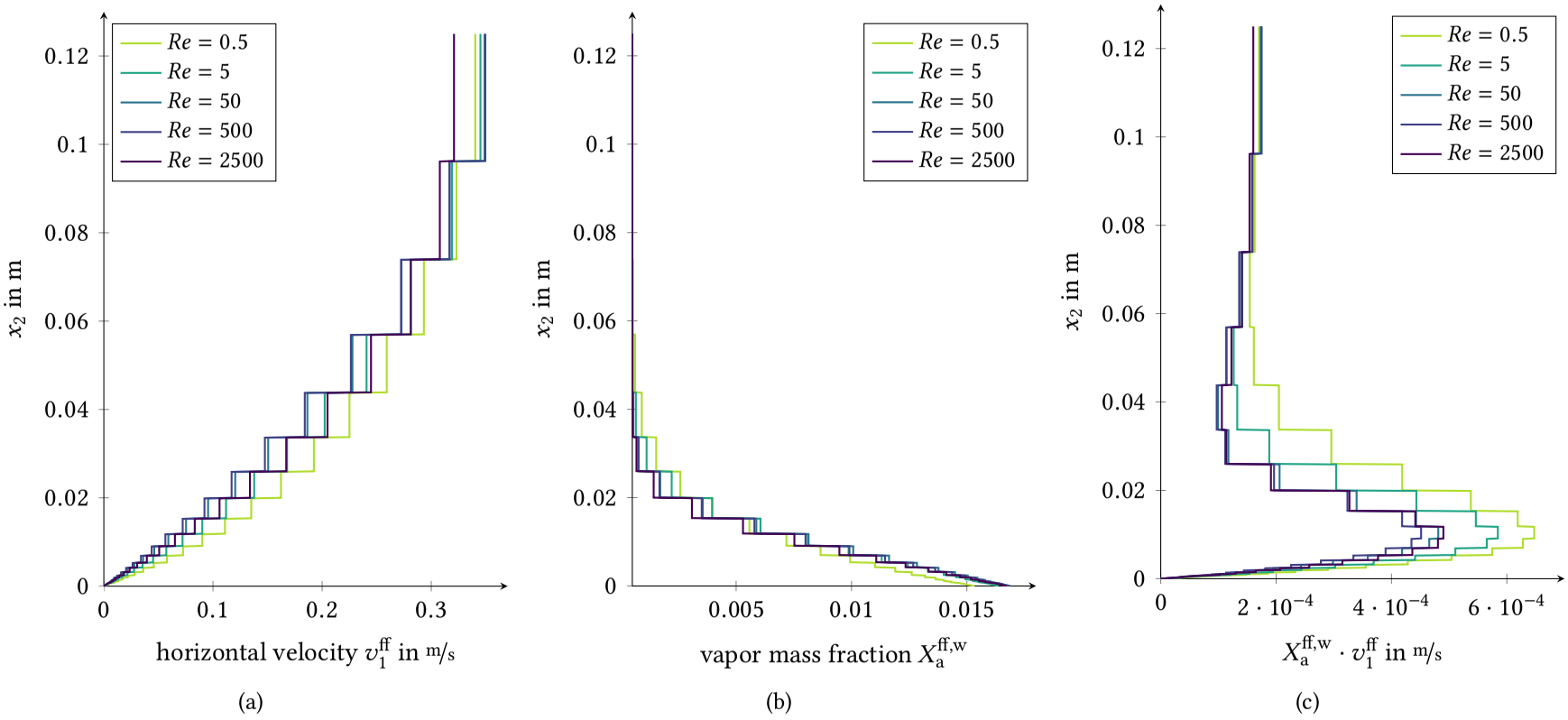

Figure 5.6: Influence of the Reynolds number in the lower half of the pipe near the end of the porous medium at $x_1 = 7.74\,\text{m}$, $t \approx 0.5\,\text{h}$ on (a) horizontal velocity v_1^{ff} in m/s (b) vapor mass fraction $X_{\text{a}}^{\text{ff,w}}$ (c) vapor mass fraction flux $X_{\text{a}}^{\text{ff,w}} \cdot v_1^{\text{ff}}$ in m/s

5.1.3 Validity of two-dimensional simplification

We want to check the validity of the assumption that the two-dimensional setup from above is a good approximation of the conducted three-dimensional laboratory experiment. The basic assumptions are that transversal fluxes can be neglected, and that the influence of the boundary conditions from both sides remains small. These assumptions might be unjustified given the wider pipe compared to the sand box, inducing additional vapor diffusion, and thermal flux perpendicular to the main flow direction.

We simplify the setup of the evaporation pipe test case to enable three-dimensional simulations for comparison. We reduce the inflow velocity to $0.01\,{}^{\mathrm{m}}/_{\mathrm{s}}$ to lower the intertia effects, resulting in a Reynolds number of $Re = 245$. This allows for a coarser grid of only 25 elements between bottom and top of the pipe. Further, the grid is no longer graded to make an approximated pipe possible, which cannot use a grading towards the wall. Elsewhere, the pipe geometry remains the same, but the runoff is shortened to 4.75 m, which is sufficiently long according to $L_{\mathrm{e}} \approx 0.06 \cdot 245\, d \approx 3.675\,\mathrm{m}$. Other simplifications include the use of a smaller sand box, which is only 10 cm deep, and a lower initial water saturation of $S_{\mathrm{l}} = 0.005$ in the porous medium. The simulation ends at $t^{\mathrm{end}} = 1800\,\mathrm{s}$ which is still long enough to reach stage 2, due to the reduced water saturation and the lower Reynolds number. The time step size is limited to 150 s.

We create four test cases, cf. figure 5.7: (A) The simplified two-dimensional test case, (B) a three-dimensional test case, which is 8 cm wide and incorporates the complete sand box and a slice of the free flow pipe, aptly named pseudo two-dimensional, as it has symmetrical boundary conditions on the left and on the right, (C) a case identical to the previous case, B, except with wall boundary conditions left and right, (D) same as previous test case, but the free-flow channel has a width of 25 cm, and (E) the free-flow subdomain is round, resulting in a pipe instead of a channel. Despite the low Reynolds number, (E) is a close representation of the actual labrotary experiment.

The additional effect of transversal diffusion is visible in the results shown in figure 5.8. Lower vapor mass fractions occur in the elements above the porous medium which are near the walls of the sand box. As a result, more water can evaporate. Figure 5.9 shows higher evaporation rates for the pipe E and for the 25 cm-channel D. Compared to the two-dimensional test case A, at $t = 0.1\,\mathrm{h}$, the pipe F has an 18% higher evaporation rate, the 25 cm-channel D even a 38% higher rate.

The evaporation rate for A and B are the same, as both have constant solutions for all quantities transversal to the pipe, cf. figure 5.8a. The refined case A is only included to ensure that no dependency exists on the grid element size or the time step size. The higher evaporation rate of the 8 cm-channel C compared to the pseudo two-dimensional channel B is caused by a higher maximum velocity for C. Near the walls, the fluid is slower, while in the center it is higher to maintain the flux. Next to the porous medium, the velocity is also higher by a factor of two to almost three, excluding the corners. This leads to a higher flux and more vapor being transported away.

For the low Reynolds number, the two-dimensional setup is insufficient. We except a less pronounced difference for higher Reynolds numbers, as the wall influence is reduced and the transveral diffusion is lower.

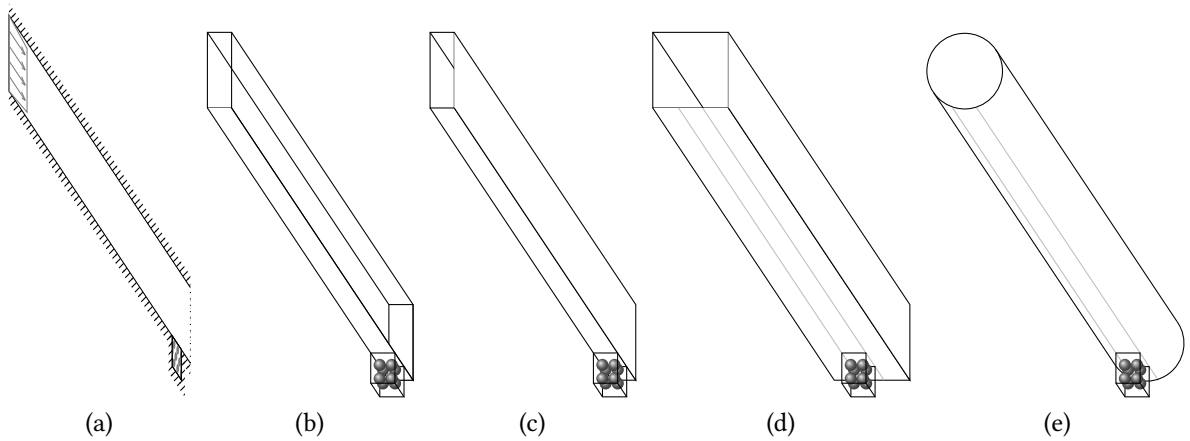

Figure 5.7: Evaporation pipe test cases in two and three dimensions, inflow at the front, outflow at the back, wall boundary conditions everywhere else, the porous medium has Neumann no-flow boundary conditions (a) A: two-dimensional (b) B: three-dimensional, pseudo two-dimensional, 8 cm wide (c) C: three-dimensional channel, 8 cm wide (d) D: three-dimensional channel, 25 cm wide (e) E: three-dimensional pipe, 25 cm diameter

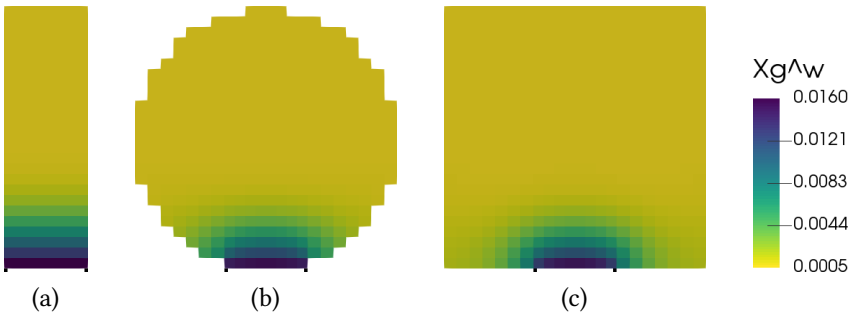

Figure 5.8: Comparison of vapor plume for (a) the pseudo-2d channel C with with $t = 8$ cm width and symmetry boundary conditions, (b) the pipe E and (c) the channel D with $t = 25$ cm width; vapor mass fraction $X_g^{ff,w}$, the location of the porous medium is indicated by the black boxes, $t = 0.1$ h, slice near the end of the porous medium at $x_1 = 4.74$ m.

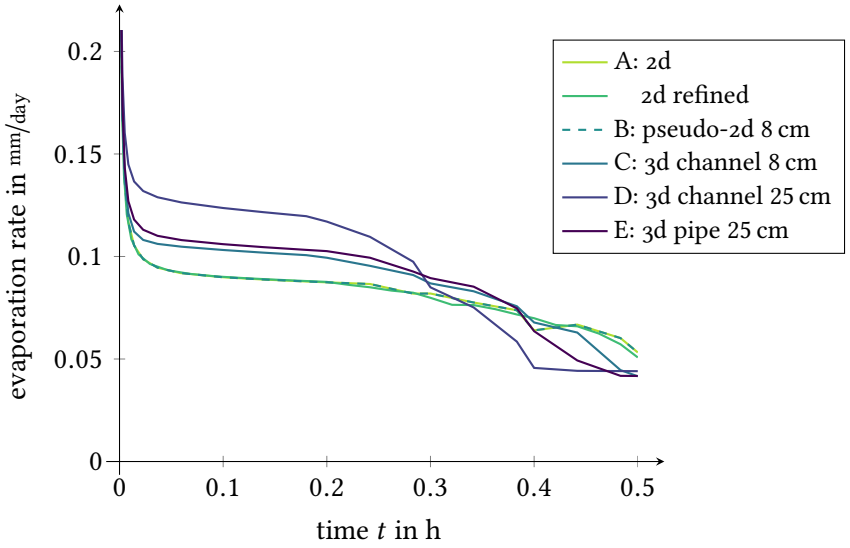

Figure 5.9: Evaporation rates for test cases in two and three dimensions

5.2 Solving the system of linear equations

To compare different solvers for the system of linear equations, we use the simplified setups from the previous subsection. We use a two-dimensional and a three-dimensional problem, refine the grid, and measure the runtimes. This reveals trends which can be extrapolated to some extend. For the two-dimensional setup, we use case A with $t^{\text{end}} = 360\,\text{s}$ and every refinement level doubles the number of elements in both dimensions for the free flow. For the three-dimensional setup, we use case C with $t^{\text{end}} = 60\,\text{s}$ and four elements in the x_2-direction. A refinement doubles the elements in the x_2-direction. The resulting number of unknowns and the number of nonzero elements are compiled in the table of figure 5.10.

All measurements were done on a Intel Core i5-4590 processor at 3.3 GHz with 8 GiB memory. The operating system is openSuse 13.2 and the C++ compiler from the GNU Compiler Collection (GCC) 6.2.1 is used with -O3 -march=native as the most important flags. We compare SuperLU 5.2.1, UMFPack 5.7.1 from SuiteSparse 4.4.6, and a GMRES preconditioned with ILUTP which is part of and makes use of SuperLU 5.2.1.

The runtimes are plotted in figure 5.11. The grid is refined until the problem grows too large: UMFPack terminates and complains about running out of memory. SuperLU starts swapping

Table 5.10: Number of unknowns η and number of nonzero elements NNZ for matrix A and different refinement levels

refinement	2d η	2d NNZ	3d η	3d NNZ
0	2 695	92 881	13 280	831 664
1	10 390	372 856	26 060	1 723 908
2	40 780	1 493 806	51 620	3 508 396
3	161 560	5 979 706	102 740	7 077 372
4	643 120	23 927 506		

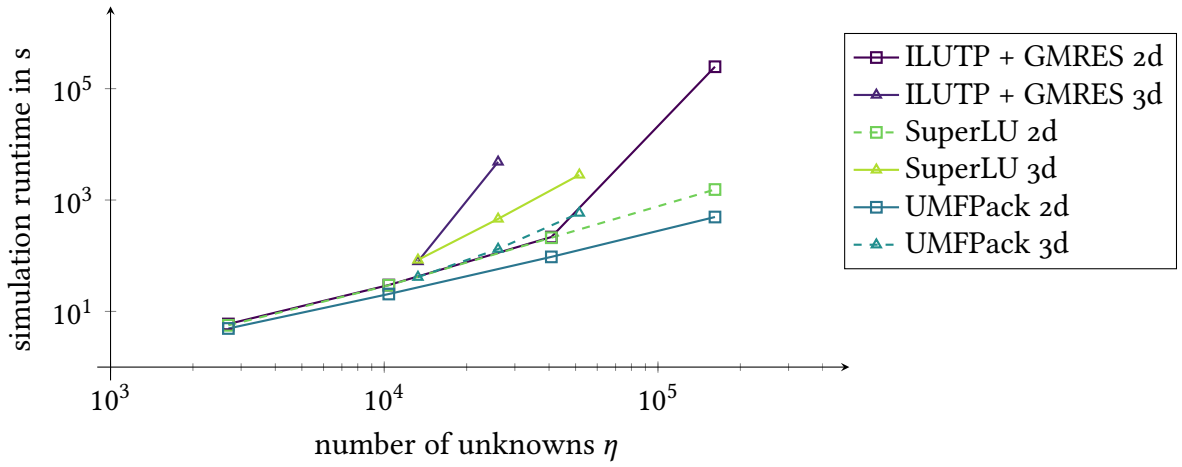

Figure 5.11: Simulation runtimes of various solvers for the linear system

data to the hard-drive which retards the solution process too much. The preconditioned GMRES only converged for time steps shorter than a second, which causes many short time steps and recalculations for failed time steps.

The most surprising result is that the preconditioned GMRES has almost the same runtimes as the direct solver SuperLU. Probably the computation of the preconditioner is dominating over the GMRES step, which stays below 10 steps. Further, for our use-case SuperLU needs between 0.1 and 5 times longer than UMFPack.

The limited time step can be seen in figure 5.12 where the attempted and the succeeded time step sizes are plotted. For the three-dimensional problem without refinement, the time step size growth during the simulation and reaches $t^6 = 19.9018\,\mathrm{s}$ without a single failing linearization. With one refinement, the successfully calculated time steps are always smaller than 1.5 s, some are even below 0.3 s. If used in an application, one would limit the maximum size of the time step to avoid the failing linearizations. Here, we want to show that the restriction of the time step size persists for the whole simulation. The same behavior occurs for the two-dimensional case with three grid refinements.

The preconditioned GMRES requires less memory than the direct solvers, in some cases only a forth, see figure 5.13. The iterative approach can be useful for applications which already have a restriction on the time step size, like for the simulation of a fuel cell presented in a subsequent section.

Regarding the extrapolated asymptotic growth of time and memory for the preconditioned GMRES, we do not expect relevant gains in performance for larger systems. Probably it is limited by the LU factorization which makes it unfavorable for our sparse matrices which still have many nonzero entries and a large bandwidth.

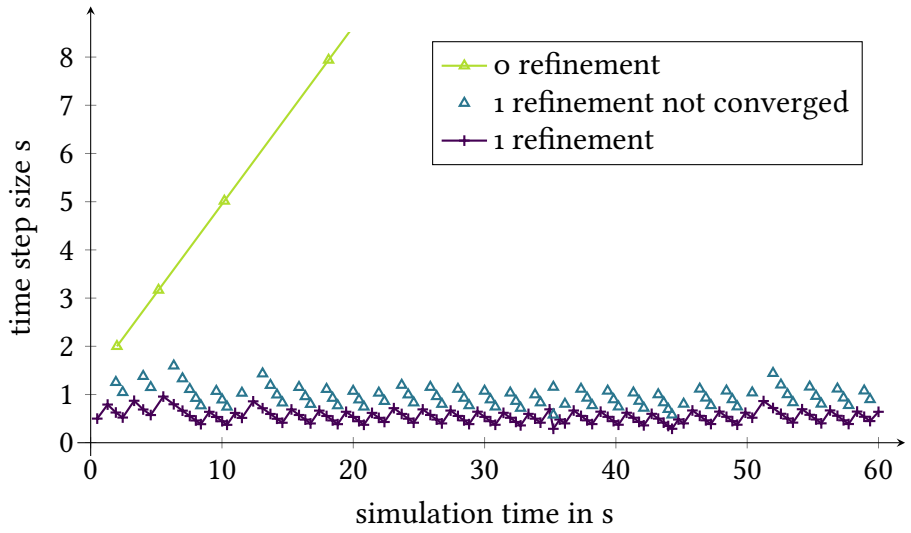

Figure 5.12: Time step sizes for preconditioned GMRES for the three-dimensional test case

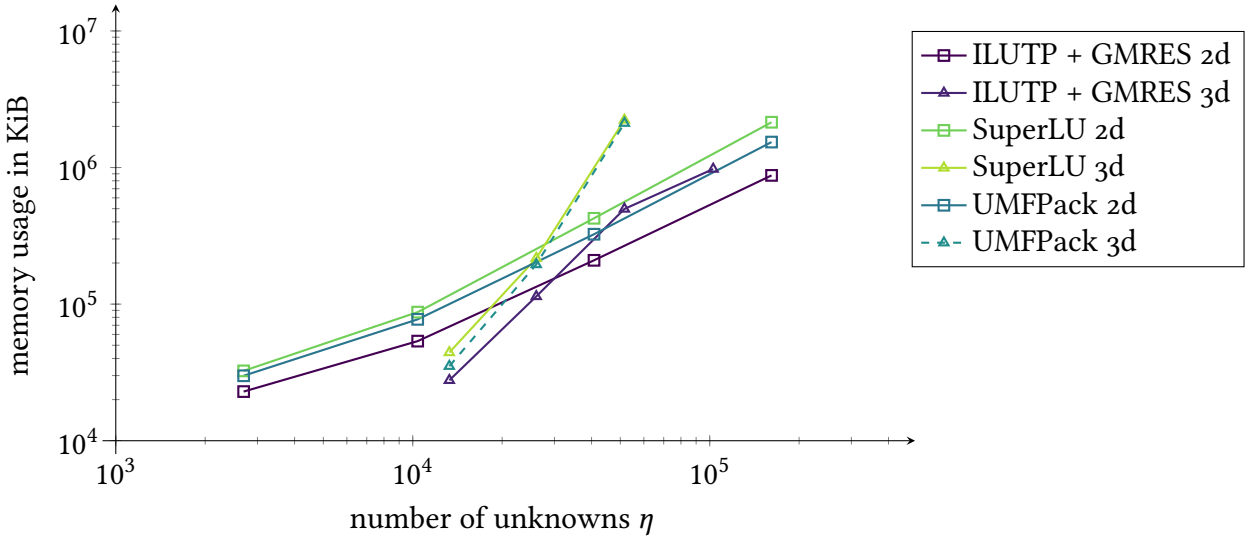

Figure 5.13: Memory usage for various solvers for the linear system

5.3 Ventilation gallery for a nuclear waste repository

One solution that many countries are considering for the disposal of high-level radioactive waste is storage in deep geological formations. The radioactive decay produces heat which affects the surrounding rock formation and compromises the stability of the repository. France plans to aerate their repository to manage the temperature and to keep the option open to retrieve the nuclear waste for at least 100 years.

We simulate a simplified setup that is based on a ventilation gallery and its influence on the soil water in the covering concrete and rock [Zhang, 2015, Masson et al., 2016]. The gallery is 5 m high, the concrete ceiling is 1 m thick, and above we consider a 9 m thick layer of Callovo Oxfordian (COx) clay, see figure 5.14. The setup has a length of 100 m. Air enters the ventilation gallery from the left and leaves it on the right. The bottom has wall boundary conditions. The porous medium has Neumann no-flow conditions on both sides and Dirichlet boundary conditions at the top, where initial values are used. Note that the Dirichlet boundary conditions at the top lead to an inflow of water. Calculating the evaporation rate with the approximation (5.1) remains valid as the inflow is several orders of magnitudes smaller than the evaporation rate.

The material parameters for the free flow remain, but we adjust the porous-medium properties. For the concrete, we use $\phi = 0.3$, $k = 10^{-18}\,\mathrm{m}^2$, and the regularized Van Genuchten model with $S_{\mathrm{l,r}} = 0.01$, $S_{\mathrm{g,r}} = 0$, $n_{\mathrm{vG}} = 1.54$ and $\alpha_{\mathrm{vG}} = 5 \cdot 10^{-7}\,1/\mathrm{Pa}$. For the Callovo Oxfordian clay, we use $\phi = 0.15$, $k = 5 \cdot 10^{-20}\,\mathrm{m}^2$, and the regularized Van Genuchten model with $S_{\mathrm{l,r}} = 0.4$, $S_{\mathrm{g,r}} = 0$, $n_{\mathrm{vG}} = 1.49$ and $\alpha_{\mathrm{vG}} = 1/15 \cdot 10^{-6}\,1/\mathrm{Pa}$. We use for both porous-medium types $\tau_{\mathrm{pm}} = 0.5$, $\lambda_{\mathrm{s}} = 10\,\mathrm{W/m\,K}$, $c_{\mathrm{s}} = 1000\,\mathrm{J/kg\,K}$, and $\varrho_{\mathrm{s}} = 2000\,\mathrm{kg/m^3}$. For the effective thermal conductivity λ_{pm}, we can alternatively use a constant value of $10\,\mathrm{W/m\,K}$ instead of the value obtained from the Johanson model. Masson and Birgle [2017] suggested the values for c_{s}, ϱ_{s} and λ_{pm}. Further, we use the Kelvin equation (2.25) analog to Masson et al. [2016]. Without the Kelvin equation, the simulation aborts when the first element dries out due to the occurring high capillary pressure and the accompanying step derivatives of the capillary pressure.

The initial values for the free flow are $v^{\mathrm{ff}}_{\mathrm{g,init}} = 0.5\,\mathrm{m/s}$, $p^{\mathrm{ff}}_{\mathrm{g,init}} = 10^5\,\mathrm{Pa}$, $X^{\mathrm{w,ff}}_{\mathrm{g,init}} = 0.01321$, and $T^{\mathrm{ff}}_{\mathrm{init}} = 303\,\mathrm{K}$. The initial values for the porous-medium flow are $p^{\mathrm{pm}}_{\mathrm{g,init}} = 10^5\,\mathrm{Pa}$, $S^{\mathrm{pm}}_{\mathrm{l,init}} = 0.98$, and $T^{\mathrm{pm}}_{\mathrm{init}} = 303\,\mathrm{K}$. The simulation starts with a time step of $t^{\mathrm{init}} = 1\,\mathrm{s}$, the maximum time step size is $1\,\mathrm{year} = 3.1536 \cdot 10^7\,\mathrm{s}$, and the simulation lasts until $t^{\mathrm{end}} = 200\,\mathrm{years} = 3.1536 \cdot 10^9\,\mathrm{s}$ is reached.

Notable changes to the setup from Masson et al. [2016] are the liquid phase pressure $p^{\mathrm{pm}}_{\mathrm{l}}$, which is deduced by our code from the gaseous phase pressure, and the water saturation, which ranges

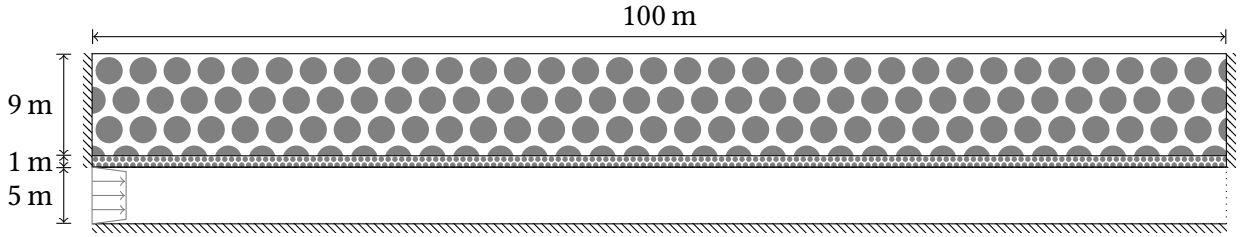

Figure 5.14: Setup for the nuclear waste repository's ventilation gallery, the values for the Dirichlet boundary conditions at the top are the initial values

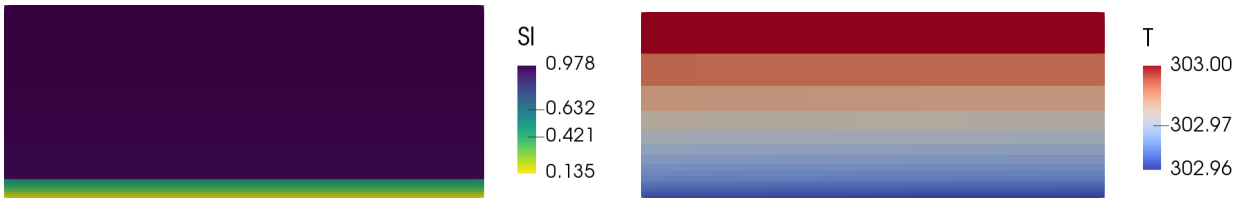

(a) (b)

Figure 5.15: Right most 25 m of the porous medium above the gallery, gallery is not shown, at $t = 200$ years (a) water saturation S_l^{pm} (b) temperature T^{pm}

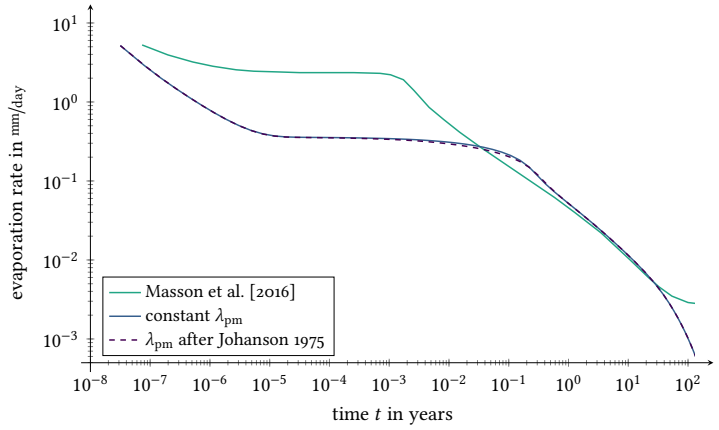

Figure 5.16: Evaporation rate for the ventilation gallery

between 328 000 Pa and 354 100 Pa instead of 400 000 Pa. Further, Masson et al. [2016] uses a RANS model for the free flow; their material laws differ, and we consider non-isothermal effects.

After 200 years, the lower third of the concrete has left 15% water saturation, the concrete in the upper two thirds has less than 50% of its original water saturation left, and the rock remains almost fully water saturated, see figure 5.15a. In other words, after 200 years, the water saturation decreased only in the concrete, not the surrounding rock. This matches the results reported by Masson et al. [2016].

The shapes of the evaporation rate plot in figure 5.16 differ from the expected shape shown in figure 2.10 which is caused by the combination of two different soils, the Dirichlet boundary conditions at the top of the porous medium, and that the plot is log-log scaled. The evaporation rate matches qualitatively the results from Masson et al. [2016], as it forms a plateau that ends after the first elements are fully dried. Quantitatively, our plateau lasts at least ten times longer before the rate falls, and the rate itself is first up to seven times smaller, then two times larger and towards the end ten times smaller than the results of Masson et al. [2016]. Our rate does not reach a steady state within the simulated 200 years.

The cumulative evaporate rate indicates the amount of water that evaporated so far. The cumulative evaporate rates are given in figure 5.17a. During the first 40 years, most of the time our models predicts more evaporated water, which reverses and leads to a 50% higher cumulative evaporate rate after 200 years. That both models have the same value after roughly 100 years is a coincident. The log-log scaled graph in figure 5.17b reveals another reversal after roughly a month.

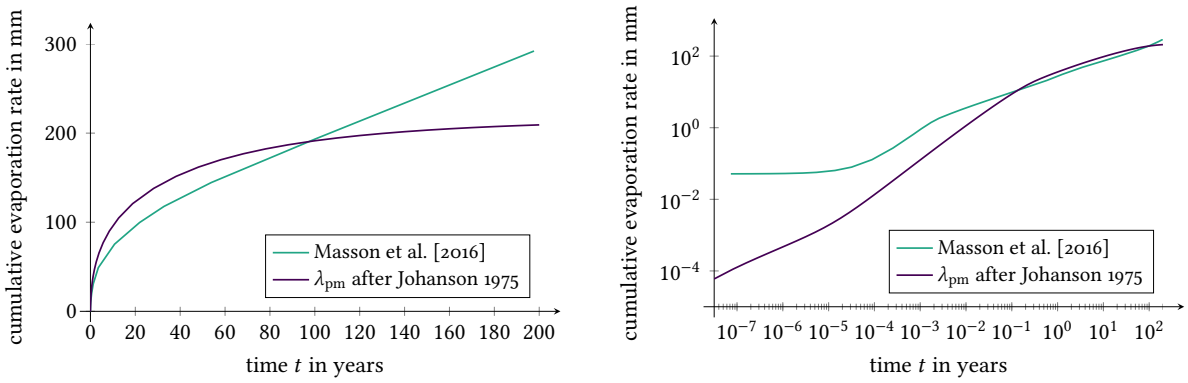

(a) (b)

Figure 5.17: Cumulative evaporation for the ventilation gallery (a) linear scale (b) log-log scale

The exact cause of the different results remains unsettled, although the different models in the porous medium, the different material laws, and the top boundary condition are likely at fault. A detailed causal research would require more data than the evaporation rate. We expect that non-isothermal effects are of minor importance as the temperature drop is small due to the low evaporation rate, see figure 5.15b.

The different effective heat conductivities play a negligible role.

5.4 Fuel cell

Next, we apply our model to the processes behind a polymer electrolyte membrane (PEM) fuel cell's water management. Its simulation requires more detailed geometries, as the interaction between the free flow and the porous medium is more complex. A fuel cell converts the chemical energy from an oxidation process into electrical energy. We consider the common case of oxidizing hydrogen H_2 by oxygen O_2. The two gases are separated by a polymer electrolyte membrane which is coated by a catalyst, like platinum. Promoted by the catalyst, the hydrogen disassociates into protons H^+ and electrons e^-, or overall $H_2 \rightarrow 2H^+ + 2e^-$. Only the protons can pass the membrane, while the electrons lead to a negative electric charge. Both sides of the membrane are connected by a cable and an electric current, the goal of the fuel cell, establishes to balance the electric charge. The protons form, together with the oxygen atoms and the electrons from the cable, water H_2O in an exothermic reaction, $1/2O_2 + 2H^+ + 2e^- \rightarrow H_2O$. On the hydrogen side, the electron reduction is an oxidation and the reaction layer is called anode. The reaction layer on the oxygen side is called cathode.

The protons can only pass the membrane if it is humidified, but too much water blocks the supply of oxygen for further reactions. The reaction produces water and heat, both of which influence the water management. To prevent the clogging of the membrane with the produced water, both sides of the membrane are covered by thin layers of hydrophobic porous media. This makes it easier to remove liquid water and the larger water surface increases the evaporation. Conventional gas distributors have continuous gas channels parallel to the porous medium. This limits the gas supply to the rate of diffusion. Gas distributors with an interdigitated flow field in

the gas channels gas channels, see figure 5.21 for an example, force the gas to flow advectively through the porous medium, resulting in an increased gas supply and better removal of water [Nguyen, 1996]. The resulting fuel cells are more efficient compared to the ones with conventional gas channel layouts [Wang and Liu, 2004, Yan et al., 2006]. The composition of a fuel cell is sketched in figure 1.4a, a laboratory sample of a gas distributor is shown in figure 1.4b.

Numerical simulations are of great importance for the development of fuel cells [Wu, 2016]. Of particular interest is the process by which the gas flow in the channel interacts with the discharge of water, produced by the reaction, into the gas channels. This interaction eventually includes a number of processes: advective free flow in the gas channels, transport of water in the gas channels, interaction in the gas channels, transport of vapor in the gas channels, and interaction between the gas-channel flow and the flow in the porous diffusion layer through shear stress.

We want to show the capabilities of our implementation as a tool to investigate the water management in a fuel cell. To focus the complexity of the model, we don't include the electrochemical processes. To simplify, instead of tracking the oxygen level of the air, we assume that all components of the air, excluding vapor, are consumed. The consumption of air and the production of water and heat have a fixed rate, independent from the concentration of the substances. The porous medium is not hydrophobic, water remains the wetting phase. The energy transport through the casing and the collector for the electric current is not modeled. The values for the following quantities are devised: the free-flow inlet velocity, the humidity of air, and the source and sink term rates. The geometry and most porous medium properties are taken from Acosta et al. [2006].

5.4.1 Two gas channels with connecting porous layer

The model domain includes the area between the centers of two neighboring, but not connected, gas channels, and the connecting porous media layer beneath. We exclude the membrane and the complete anode side, as the processes on the anode side are identified to limit the efficiency of the fuel cell [Acosta et al., 2006]. At the base of the 0.05 mm thick porous medium layer, there is a reaction layer where the chemical reaction happens. The reaction layer contains the source and sink terms. The left gas channel has an inflow of air, the right channel has an outflow, and every other boundary has wall or Neumann no-flow boundary conditions. This means that the only flow path is through the porous medium. The complete flow is forced to enter the porous medium from one gas channel and leave it through the other gas channel, see figure 5.18.

Below we list the physical properties that differ from the above evaporation pipe example. The porous-medium properties are $\phi = 0.78$, $k = 5.2 \cdot 10^{-11}\,\mathrm{m}^2$, $\varrho_\mathrm{s} = 1430\,\mathrm{kg/m^3}$, $\tau_\mathrm{pm} = 3$, $\lambda_\mathrm{s} = 15.6\,\mathrm{W/m\,K}$, $c_\mathrm{s} = 710\,\mathrm{J/kg\,K}$. We use again the regularized Van Genuchten for k_α and p_c with the constants $S_\mathrm{l,r} = 0.005$, $S_\mathrm{g,r} = 0.05$, $n_\mathrm{vG} = 3.652$ and $\alpha_\mathrm{vG} = 6.66 \cdot 10^{-5}\,1/\mathrm{Pa}$. In the reaction layer we have $\phi = 0.07$, the source term for the total mass balance equation (3.26) is $-20\,\mathrm{kg/m^3\,s}$, the source term for the water mass balance equation (3.25) is $20\,\mathrm{kg/m^3\,s}$, and the source term for the the energy balance equation (3.27) is $4 \cdot 10^7\,\mathrm{J/m^3\,s}$.

The initial values for the free flow section are $p^\mathrm{ff}_\mathrm{g,init} = 2.013^5\,\mathrm{Pa}$, $X^\mathrm{ff}_\mathrm{init} = 0.1$, $T^\mathrm{ff}_\mathrm{init} = 343.15\,\mathrm{K}$ and the initial values for the porous medium section are $p^\mathrm{pm}_\mathrm{g,init} = 2.013^5\,\mathrm{Pa}$, $S_\mathrm{l,init} = 0.01$, $T^\mathrm{pm}_\mathrm{init} = 343.15\,\mathrm{K}$ with both phases present. At the inlet, the flow has a velocity $v^\mathrm{ff}_\mathrm{g} = 0.86\,\mathrm{m/s}$ in a block velocity

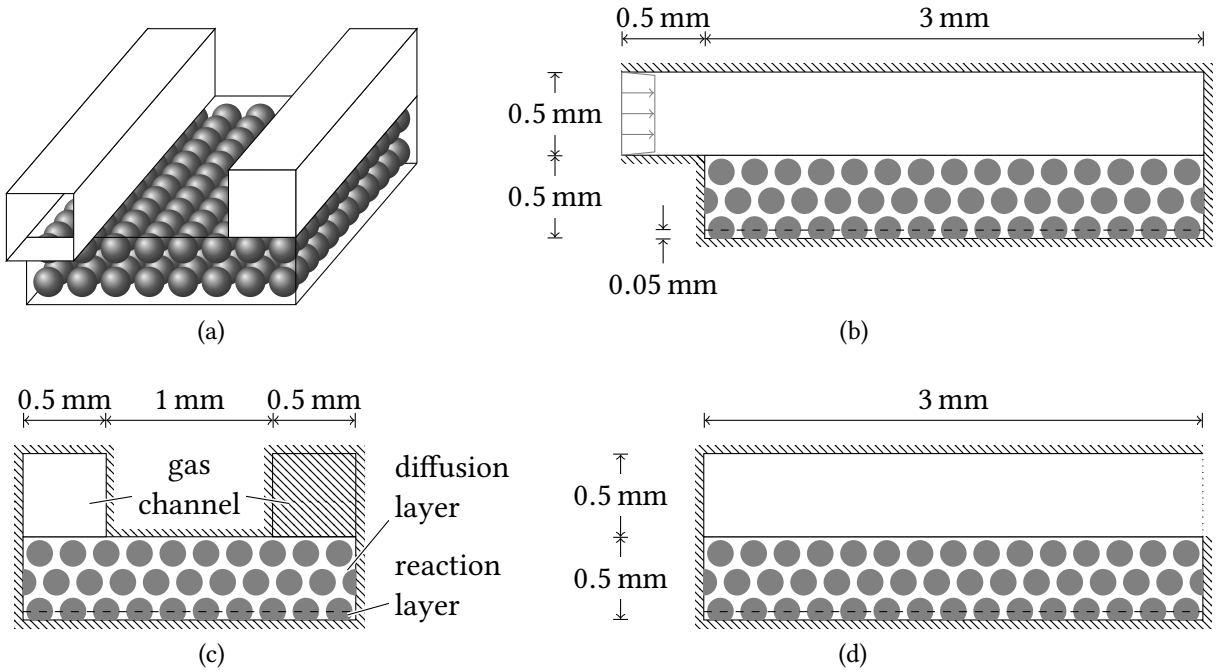

Figure 5.18: Setup for the fuel cell channel (a) general view (b) side view of left gas channel with inlet on left (c) front view (d) side view of right gas channel with outlet on right

profile. The resulting maximum velocity of 1.5 m/s and the related Reynolds number of $Re = 71$ are too small by a factor of 20 to 30. In this test case, we are less interested in the free flow within the gas channel, and rather focus on the processes within the porous medium. In this case, the flux through the porous medium is in the right order of magnitude. For longer gas channels, the gas channel entry velocity should be accordingly increased.

The initial time step size is $t^{\text{init}} = 0.25$ s, the maximum time step size is 2 s, and the simulation lasts for 60 s. The resulting linear system has 12 514 degrees of freedom.

Some simulation results are shown in figure 5.19. The aim is not to reach steady-state. The air flows through the left gas channel and dips towards the porous medium. The flow then crosses the porous medium in a curved path, almost perpendicular to the gas channel. Finally, the air reaches the left gas channel and continues to the outlet. Beneath the left gas channel, the porous medium dries out completely, in contrast to the right part which accumulates liquid water, see figures 5.20. The reason for this phenomenon is shown in figure 5.19b and 5.19c. In the left section the water is taken up by the air, and evaporation cools the system. In the right section, the more humid air takes up less water, leaving more of the produced water in the porous media.

These modeled effects are essentially what occurs in the fuel cells, which can lead to flooded fuel cells. After including the electrochemistry, we believe that the model can help improve the understanding of the relevant influencing factors.

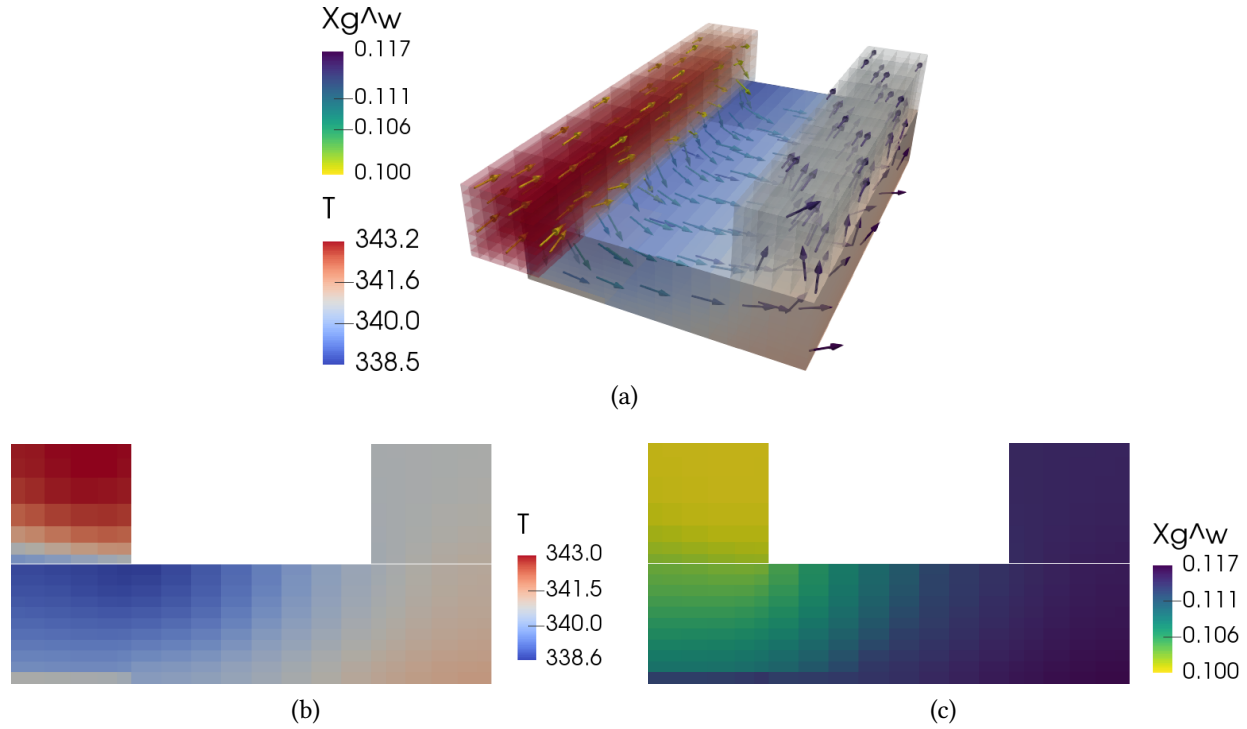

Figure 5.19: Evaporation within the fuel cell's porous medium, lower temperature indicates evaporation which increases the vapor mass fraction of air, $t = 60$ s; (a) arrow orientation: flow field direction, arrow color: vapor mass fraction in air X_g^w, volume color: temperature (b) temperature T at x_1-x_3 plane in the middle of the porous medium (c) vapor mass fraction in the air X_g^w

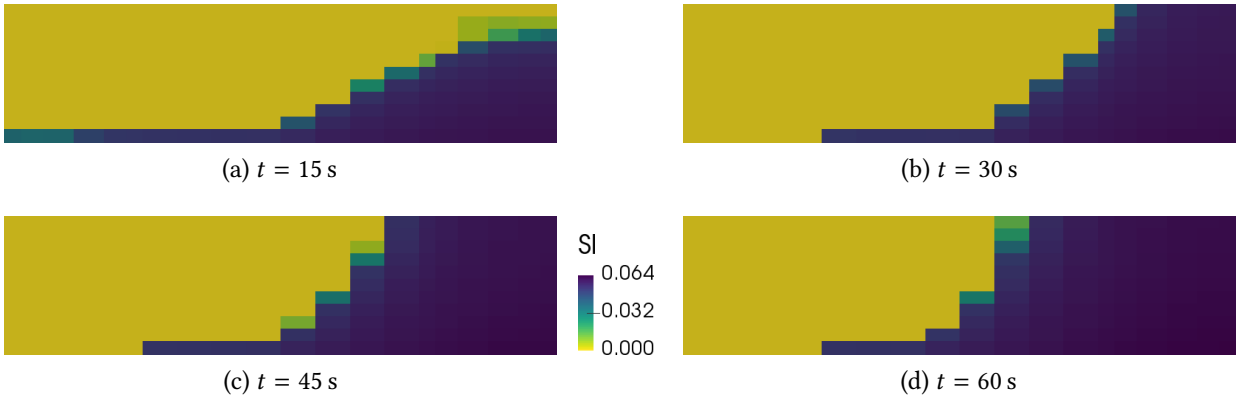

Figure 5.20: Water saturation within the fuel cell's porous medium over time, at x_1-x_3 plane in the middle of the porous medium

5.4.2 Complex gas channel layouts

To simulate a complete gas distributor, the geometry must become more complex. To demonstrate the feasibility, we simulate two simplified gas distributors. The first is a serpentine layout where a single gas channel connects the inlet and outlet with a zig-zag-pattern; see figure 5.21a for the simulation setup and figure 1.4b for a photograph of a laboratory sample. The second is a interdigitated layout which has no direct gas channel between inlet and outlet, forming a pattern of two combs with an offset. The gas is forced to enter the porous medium to reach the gas channels leading to the outlet, see figure 5.21b.

The serpentine layout has 39 003 degrees of freedom, the interdigitated 38 355. All parameters are taken from the fuel cell simulation above, including the source and sink terms, the dimensions in x_3 direction, and the initial conditions. The only modifications are that $S_{\mathrm{l,init}} = 0.05$ is five times higher to reduce the number of variable switches due to dry out, and the simulation is shortened to $t^{\mathrm{end}} = 5\,\mathrm{s}$.

We do not expect to discover anything new with our simple model, but we hope to provide insight into the water and heat management, as well as display the results from the different gas channel layouts for better comparison.

The incoming air dries the porous medium next to the gas channels. The serpentine layout has more completely dry elements. In the interdigitated layout evaporation happens within the porous medium, as the air entering the porous medium is dryer compared to the air leaving the porous medium, see figure 5.22. Lower temperatures indicate a higher evaporation rate, but it is not clear from the temperature where evaporation in the porous medium happens, as it is blurred by the temperature drop caused by evaporation below the gas channels. In some areas, the air coming from the porous medium is warmer than the air leaving the system, see figure 5.23. This could mean that different layouts have different cooling capabilities. Further, the layouts influences the gas flow in the reaction layer. Considering the relative gas pressure $p_{\mathrm{g}}^{\mathrm{pm}} - 2.013 \cdot 10^5$ at the bottom of the reaction layer, as in figure 5.24, the difference becomes obvious. The serpentine layout has an almost steady, small gradient, while the interdigitated layout has steeper gradients between the gas channels. The latter could be beneficial to provide oxygen for the chemical reaction and to transport away the produced water.

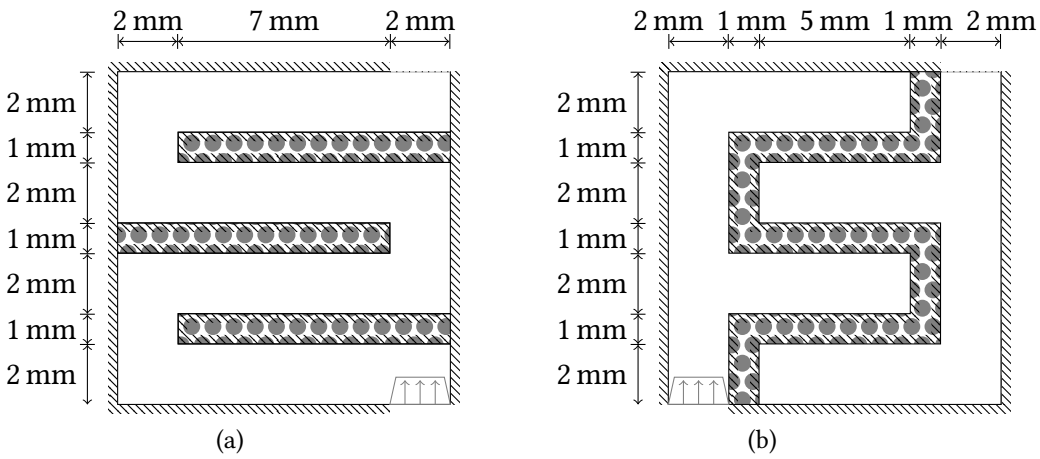

Figure 5.21: Top view of the complex gas channel layouts (a) serpentine (b) interdigitated

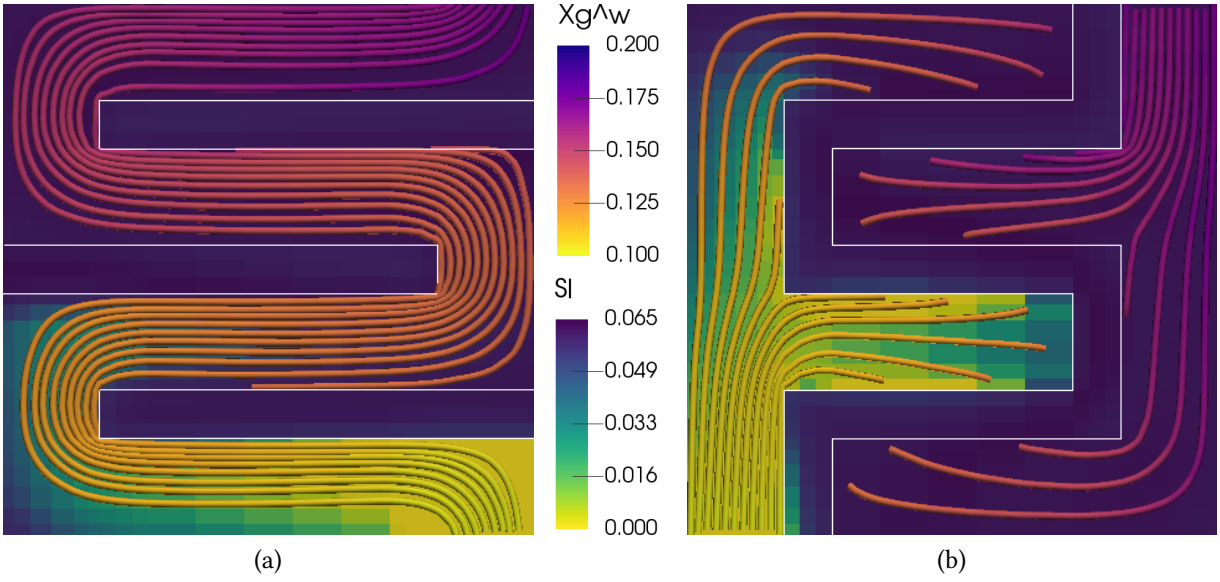

Figure 5.22: Water saturation and vapor mass fraction for different gas channel layouts, streamlines are vapor mass fraction $X_g^{w,ff}$ in free flow, background is water saturation S_l in porous medium, $t = 5$ s (a) serpentine (b) interdigitated

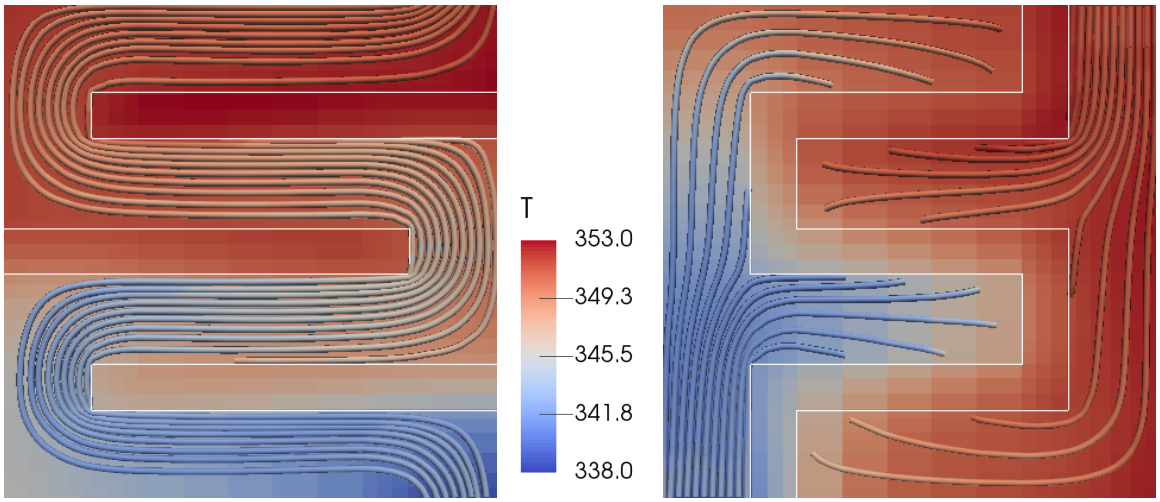

(a) (b)

Figure 5.23: Temperature for different gas channel layouts, streamlines are in free flow, background is porous medium, $t = 5$ s (a) serpentine (b) interdigitated

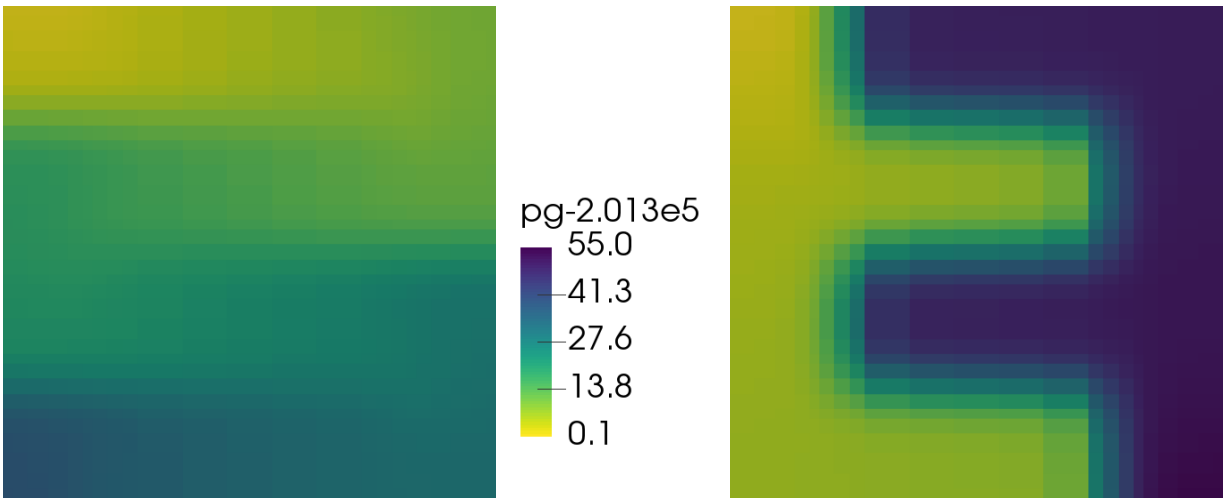

(a) (b)

Figure 5.24: Relative gas pressure $p_g - 2.013 \cdot 10^5$ in the reaction layer for different gas channel layouts; view from bottom, $t = 5$ s (a) serpentine (b) interdigitated

Człowiek nigdy nie ogląda się na to, co zrobione, ale na to patrzy, co ma przed sobą do zrobienia.

Marie Skłodowska Curie, 1894

6 Finale

We introduced the relevant physical processes in the compositional non-isothermal free flow and the two-phase compositional non-isothermal porous-medium flow. We described how we model these using partial differential equations, closing conditions and material laws. We emphasized how both the Navier-Stokes equation and the Darcy equation play an important role. Then we presented the coupling conditions based on a local thermodynamic equilibrium and the Beavers-Joseph-Saffman condition, following the approach from Mosthaf et al. [2011].

We use a cell-centered finite volume method on an axially parallel grid to discretize the partial differential equations. For the Navier-Stokes equation, we use the marker and cell scheme which moves the degrees of freedom for the velocities towards the edges of the grid elements, forming one secondary, staggered grid per dimension. The coupling conditions are applied without additional variables along the coupling interface. They are incorporated as Dirichlet, Neumann or Robin boundary conditions, all of which result in interfaces fluxes.

For the porous-medium flow we use the finite volume implementation provided by DuMu^{x}. The marker and cell scheme is implemented using PDELab. The grid is split into two subdomains, where the elements on both sides of the coupling interface match, simplifying the implementation. The coupling is provided by a Dune-Multidomain local coupling operator. The time integration is approximated with an implicit Euler scheme. All contributions are compiled in one non-linear system. This is linearized by a Newton method.

The resulting nonsymmetric sparse matrices are solved with direct methods. We investigated iterative methods and tested promising ones: An algebraic multigrid (AMG) method, a Schur complement method, and a GMRES preconditioned with MC64 and an incomplete LU factorization with threshold and pivoting (ILUTP). We experienced problems with AMG's error criteria leading to convergence problems. The Schur complement method is slow as we lack a preconditioner for the not explicitly calculated Schur complement. GMRES with ILUTP shows a restriction on the time step size for larger problems; the reason remains unclear.

The numerical results presented in the previous chapter show that there is a wide range of applications that our implementation is capable of simulating. Three applications are then simulated: A laboratory experiment to investigate soil-water evaporation, the water content of the concrete and rock covering a ventilation gallery of a deep geological repository for nuclear waste, and the simplified water management of a fuel cell. These simulations cover time scales which span from seconds to decades and length scales which range between nanometers and dozens of meters. We are able to simulate setups in two and three dimensions, including complex geometries as long as they can be approximated with an axially parallel grid, using various porous-medium types, and with free flows spanning several magnitudes of Reynolds numbers.

Compared to the work of our predecessors [Mosthaf et al., 2011, Baber et al., 2012], we obtain a speedup for the simulations between one and two orders of magnitude with comparable results [Grüninger et al., 2017] and without oscillations in the free flow.

Regarding the applications, we have determined that the Reynolds number has an influence on the evaporation rate. If the free flow channel or pipe is wider than the porous medium, a simulation using a two-dimensional simplification may be flawed, depending on the Reynolds number. The evaporation rate in the ventilation gallery differs by a factor of up to ten and the cumulative evaporation rate by 50% when compared with the results from Masson et al. [2016]. That being said, we can confirm the overall result of the given setup, where the water saturation in the rock is not altered, and only the concrete ceiling partially dries. For the fuel cell with an interdigitated flow field, we could show that parts of the porous medium accumulate water which might reduce the efficiency of the fuel cell. Further investigations and insights will be reachable after the electrochemistry is included.

6.1 Conclusions

We draw the following conclusions regarding the coupled Navier-Stokes and Darcy flow in general, particularly our discretization and implementation

Material laws

Our implementation heavily relies on the material laws provided by DuMu^{x}. We adopted the set of material laws used by the predecessor code. We altered some material laws—for example, the law used to compute the effective thermal conductivity λ_{pm}, or the assumption of incompressible flow in the free-flow subdomain—to either reduce computational costs or to diminish the number of nonzero matrix entries. We tried to keep our results close to the results from the predecessor code, and did not systematically examine all used material laws. As the example in section 5.3 shows, changing some laws will marginally impact the result. Further simplifications could have two advances: First, one could reduce the computational costs of the matrix assembly. Second, it would lower the bar for other scientific groups to reproduce our results as implementing the used material laws is a major obstacle. Still, one has to balance every simplification against the applicability to the different applications. If the implementation becomes more focused on a specific example, it can exploit the special circumstances at hand.

Free flow

The used first-order upwind scheme introduces severe numerical diffusion which prevents eddy detachment as the fine grid required leads to linear systems too large to solve. Replacing the upwind scheme with a total variation diminishing (TVD) or a higher-order scheme would improve this, but we cannot include such schemes due to PDELab's ability to only access face-neighboring degrees of freedom. In general, when detached eddies occur near the interface, the validity of the coupling conditions must be reviewed.

In this work, the grid resolution and the consequential large number of degrees of freedom limit the free flow to laminar flows with moderate Reynolds numbers. To investigate flows with higher Reynolds numbers, the implicit scheme can be replaced by a semi-implicit predictor-corrector scheme [Versteeg and Malalasekera, 2007] and a higher-order scheme. This conflicts with the implicit coupling of free flow and porous-medium flow. More suitable methods like spectral

methods or discontinuous Galerkin methods require appropriate coupling conditions. The general approach by Kanschat and Rivière [2010] might be of avail.

The examined applications all have a stationary flow field, no change in the boundary conditions over time, and no processes within the domain that affect the flow field. Precomputing the velocity once, similar to Masson et al. [2016], would reduce the computational cost for both the assembly and the linear methods, especially as the linear system would no longer contain a saddle-point problem. Note that applications with transient flow fields exist like soil-water evaporation using measured wind velocities, or biological applications considering breathing or heartbeats.

Solving the system of linear equations

The limiting factor remains the solver for the system of linear equations. The direct solver UMFPack is currently the preferred choice. The easiest way to raise the bar with simulating larger problems is to use better computers. Instead of a desktop computer which we used for the simulations in this work, a workstation or a cluster node with the latest hardware and more memory can cope with larger linear systems. The thread-parallel SuperLU_MT might decrease the time for solving the system, but only by the number of possible threads. Nevertheless, the memory limit, common for all direct methods, remains. Further progress with direct solvers [Agullo et al., 2013], especially utilizing the enormous computational capacities of graphics processors [Davis et al., 2016], will reduce the time to solve the occurring linear systems in the future.

The use of iterative methods to speed up the solution of linear systems still needs more work. The investigated combination of MC64 reordering and ILUTP can probably be improved with a more suitable choice of parameters, especially regarding the restriction on the time step size. A less frequent calculation of the preconditioner carries potential; the MC64 reordering is calculated every time step and the ILUTP preconditioner every Newton step, which can be done less often. As this reduces the quality of the preconditioner, one must, in turn, take care to ensure the robustness of the overall method.

The algebraic multigrid methods are worthy of a more in-depth investigation. This also applies to the Schur complement methods, for which we lack a cheap approximation of the Schur complement. Both approaches promise a lower computational complexity compared to the LU decomposition of the direct solvers and the ILU preconditioners. Additionally, the used algebraic multigrid method scales well for parallel computations [Blatt, 2010].

Decoupling time steps

The idea to decouple the two domains, and to compute the free flow more often was proposed by Rybak and Magiera [2014] and Rybak et al. [2015]. This idea stems from the fact that the porous-medium flow is much slower, and requires updates less frequently. If it were solved less often, it would reduce the overall computational cost. For the examined applications, the benefit is negligible. Regarding the two-dimensional setup from section 5.1.3, the porous medium is accountable for only 10% of the degrees of freedom and its matrix assembly causes less than a sixth of the overall time spend for the assembly. For the other evaporation pipe setups, the free flow takes up even a larger share of both degrees of freedom and assembly time. This is true as, in the free flow, the time steps are keep small, the values change little, and no additional Newton steps

are required by the nonlinear material laws. For the fuel cell, the appearance and disappearance of the liquid phase triggers the computation of additional Newton solver steps. The time step size is limited by the physics of the porous medium and not by the free flow. As the air crosses the porous medium, both physical compartments have similar time and length scales.

This does not mean that auspicious examples do not exists. Simulating the impact to the surface of a CO_2 storage with a leakage [Oldenburg and Unger, 2004] requires a large porous-medium subdomain, compared to the one for the free flow. For such setups with large Darcy domains, the influence of the free flow can maybe be incorporated as top boundary conditions [Tang and Riley, 2013].

6.2 Outlook

This work can be the basis for further research which might lead to a continued development of the software. The software can be extended—similar to the extensions to the predecessor code—to include salt precipitation for soil water evaporation [Jambhekar et al., 2015], drop formation at the interface for fuel cells [Baber, 2014], surface roughness [Fetzer, 2012], boundary layer models or Reynolds-averaged Navier-Stokes methods with eddy viscosity models like zero-equation models [Fetzer et al., 2016] or a k-ε model. Further possible extensions to the model could include solar radiation, which should be considered for soil-water evaporation in arid regions, as well as a way to include rainfall for the recharge of the soil water, which could include a tertiary coupled shallow water model [Sochala et al., 2009] that might require a coupling including vertical momentum transfer [Furman, 2008]. One could conduct a simulation of soil-water evaporation for a field with measured weather data, especially temperature, air humidity and wind velocity. This could also include day-night cycles and condensation of vapor caused by nocturnal cooling. Another possible extension is evapotranspiration, which also considers transpiration, i. e., living plants cause vaporization of water through their stomata. This affects the evaporation rate of surfaces covered with plants. A far-distance goal could be a complete simulation of the grain yield of a field, covering its water dynamics, root-water uptake, and crop growth [Zhang et al., 2015]. Future research could also investigate the effect of vegetation on the turbulence, e. g., it is reduced by the porous bed while it is increased by grass [Pechlivanidis et al., 2015]. Biological applications would be interesting as well.

The software can be improved by parallelization of the assembly and the solving. Replacing PDELab and Dune-Multidomain would lift the restriction on face-neighboring degrees of freedom which would allow for a replacement of the upwind scheme and would allow a decoupling of the subdomains with a Robin-Robin coupling, as the Dirichlet-Neumann coupling shows poor convergence [Ackermann, 2016, Discacciati, 2004]. For the marker and cell scheme, a generalization exists for triangles and tetrahedra or prisms respectively [Nicolaides, 1989, 1993]; while there is a restriction on the angles to obtain valid dual grids, its use would allow for geometries more general than axially parallel geometries.

To use a state-of-the-art discretization for the free flow together with DuMu^x, one has to consider coupling non-Dune software. Bungartz et al. [2016] describe preCICE which is a general framework for coupling different grid-based numerical simulators. It would be handy to couple DuMu^x with established free-flow simulators like OpenFOAM, Comsol or Fluent. Even without utilizing

preCICE, the described ideas of data interchange, non-matching grids, and coupling schemes are useful by themselves.

To attract people to develop methods for our system of linear equations, we submitted matrices from a two- and a three-dimensional coupled evaporation pipe test case to the SuiteSparse Matrix Collection, formerly known as the University of Florida Sparse Matrix Collection [Davis and Hu, 2011]. Matrices from this collection where used for benchmarks of linear solvers in Benzi et al. [2000] and Li and Shao [2011].

There is a lack of test cases with generally recognized results. The scientific groups have their own test cases, but they are seldom verified by other groups. If differences occur, like the ones described in section 5.3, it is unclear which result is preferred. It would be great to announce a benchmark problem that can be simulated by many groups and which can be set up in a laboratory to obtain data for comparison. Analytic solutions are probably out of reach, but direct numerical solutions can act as referee.

Invitation to use our results and our software

Hopefully we have made a fruitful contribution to the field of coupled Navier-Stokes flow with Darcy flow. We want other researchers to use our results to improve their work. We invite everybody to utilize our implementation, either for comparison with new numerical codes or to simulate applications of their own.

Omne tulit punctum qui miscuit utile dulci.

Horace, c. 19 BC

Colophon

This work is typeset with LaTeX 2_ε—the typesetting system originally developed by Leslie Lamport, based on TeX created by Donald Knuth—using TeX Live 2016 and pdfLaTeX 3.14159265. KOMA-Script 3.20 provides the document class scrbook. The figures were created with Ti*k*Z 3.0.1a, the graphs with PGFPlots 1.13, and the visualizations of two- and three-dimensional results were drawn with ParaView 5.3.0 and included as PNG images. The serif typeface of the text body is Linux Libertine, inspired by 19th century book types. Linux Bioline is used as the humanist sans-serif typeface for the headings and the quotes. The math font is newtxmath in Libertine mode.

LaTeX and Ti*k*Z are great tools for beautifully typeset documents and for thesis procrastination.

Quotes

We give the English translation of the quotes next to the chapter headings.

Chapter 1 Johann Wolfgang von Goethe: Water is a friendly element to whomever is familiar with it and is able to manage it.

Chapter 2 Genesis, 2:6 (KJV): But there went up a mist from the earth, and watered the whole face of the ground.

Chapter 5 Benoît Mandelbrot: In an ever-more complex world, scientists need both tools: image as well as number, the geometric view as well as the analytic.

Chapter 6 Marie Skłodowska Curie: One never notices what has been done; one can only see what remains to be done.

Colophon Horace: He wins every hand who blends the useful with the sweet.

I'm glad I'm not the clueless person I was five years ago,
but now I don't want to get any older.

Randall Munroe, xkcd #907

Acknowledgment

Danksagung

Diese Dissertation ist eine eigenständige Arbeit, aber sie ist nicht im luftleeren und reibungsfreien Raum entstanden. Ohne Anregungen, Reflexionen, Verbesserungen, Ermutigungen, Ermahnungen, Hilfen und nicht zuletzt Ablenkungen von außen wäre diese Arbeit unvollendet geblieben. Ich möchte mich herzlich bei den Menschen bedanken, die ein Stück des streckenweise beschwerlichen Wegs mit mir gegangen sind.

Meine tiefste Dankbarkeit möchte ich meiner geliebten Frau Aurelia bekunden, sie hat mir unendlich viel Verständnis und Geduld entgegengebracht. Meine Tochter hat mich motiviert mit ihrem Lächeln, das sie mir zu meinem täglichen Nachhausekommen geschenkt hat. Meinen Eltern danke ich für die ungebrochene Unterstützung. Meinen Geschwistern und Freunden bin ich dankbar für die Begleitung meiner Promotionszeit, insbesondere Albert, Miriam, Michael, Kai, Tobias, Alexander S., Marja und Alexander E.

Besonderer Dank gilt meinem Betreuer, Chef und Professor Rainer Helmig. Er bewies immer wieder aufs Neue, was für ein großartiger Wissenschaftler und Mensch er ist. Ich durfte viel von ihm lernen und zahlreiche durch ihn eröffnete Möglichkeiten wahrnehmen. Trotzdem war er mit mir geduldig, hat mich auf Augenhöhe behandelt und wir konnten auch abseits des Fachlichen mit Hingabe diskutieren. Mein Hauptbetreuer und die Ruhe im Sturm war Bernd Flemisch. Für ihn war kein Problem zu groß, es gab nie Grund sich aufzuregen. In der Anwendung, der Mathematik und beim Programmieren gleichermaßen bewandert, hat er mir viele Stunden gewidmet und mir dadurch noch viel mehr Stunden erspart.

I want to thank Béatrice Rivière for all the support she offered and for hosting me in Houston; it was a wonderful time and a lasting experience.

Meine Zeit am Institut habe ich sehr genossen, vor allem den Umgang mit meinen Kollegen. Thomas Fetzer war nicht nur Zimmer-, sondern auch Leidensgenosse. In ihm hatte ich einen exzellenten Ingenieur als Forschungspartner, der mich wunderbar ergänzte und der mich regelmäßig in den Dingen überflügelte, in die ich ihn eingeführt hatte. Die humorvollen Diskussionen mit meinen Kollegen Rainer E., Michael, Benjamin, Philipp, Frau Lawday, Karin S., Nicolas, Natalie, Martin B. und Gabriele waren das Salz in der Suppe. Klaus und Katherina haben wichtige Vorarbeiten geleistet und mir beim Einstieg ins Thema geholfen. Holger hat mich bezüglich Brennstoffzellen betreut. Er, Kilian und Thomas haben hilfreiche Anmerkungen zur Arbeit gemacht. Für die sprachlichen Korrekturen der Arbeit möchte ich mich bei Ned bedanken.

Mir war es vergönnt beim Dune-Projekt mitzuwirken, bei dem ich mit kompetenten und freundlichen Entwicklern in Kontakt kam. Es ist ein vorzügliches Stück Software mit einer tollen Gemeinschaft. Besonders Christian, Jö, Robert, Markus, Oliver, Dominic und Steffen verdanke ich viel. Letzterer hat dankenswerterweise jahrelang persönlichen Support für PDELab und seine Multidomain-Module geleistet.

Nomenclature

A	matrix of linear system, $A \in \mathbb{R}^{\eta \times \eta}$, p. 50	
b	right hand side of linear system, $b \in \mathbb{R}^{\eta}$, p. 50	
c	specific heat capacity, p. 13	$\mathrm{J/kg\,K}$
D	diffusion coefficient, p. 19	
F	force	$\mathrm{kg\,m/s^2}$
g	gravitational acceleration vector, p. 28	$\mathrm{m/s^2}$
H	Henry coefficient, p. 12	$\mathrm{1/Pa}$
h	specific enthalpy, p. 13	$\mathrm{J/kg}$
j	diffusive flux, p. 19	
k	intrinsic permeability, p. 14	$\mathrm{m^2}$
k_α	relative permeability, p. 17	–
M	molar mass, p. 10	$\mathrm{kg/mol}$
m	mass	kg
n	outer normal of porous medium subdomain regarding Γ, p. 36	–
n_{mole}	amount of substance, p. 10	mol
n_{VG}	Van Genuchten model parameter, relates to pore size distribution, p. 17	–
O	big O, upper bound of asymptotic growth rate	
p	pressure, p. 11	Pa
p_{c}	capillary pressure, p. 17	Pa
$p_{\mathrm{sat}}^{\mathrm{w}}$	saturated vapor pressure, p. 21	Pa
q	evaporation rate, p. 23	$\mathrm{mm/day}$
R_{s}	specific gas constant, p. 12	$\mathrm{J/kg\,K}$
Re	Reynolds number, p. 19	–
S	saturation, p. 15	–
T	temperature, p. 13	K
t	time	s
t^k	time step, a discrete point in time, p. 48	s
t_i	tangentials of the interface Γ with $t_i \perp t_j$ for $i \neq j$, p. 36	–
u	specific internal energy, p. 13	$\mathrm{J/kg}$
v	velocity $v = (v_1, v_2, \dots)^\intercal$, p. 11	$\mathrm{m/s}$
v^{pm}	Darcy velocity, p. 32	$\mathrm{m/s}$
$\tilde{v}^{\mathrm{pm}}$	seepage velocity, p. 32	$\mathrm{m/s}$
X	mass fraction, p. 10	–
x	space coordinate $x = (x_1, x_2, \dots)^\intercal$	m
x_{mole}	mole fraction, p. 10	–
z	vector of unknowns in the linear system, $z \in \mathbb{R}^{\eta}$, p. 50	

α	phase index, p. 10	
α_{VG}	Van Genuchten model parameter, relates to inverse entry pressure, p. 17	$^1/\mathrm{Pa}$
Γ	interface between porous-medium and free-flow subdomain, p. 36	
Δt^k	time step size between t^{k-1} and t^k, p. 48	s
η	number of unknowns in the linear system, p. 50	–
κ	component index, p. 10	
λ	thermal conductivity, p. 13	$\mathrm{J/s\,m\,K}$
λ_{pm}	effective porous-medium thermal conductivity, p. 18	$\mathrm{J/s\,m\,K}$
μ	dynamic viscosity, p. 11	Pa s
ϱ	density, p. 11	$\mathrm{kg/m^3}$
σ	stress, p. 11	Pa
τ	shear stress, p. 11	Pa
τ_{pm}	pore tortuosity, p. 19	–
ϕ	porosity, p. 14	–
χ_α	characteristic function for phase α, p. 15	–

div	divergence, for matrices $\mathrm{div}(U)_i \coloneqq \sum_j \frac{\partial}{\partial x_j} U_{i,j}$
grad	gradient, for vectors $\mathrm{grad}(v)_{i,j} \coloneqq \mathrm{grad}\,(v_i)_j$
ff, pm	free flow, porous medium subdomain superscript
a, w	air, water component superscript
g, l, s	gas, liquid, solid phase subscript

When symbols are only used in close proximity to their definition, they have been omitted from the nomenclature.

Bibliography

S. Ackermann. Development and evaluation of iterative solution strategies for coupled Stokes-Darcy problems. Master's thesis, University of Stuttgart, 2016.

S. Ackermann, M. Beck, B. Becker, H. Class, T. Fetzer, B. Flemisch, D. Gläser, C. Grüninger, K. Heck, R. Helmig, J. Hommel, A. Kissinger, T. Koch, M. Schneider, G. Seitz, and K. Weishaupt. DuMuX 2.11.0, 2017. doi: 10.5281/zenodo.439488.

M. Acosta, C. Merten, G. Eigenberger, H. Class, R. Helmig, B. Thoben, and H. Müller-Steinhagen. Modeling non-isothermal two-phase multicomponent flow in the cathode of PEM fuel cells. *Journal of Power Sources*, 159(2):1123–1141, 2006. doi: 10.1016/j.jpowsour.2005.12.068.

E. Agullo, P. R. Amestoy, A. Buttari, A. Guermouche, G. Joslin, J.-Y. L'Excellent, X. S. Li, A. Napov, F.-H. Rouet, W. M. Sid-Lakhdar, S. Wang, C. Weisbecker, and I. Yamazaki. Recent advances in sparse direct solvers. In *22nd Conference on Structural Mechanics in Reactor Technology*, page 10, San Francisco, United States, 2013.

B. Alazmi and K. Vafai. Analysis of fluid flow and heat transfer interfacial conditions between a porous medium and a fluid layer. *International Journal of Heat and Mass Transfer*, 44(9): 1735–1749, 2001. doi: 10.1016/S0017-9310(00)00217-9.

C. Argyropoulos and N. Markatos. Recent advances on the numerical modelling of turbulent flows. *Applied Mathematical Modelling*, 39(2):693–732, 2015. doi: 10.1016/j.apm.2014.07.001.

D. Aronson and L. Löfdahl. The plane wake of a cylinder: Measurements and inferences on turbulence modeling. *Physics of Fluids A*, 5(6):1433–1437, 1993. doi: 10.1063/1.858579.

K. Baber. *Coupling free flow and flow in porous media in biological and technical applications: from a simple to a complex interface description.* PhD thesis, University of Stuttgart, 2014. doi: 10.18419/opus-594.

K. Baber, K. Mosthaf, B. Flemisch, R. Helmig, S. Müthing, and B. Wohlmuth. Numerical scheme for coupling two-phase compositional porous-media flow and one-phase compositional free flow. *IMA Journal of Applied Mathematics*, 77(6):887–909, 2012. doi: 10.1093/imamat/hxs048.

L. Badea, M. Discacciati, and A. Quarteroni. Numerical analysis of the Navier–Stokes/Darcy coupling. *Numerische Mathematik*, 115(2):195–227, 2010. doi: 10.1007/s00211-009-0279-6.

P. Ball. Water and life: Seeking the solution. *Nature*, 436(7054):1084–1085, Aug 2005. doi: 10.1038/4361084a.

H. Basser, E. Daly, C. Lu, and H. H. Bui. SPH modeling of multi-phase flow over a porous layer. In *The XXI International Conference Computational Methods in Water Resources, CMWR 2016, Toronto, Canada*, 2016.

P. Bastian, M. Blatt, A. Dedner, C. Engwer, R. Klöfkorn, R. Kornhuber, M. Ohlberger, and O. Sander. A generic grid interface for parallel and adaptive scientific computing. Part II: Implementation and tests in DUNE. *Computing*, 82(2–3):121–138, 2008a. doi: 10.1007/s00607-008-0004-9.

P. Bastian, M. Blatt, A. Dedner, C. Engwer, R. Klöfkorn, M. Ohlberger, and O. Sander. A generic grid interface for parallel and adaptive scientific computing. Part I: Abstract framework. *Computing*, 82(2–3):103–119, 2008b. doi: 10.1007/s00607-008-0003-x.

P. Bastian, F. Heimann, and S. Marnach. Generic implementation of finite element methods in the Distributed and Unified Numerics Environment (DUNE). *Kybernetika*, 46(2):294–315, 2010. URL `http://hdl.handle.net/10338.dmlcz/140745`.

J. Bear. *Dynamics of Fluids in Porous Media*. Dover, 1972. ISBN 9780486656755.

G. S. Beavers and D. D. Joseph. Boundary conditions at a naturally permeable wall. *Journal of Fluid Mechanics*, 30(1):197–207, 1967. doi: 10.1017/S0022112067001375.

M. Benzi, J. C. Haws, and M. Tůma. Preconditioning highly indefinite and nonsymmetric matrices. *SIAM Journal on Scientific Computing*, 22(4):1333–1353, 2000. doi: 10.1137/S1064827599361308.

M. Benzi, G. H. Golub, and J. Liesen. Numerical solution of saddle point problems. *Acta Numerica*, 14:1–137, 2005. doi: 10.1017/S0962492904000212.

R. B. Bird, W. E. Stewart, and E. N. Lightfoot. *Transport Phenomena*. Wiley, 2007. ISBN 9780470115398.

N. Birgle, R. Masson, and L. Trenty. A nonlinear domain decomposition method to couple compositional gas liquid Darcy and free gas flows. In C. Cancès and P. Omnes, editors, *Finite Volumes for Complex Applications VIII – Hyperbolic, Elliptic and Parabolic Problems: FVCA 8, Lille, France, June 2017*, pages 387–395, 2017. ISBN 9783319573946. doi: 10.1007/978-3-319-57394-6_41.

M. Blatt. *A parallel algebraic multigrid method for elliptic problems with highly discontinuous coefficients*. PhD thesis, Heidelberg University, July 2010. doi: 10.11588/heidok.00010856.

M. Blatt and P. Bastian. The iterative solver template library. In B. Kågström, E. Elmroth, J. Dongarra, and J. Waśniewski, editors, *Applied Parallel Computing. State of the Art in Scientific Computing: 8th International Workshop, PARA 2006, Umeå, Sweden, June 18-21, 2006, Revised Selected Papers*, pages 666–675. Springer, 2007. ISBN 9783540757559. doi: 10.1007/978-3-540-75755-9_82.

M. Blatt, A. Burchardt, A. Dedner, C. Engwer, J. Fahlke, B. Flemisch, C. Gersbacher, C. Gräser, F. Gruber, C. Grüninger, D. Kempf, R. Klöfkorn, T. Malkmus, S. Müthing, M. Nolte, M. Piatkowski, and O. Sander. The Distributed and Unified Numerics Environment, Version 2.4. *Archive of Numerical Software*, 100(4):13–29, 2016. doi: 10.11588/ans.2016.100.26526.

M. Braack and A. Ern. A posteriori control of modeling errors and discretization errors. *Multiscale Modeling & Simulation*, 1(2):221–238, 2003. doi: 10.1137/S1540345902410482.

J. Bramble, J. Pasciak, and A. Vassilev. Uzawa type algorithms for nonsymmetric saddle point problems. *Mathematics of Computation of the American Mathematical Society*, 69(230):667–689, 2000. doi: 0.1090/S0025-5718-99-01152-7.

H. C. Brinkman. A calculation of the viscous force exerted by a flowing fluid on a dense swarm of particles. *Flow, Turbulence and Combustion*, 1(1):27–34, 1949. doi: 10.1007/BF02120313.

R. H. Brooks and A. T. Corey. *Hydraulic Properties of Porous Media.* Colorado State University Hydrology Papers. Colorado State University, 1964.

W. Brutsaert. *Evaporation into the Atmosphere: Theory, History and Applications.* Springer, 1982. ISBN 9789027712479.

H.-J. Bungartz, F. Lindner, B. Gatzhammer, M. Mehl, K. Scheufele, A. Shukaev, and B. Uekermann. preCICE - A fully parallel library for multi-physics surface coupling. *Computers & Fluids*, 141: 250–258, 2016. doi: 10.1016/j.compfluid.2016.04.003.

Y. Cao, M. Gunzburger, F. Hua, and X. Wang. Coupled Stokes-Darcy model with Beavers-Joseph interface boundary condition. *Communications in Mathematical Sciences*, 8(1):1–25, 2010. doi: 10.4310/CMS.2010.v8.n1.a2.

P. C. Carman. Fluid flow through granular beds. *Transactions, Institution of Chemical Engineers*, 15: 150–166, 1937. doi: 10.1016/S0263-8762(97)80003-2. Reprinted in *Chemical Engineering Research and Design*, 75:S32–S48, 1997.

A. Çeşmelioğlu and B. Rivière. Existence of a weak solution for the fully coupled Navier–Stokes/Darcy-transport problem. *Journal of Differential Equations*, 252(7):4138–4175, 2012. doi: 10.1016/j.jde.2011.12.001.

H. Chan, W. Huang, J. Leu, and C. Lai. Macroscopic modeling of turbulent flow over a porous medium. *International Journal of Heat and Fluid Flow*, 28(5):1157–1166, 2007. doi: 10.1016/j.ijheatfluidflow.2006.10.005.

M. Chandesris, A. D'Hueppe, B. Mathieu, D. Jamet, and B. Goyeau. Direct numerical simulation of turbulent heat transfer in a fluid-porous domain. *Physics of Fluids*, 25(12), 2013. doi: 10.1063/1.4851416.

Z. Chen. *Finite element methods and their applications.* Springer, 2005. ISBN 9783540240780.

P. Chidyagwai and B. Rivière. A two-grid method for coupled free flow with porous media flow. *Advances in Water Resources*, 34(9):1113–1123, 2011. doi: 10.1016/j.advwatres.2011.04.010.

F. Cimolin and M. Discacciati. Navier–Stokes/Forchheimer models for filtration through porous media. *Applied Numerical Mathematics*, 72:205–224, 2013. doi: 10.1016/j.apnum.2013.07.001.

H. Class and R. Helmig. Numerical simulation of non-isothermal multiphase multicomponent processes in porous media. 2. Applications for the injection of steam and air. *Advances in Water Resources*, 25(5):551–564, 2002. doi: 10.1016/S0309-1708(02)00015-5.

H. Class, R. Helmig, and P. Bastian. Numerical simulation of non-isothermal multiphase multicomponent processes in porous media. 1. An efficient solution technique. *Advances in Water Resources*, 25(5):533–550, 2002. doi: 10.1016/S0309-1708(02)00014-3.

W. Dahmen, T. Gotzen, S. Müller, and M. Rom. Numerical simulation of transpiration cooling through porous material. *International Journal for Numerical Methods in Fluids*, 76(6):331–365, 2014. doi: 10.1002/fld.3935.

H. Darcy. *Les fontaines publiques de la ville de Dijon: exposition et application des principes à suivre et des formules à employer dans les questions de distribution d'eau.* Victor Dalmont, 1856.

D. Das, V. Nassehi, and R. Wakeman. A finite volume model for the hydrodynamics of combined free and porous flow in sub-surface regions. *Advances in Environmental Research*, 7(1):35–58, 2002. doi: 10.1016/S1093-0191(01)00108-3.

H. Davarzani, K. Smits, R. M. Tolene, and T. Illangasekare. Study of the effect of wind speed on evaporation from soil through integrated modeling of the atmospheric boundary layer and shallow subsurface. *Water Resources Research*, 50(1):661–680, 2014. doi: 10.1002/2013WR013952.

T. A. Davis. A column pre-ordering strategy for the unsymmetric-pattern multifrontal method. *ACM Transactions on Mathematical Software*, 30(2):165–195, 2004. doi: 10.1145/992200.992205.

T. A. Davis and Y. Hu. The University of Florida sparse matrix collection. *ACM Transactions on Mathematical Software*, 38(1):1:1–1:25, 2011. doi: 10.1145/2049662.2049663.

T. A. Davis, S. Rajamanickam, and W. M. Sid-Lakhdar. A survey of direct methods for sparse linear systems. *Acta Numerica*, 25:383–566, 2016. doi: 10.1017/S0962492916000076.

M. De Lemos. Turbulent flow around fluid–porous interfaces computed with a diffusion-jump model for k and ε transport equations. *Transport in Porous Media*, 78:331–346, 2009. doi: 10.1007/s11242-009-9379-0.

T. Defraeye. Advanced computational modelling for drying processes – a review. *Applied Energy*, 131(C):323–344, 2014. doi: 10.1016/j.apenergy.2014.06.027.

T. Defraeye, B. Blocken, and J. Carmeliet. Analysis of convective heat and mass transfer coefficients for convective drying of a porous flat plate by conjugate modelling. *International Journal of Heat and Mass Transfer*, 55(1–3):112–124, 2012. doi: 10.1016/j.ijheatmasstransfer.2011.08.047.

T. Defraeye, B. Nicolaï, D. Mannes, W. Aregawi, P. Verboven, and D. Derome. Probing inside fruit slices during convective drying by quantitative neutron imaging. *Journal of Food Engineering*, 178:198–202, 2016. doi: 10.1016/j.jfoodeng.2016.01.023.

J. W. Delleur. *The Handbook of Groundwater Engineering*. CRC Press, second edition, 2006. ISBN 1420006001.

J. W. Demmel, S. C. Eisenstat, J. R. Gilbert, X. S. Li, and J. W. H. Liu. A supernodal approach to sparse partial pivoting. *SIAM Journal on Matrix Analysis and Applications*, 20(3):720–755, 1999. doi: 10.1137/S0895479895291765.

A. D'Hueppe. *Heat transfer modeling at an interface between a porous medium and a free region.* PhD thesis, Ecole Centrale Paris, 2011. URL `https://tel.archives-ouvertes.fr/tel-00711470/`.

M. Discacciati. Iterative methods for Stokes/Darcy coupling. In *Domain Decomposition Methods in Science and Engineering*, volume 40, pages 563–570. Springer, 2004. doi: 10.1007/3-540-26825-1_59.

M. Discacciati and A. Quarteroni. Convergence analysis of a subdomain iterative method for the finite element approximation of the coupling of Stokes and Darcy equations. *Computing and Visualization in Science*, 6(2):93–103, 2004. doi: 10.1007/s00791-003-0113-0.

M. Discacciati and A. Quarteroni. Navier-Stokes/Darcy coupling: modeling, analysis, and numerical approximation. *Revista Matemática Complutense*, 22(2):315–426, 2009. doi: 10.5209/rev_REMA.2009.v22.n2.16263.

M. Discacciati, A. Quarteroni, and A. Valli. Robin-Robin domain decomposition methods for the Stokes-Darcy coupling. *SIAM Journal on Numerical Analysis*, 45(3):1246–1268, 2007. doi: 10.1137/06065091X.

M. Discacciati, P. Gervasio, A. Giacomini, and A. Quarteroni. The interface control domain decomposition method for Stokes–Darcy coupling. *SIAM Journal on Numerical Analysis*, 54(2):1039–1068, 2016. doi: 10.1137/15M101854X.

V. Dolean, P. Jolivet, and F. Nataf. *An Introduction to Domain Decomposition Methods: Algorithms, Theory, and Parallel Implementation.* Society for Industrial and Applied Mathematics, 2015. ISBN 9781611974058.

I. S. Duff and J. Koster. The design and use of algorithms for permuting large entries to the diagonal of sparse matrices. *SIAM Journal on Matrix Analysis and Applications*, 20(4):889–901, 1999. doi: 10.1137/S0895479897317661.

I. S. Duff and J. Koster. On algorithms for permuting large entries to the diagonal of a sparse matrix. *SIAM Journal on Matrix Analysis and Applications*, 22(4):973–996, 2001. doi: 10.1137/S0895479899358443.

V. J. Ervin, M. Kubacki, W. Layton, M. Moraiti, Z. Si, and C. Trenchea. On limiting behavior of contaminant transport models in coupled surface and groundwater flows. *Axioms*, 4(4):518, 2015. doi: 10.3390/axioms4040518.

L. C. Evans. *Partial Differential Equations.* American Mathematical Society, 2010. ISBN 9780821849743.

B. Faigle, M. A. Elfeel, R. Helmig, B. Becker, B. Flemisch, and S. Geiger. Multi-physics modeling of non-isothermal compositional flow on adaptive grids. *Computer Methods in Applied Mechanics and Engineering*, 292:16–34, 2015. doi: 10.1016/j.cma.2014.11.030.

E. Fattahi, C. Waluga, B. I. Wohlmuth, and U. Rüde. Large scale lattice Boltzmann simulation for the coupling of free and porous media flow. In T. Kozubek, R. Blaheta, J. Šístek, M. Rozložník, and M. Čermák, editors, *High Performance Computing in Science and Engineering: Second International Conference, HPCSE 2015, Soláň, Czech Republic, May 25-28, 2015, Revised Selected Papers*, pages 1–18. Springer, 2016. ISBN 9783319403618. doi: 10.1007/978-3-319-40361-8_1.

C. L. Fefferman. Existence and smoothness of the Navier-Stokes equation. Technical report, Clay Mathematics Institute, 2000. URL `www.claymath.org/sites/default/files/navierstokes.pdf`.

J. Ferziger and M. Perić. *Computational methods for fluid dynamics*. Springer, 2002. ISBN 9783540420743.

T. Fetzer. Numerical analysis of the influence of turbulence on exchange processes between porous-medium and free flow. Master's thesis, University of Stuttgart, 2012.

T. Fetzer, K. M. Smits, and R. Helmig. Effect of turbulence and roughness on coupled porous-medium/free-flow exchange processes. *Transport in Porous Media*, pages 1–30, 2016. doi: 10.1007/s11242-016-0654-6.

T. Fetzer, C. Grüninger, B. Flemisch, and R. Helmig. On the conditions for coupling free flow and porous-medium flow in a finite volume framework. In C. Cancès and P. Omnes, editors, *Finite Volumes for Complex Applications VIII – Hyperbolic, Elliptic and Parabolic Problems: FVCA 8, Lille, France, June 2017*, pages 347–356, 2017a. ISBN 9783319573946. doi: 10.1007/978-3-319-57394-6_37.

T. Fetzer, J. Vanderborght, K. Mosthaf, K. M. Smits, and R. Helmig. Heat and water transport in soils and across the soil-atmosphere interface: 2. numerical analysis. *Water Resources Research*, 53(2):1080–1100, 2017b. doi: 10.1002/2016WR019983.

S. Finsterle. Inverse Modellierung zur Bestimmung hydrogeologischer Parameter eines Zweiphasensystems. Zürich, 1993. doi: 10.3929/ethz-a-000693070.

B. Flemisch, M. Darcis, K. Erbertseder, B. Faigle, A. Lauser, K. Mosthaf, S. Müthing, P. Nuske, A. Tatomir, M. Wolff, and R. Helmig. DuMu^x: DUNE for multi-{phase, component, scale, physics, ...} flow and transport in porous media. *Advances in Water Resources*, 34(9):1102–1112, 2011. doi: 10.1016/j.advwatres.2011.03.007.

J. Freund and R. Stenberg. On weakly imposed boundary conditions for second order problems. In *Proceedings of the 9th International Conference on Finite Elements in Fluids*, pages 327–336, 1995.

M. Fritsch. Analysis of processes and properties at a porous-medium free-flow interface with the application of evaporation. Master's thesis, University of Stuttgart, 2016.

A. Furman. Modeling coupled surface-subsurface flow processes: A review. *Vadose Zone Journal*, 7(2):741–756, 2008. doi: 10.2136/vzj2007.0065.

C. Grüninger, T. Fetzer, B. Flemisch, and R. Helmig. Coupling DuMuX and DUNE-PDELab to investigate evaporation at the interface between Darcy and Navier-Stokes flow. Technical Report 2017 - 1, SimTech, University of Stuttgart, 2017. doi: 10.18419/opus-9360.

S. Hahn, J. Je, and H. Choi. Direct numerical simulation of turbulent channel flow with permeable walls. *Journal of Fluid Mechanics*, 450:259–285, 2002. doi: 10.1017/S0022112001006437.

F. H. Harlow and J. E. Welch. Numerical calculation of time-dependent viscous incompressible flow of fluid with free surface. *Physics of Fluids*, 8(12):2182–2189, 1965. doi: 10.1063/1.1761178.

S. Hassanizadeh and W. G. Gray. Mechanics and thermodynamics of multiphase flow in porous media including interphase boundaries. *Advances in Water Resources*, 13(4):169–186, 1990. doi: 10.1016/0309-1708(90)90040-B.

S. M. Hassanizadeh and W. G. Gray. Derivation of conditions describing transport across zones of reduced dynamics within multiphase systems. *Water Resources Research*, 25(3):529–539, 1989a. doi: 10.1029/WR025i003p00529.

S. M. Hassanizadeh and W. G. Gray. Boundary and interface conditions in porous media. *Water Resources Research*, 25(7):1705–1715, 1989b. doi: 10.1029/WR025i007p01705.

R. Helmig. *Multiphase flow and transport processes in the subsurface: a contribution to the modeling of hydrosystems*. Springer, 1997. ISBN 9783540627036.

J. G. Heywood, R. Rannacher, and S. Turek. Artificial boundaries and flux and pressure conditions for the incompressible Navier–Stokes equations. *International Journal for Numerical Methods in Fluids*, 22(5):325–352, 1996. doi: 10.1002/(SICI)1097-0363(19960315)22:5<325::AID-FLD307>3.0.CO;2-Y.

E. Holzbecher. *Modellierung dynamischer Prozesse in der Hydrologie*. Springer, 1996. ISBN 9783540605164.

U. Hornung. *Homogenization and Porous Media*. Springer, 2012. ISBN 9781461219200.

V. E. Howle, R. C. Kirby, and G. Dillon. Block preconditioners for coupled physics problems. *SIAM Journal on Scientific Computing*, 35(5):S368–S385, 2013. doi: 10.1137/120883086.

C. Hutton, T. Wagener, J. Freer, D. Han, C. Duffy, and B. Arheimer. Most computational hydrology is not reproducible, so is it really science? *Water Resources Research*, 52(10):7548–7555, 2016. doi: 10.1002/2016WR019285.

IAPWS. Revised release on the IAPWS industrial formulation 1997 for the thermodynamic properties of water and steam, 2007. URL `http://www.iapws.org/relguide/IF97-Rev.pdf`.

V. A. Jambhekar, R. Helmig, N. Schröder, and N. Shokri. Free-flow–porous-media coupling for evaporation-driven transport and precipitation of salt in soil. *Transport in Porous Media*, 110(2): 251–280, 2015. doi: 10.1007/s11242-015-0516-7.

Ø. Johansen. *Varmeledningsevne av Jordarter*. PhD thesis, Norwegian University of Science and Technology, Trondheim, 1975. Translated as *Thermal conductivity of soils* by U.S. Army, Cold Regions Research and Engineering Laboratory, 1977.

I. P. Jones. Low Reynolds number flow past a porous spherical shell. *Mathematical Proceedings of the Cambridge Philosophical Society*, 73(1):231–238, 1973. doi: 10.1017/S0305004100047642.

W. Jäger and A. Mikelić. On the interface boundary condition of Beavers, Joseph, and Saffman. *SIAM Journal on Applied Mathematics*, 60(4):1111–1127, 2000. doi: 10.1137/S003613999833678X.

W. Jäger, A. Mikelić, and N. Neuss. Asymptotic analysis of the laminar viscous flow over a porous bed. *SIAM Journal on Scientific Computing*, 22(6):2006–2028, 2001. doi: 10.1137/S1064827599360339.

G. Kanschat. Divergence-free discontinuous Galerkin schemes for the Stokes equations and the mac scheme. *International Journal for Numerical Methods in Fluids*, 56(7):941–950, 2008. doi: 10.1002/fld.1566.

G. Kanschat and B. Rivière. A strongly conservative finite element method for the coupling of Stokes and Darcy flow. *Journal of Computational Physics*, 229(17):5933–5943, 2010. doi: 10.1016/j.jcp.2010.04.021.

W. M. Kays, M. E. Crawford, and B. Weigand. *Convective heat and mass transfer*. McGraw-Hill Higher Education, 4th edition, 2005. ISBN 9780071238298.

J. B. Keller. Darcy's law for flow in porous media and the two-space method. In R. L. Sternberg, A. J. Kalinowski, and J. S. Papadakis, editors, *Nonlinear Partial Differential Equations in Engineering and Applied Science*, pages 429–443. CRC Press, 1980. ISBN 9780824769963.

I. N. Konshin, M. A. Olshanskii, and Y. V. Vassilevski. ILU preconditioners for nonsymmetric saddle-point matrices with application to the incompressible Navier-Stokes equations. *SIAM Journal on Scientific Computing*, 37(5):A2171–A2197, 2015. doi: 10.1137/15M1012311.

M. Krafczyk, K. Kucher, Y. Wang, and M. Geier. DNS/LES studies of turbulent flows based on the cumulant lattice Boltzmann approach. In W. E. Nagel, D. H. Kröner, and M. M. Resch, editors, *High Performance Computing in Science and Engineering '14*, pages 519–531. Springer, 2014.

M. Krotkiewski, I. S. Ligaarden, K.-A. Lie, and D. W. Schmid. On the importance of the Stokes-Brinkman equations for computing effective permeability in karst reservoirs. *Communications in Computational Physics*, 10(5):1315–1332, 2015. doi: 10.4208/cicp.290610.020211a.

P. Krzyzanowski. On block preconditioners for nonsymmetric saddle point problems. *SIAM Journal on Scientific Computing*, 23(1):157–169, 2001. doi: 10.1137/S1064827599360406.

J. Laufer. The structure of turbulence in fully developed pipe flow. *NACA Technical Report 1174*, 1954.

W. J. Layton, F. Schieweck, and I. Yotov. Coupling fluid flow with porous media flow. *SIAM Journal on Numerical Analysis*, 40(6):2195–2218, 2002. URL `http://www.jstor.org/stable/4100990`.

P. Lehmann, S. Assouline, and D. Or. Characteristic lengths affecting evaporative drying of porous media. *Physical Review E*, 77:056309, 2008. doi: 10.1103/PhysRevE.77.056309.

R. J. LeVeque. *Finite Volume Methods for Hyperbolic Problems*. Cambridge University Press, 2002. ISBN 9781139434188.

X. S. Li and M. Shao. A supernodal approach to incomplete LU factorization with partial pivoting. *ACM Transactions on Mathematical Software*, 37(4):43:1–43:20, 2011. doi: 10.1145/1916461.1916467.

C. Liu, Y. Yan, and P. Lu. Physics of turbulence generation and sustenance in a boundary layer. *Computers & Fluids*, 102:353–384, 2014. doi: 10.1016/j.compfluid.2014.06.032.

R. Masson and N. Birgle. Private communication, 2017.

R. Masson, L. Trenty, and Y. Zhang. Coupling compositional liquid gas Darcy and free gas flows at porous and free-flow domains interface. *Journal of Computational Physics*, 321:708–728, 2016. doi: 10.1016/j.jcp.2016.06.003.

S. Mazumder. *Numerical Methods for Partial Differential Equations: Finite Difference and Finite Volume Methods*. Elsevier Science, 2015. ISBN 9780128035047.

K. Mosthaf. *Modeling and analysis of coupled porous-medium and free flow with application to evaporation processes*. PhD thesis, University of Stuttgart, 2014. doi: 10.18419/opus-519.

K. Mosthaf, K. Baber, B. Flemisch, R. Helmig, A. Leijnse, I. Rybak, and B. Wohlmuth. A coupling concept for two-phase compositional porous-medium and single-phase compositional free flow. *Water Resources Research*, W10522, 2011. doi: 10.1029/2011WR010685.

K. Mosthaf, R. Helmig, and D. Or. Modeling and analysis of evaporation processes from porous media on the REV scale. *Water Resources Research*, 2014. doi: 10.1002/2013WR014442.

S. Müthing. *A Flexible Framework for Multi Physics and Multi Domain PDE Simulations*. PhD thesis, University of Stuttgart, January 2015. doi: 10.18419/opus-3620.

S. Müthing and P. Bastian. Dune-Multidomaingrid: A metagrid approach to subdomain modeling. In A. Dedner, B. Flemisch, and R. Klöfkorn, editors, *Advances in DUNE: Proceedings of the DUNE User Meeting, Held in October 6th–8th 2010 in Stuttgart, Germany*, pages 59–73. Springer, 2012. ISBN 9783642285899. doi: 10.1007/978-3-642-28589-9_5.

J. R. Natvig and K.-A. Lie. Fast computation of multiphase flow in porous media by implicit discontinuous Galerkin schemes with optimal ordering of elements. *Journal of Computational Physics*, 227(24):10108–10124, 2008. doi: 10.1016/j.jcp.2008.08.024.

T. V. Nguyen. A gas distributor design for proton-exchange-membrane fuel cells. *Journal of The Electrochemical Society*, 143(5):L103–L105, 1996. doi: 10.1149/1.1836666.

R. A. Nicolaides. Flow discretization by complementary volume techniques. In *Proceedings of 9th AIAA CFD Meeting*, pages 464–470, 1989. doi: 10.2514/6.1989-1978.

R. A. Nicolaides. Analysis and convergence of the MAC scheme. I. The linear problem. *SIAM Journal on Numerical Analysis*, 29(6):1579–1591, 1992. doi: 10.1137/0729091.

R. A. Nicolaides. Three dimensional covolume algorithms for viscous flows. In M. Y. Hussaini, A. Kumar, and M. D. Salas, editors, *Algorithmic Trends in Computational Fluid Dynamics*, pages 397–414. Springer, 1993. ISBN 9781461227083.

R. A. Nicolaides and X. Wu. Analysis and convergence of the MAC scheme. II. Navier-Stokes equations. *Math. Comput.*, 65(213):29–44, 1996. doi: 10.1090/S0025-5718-96-00665-5.

D. A. Nield. The Beavers-Joseph boundary condition and related matters: A historical and critical note. *Transport in Porous Media*, 78(3):537–540, 2009. doi: 10.1007/s11242-009-9344-y.

D. A. Nield and A. V. Kuznetsov. The effect of a transition layer between a fluid and a porous medium: shear flow in a channel. *Transport in Porous Media*, 78(3):477–487, 2009. doi: 10.1007/s11242-009-9342-0.

C. M. Oldenburg and A. Unger. Coupled vadose zone and atmospheric surface-layer transport of carbon dioxide from geologic carbon sequestration sites. *Vadose Zone Journal*, 3(3), 2004. doi: 10.2136/vzj2004.0848.

D. Or, P. Lehmann, E. Shahraeeni, and N. Shokri. Advances in soil evaporation physics—a review. *Vadose Zone Journal*, 12(4), 2013. doi: 10.2136/vzj2012.0163.

G. Pechlivanidis, E. Keramaris, and I. Pechlivanidis. Experimental study of the effects of grass vegetation and gravel bed on the turbulent flow using particle image velocimetry. *Journal of Turbulence*, 16(1):1–14, 2015. doi: 10.1080/14685248.2014.946605.

D. Pokrajac and C. Manes. Velocity measurements of a free-surface turbulent flow penetrating a porous medium composed of uniform-size spheres. *Transport in Porous Media*, 78(3):367–383, 2009. doi: 10.1007/s11242-009-9339-8.

S. B. Pope. *Turbulent Flows*. Cambridge University Press, 2000. ISBN 9780521598866.

M. Prat. Recent advances in pore-scale models for drying of porous media. *Chemical Engineering Journal*, 86(1–2):153–164, 2002. doi: 10.1016/S1385-8947(01)00283-2.

P. Prinos, D. Sofialidis, and E. Keramaris. Turbulent flow over and within a porous bed. *Journal of Hydraulic Engineering*, 129(9):720, 2003.

A. Quarteroni, F. Pasquarelli, and A. Valli. Heterogeneous domain decomposition principles, algorithms, applications. In D. E. Keyes, T. F. Chan, G. A. Meurant, J. S. Scroggs, and R. G. Voigt, editors, *Fifth International Symposium on Domain Decomposition Methods for Partial Differential Equations*, pages 129–150, Philadelphia, PA, 1992. SIAM.

R. Reid, J. Prausnitz, and B. Poling. *The properties of gases and liquids.* McGraw Hill, 1987.

D. Rind, C. Rosenzweig, and M. Stieglitz. The role of moisture transport between ground and atmosphere in global change. *Annual Review of Energy and the Environment*, 22(1):47–74, 1997. doi: 10.1146/annurev.energy.22.1.47.

I. Rybak and J. Magiera. A multiple-time-step technique for coupled free flow and porous medium systems. *Journal of Computational Physics*, 272:327–342, 2014. doi: 10.1016/j.jcp.2014.04.036.

I. Rybak, J. Magiera, R. Helmig, and C. Rohde. Multirate time integration for coupled saturated/unsaturated porous medium and free flow systems. *Computational Geosciences*, 19(2): 299–309, 2015. doi: 10.1007/s10596-015-9469-8.

Y. Saad. *Iterative Methods for Sparse Linear Systems.* Society for Industrial and Applied Mathematics, second edition, 2003. ISBN 97808987153347. doi: 10.1137/1.9780898718003.

P. G. Saffman. On the boundary condition at the surface of a porous medium. *Studies in Applied Mathematics*, 50(2):93–101, 1971. doi: 10.1002/sapm197150293.

A. G. Salinger, R. Aris, and J. J. Derby. Finite element formulations for large-scale, coupled flows in adjacent porous and open fluid domains. *International Journal for Numerical Methods in Fluids*, 18(12):1185–1209, 1994. doi: 10.1002/fld.1650181205.

H. A. Schwarz. *Ueber einen Grenzübergang durch alternirendes Verfahren.* Vierteljahrsschrift der Naturforschenden Gesellschaft in Zürich. Zürcher und Furrer, 1870.

E. Shahraeeni, P. Lehmann, and D. Or. Coupling of evaporative fluxes from drying porous surfaces with air boundary layer: Characteristics of evaporation from discrete pores. *Water Resources Research*, 48:W09525, 15 pp, 2012. doi: 10.1029/2012WR011857.

S. Shao. Incompressible SPH flow model for wave interactions with porous media. *Coastal Engineering*, 57(3):304–316, 2010. doi: 10.1016/j.coastaleng.2009.10.012.

H. E. Siekmann and P. U. Thamsen. *Strömungslehre: Grundlagen.* Springer, 2008. ISBN 9783540737278.

B. F. Smith, P. E. Bjørstad, and W. Gropp. *Domain decomposition: parallel multilevel methods for elliptic partial differential equations.* Cambridge University Press, 1996. ISBN 9780521495899.

K. M. Smits, A. Cihan, T. Sakaki, S. E. Howington, J. F. Peters, and T. H. Illangasekare. Soil moisture and thermal behavior in the vicinity of buried objects affecting remote sensing detection: Experimental and modeling investigation. *IEEE Transactions on Geoscience and Remote Sensing*, 51(5):2675–2688, 2013. doi: 10.1109/TGRS.2012.2214485.

P. Sochala, A. Ern, and S. Piperno. Mass conservative BDF-discontinuous Galerkin/explicit finite volume schemes for coupling subsurface and overland flows. *Computer Methods in Applied Mechanics and Engineering*, 198(27–29):2122–2136, 2009. doi: 10.1016/j.cma.2009.02.024.

P. R. Spalart. Philosophies and fallacies in turbulence modeling. *Progress in Aerospace Sciences*, 74: 1–15, 2015. doi: 10.1016/j.paerosci.2014.12.004.

K. Suga. Understanding and modelling turbulence over and inside porous media. *Flow, Turbulence and Combustion*, 96(3):717–756, 2016. doi: 10.1007/s10494-015-9673-6.

J. Y. Tang and W. J. Riley. A new top boundary condition for modeling surface diffusive exchange of a generic volatile tracer: theoretical analysis and application to soil evaporation. *Hydrology and Earth System Sciences*, 17(2):873–893, 2013. doi: 10.5194/hess-17-873-2013.

A. Toselli and O. Widlund. *Domain Decomposition Methods – Algorithms and Theory*. Springer, 2004. ISBN 9783540206965.

R. Usha, A. Anjalaiah, and Y. V. S. S. Sanyasiraju. Dynamics of a pre-lens tear film after a blink: Model, evolution, and rupture. *Physics of Fluids*, 25(11), 2013. doi: 10.1063/1.4831795.

S. V. Utyuzhnikov. Robin-type wall functions and their numerical implementation. *Applied Numerical Mathematics*, 58(10):1521–1533, 2008. doi: 10.1016/j.apnum.2007.09.003.

M. T. Van Genuchten. A closed-form equation for predicting the hydraulic conductivity of unsaturated soils. *Soil Science Society of America Journal*, 44(5):892–898, 1980. doi: 10.2136/sssaj1980.03615995004400050002x.

J. Vanderborght, T. Fetzer, K. Mosthaf, K. M. Smits, and R. Helmig. Heat and water transport in soils and across the soil-atmosphere interface: 1. theory and different model concepts. *Water Resources Research*, 53(2):1057–1079, 2017. doi: 10.1002/2016WR019982.

P. Verboven, D. Flick, B. Nicolaï, and G. Alvarez. Modelling transport phenomena in refrigerated food bulks, packages and stacks: basics and advances. *International Journal of Refrigeration*, 29 (6):985–997, 2006. doi: 10.1016/j.ijrefrig.2005.12.010.

H. Versteeg and W. Malalasekera. *An Introduction to Computational Fluid Dynamics: The Finite Volume Method*. Prentice Hall, 2007. ISBN 9780131274983.

R. Vuduc, A. Chandramowlishwaran, J. Choi, M. Guney, and A. Shringarpure. On the limits of GPU acceleration. In *Proceedings of the 2nd USENIX Conference on Hot Topics in Parallelism*, HotPar'10, Berkeley, CA, USA, 2010. USENIX Association.

L. Wang and H. Liu. Performance studies of PEM fuel cells with interdigitated flow fields. *Journal of Power Sources*, 134(2):185–196, 2004. doi: j.jpowsour.2004.03.055.

M. F. Wheeler and I. Yotov. Physical and computational domain decompositions for modeling subsurface flows. *Contemporary Mathematics*, 218:217–228, 1998.

F. M. White. *Fluid Mechanics*. McGraw-Hill, 4th edition, 1999. ISBN 9780072281928.

Wikipedia: The Free Encyclopedia, 2017.

D. Wilcox. *Turbulence Modeling for CFD*. DCW Industries, 1998. ISBN 9780963605153.

H.-W. Wu. A review of recent development: Transport and performance modeling of PEM fuel cells. *Applied Energy*, 165:81–106, 2016. doi: 10.1016/j.apenergy.2015.12.075.

W.-M. Yan, S.-C. Mei, C.-Y. Soong, Z.-S. Liu, and D. Song. Experimental study on the performance of PEM fuel cells with interdigitated flow channels. *Journal of Power Sources*, 160(1):116–122, 2006. doi: 10.1016/j.jpowsour.2006.01.063.

A. G. Yiotis, I. N. Tsimpanogiannis, A. K. Stubos, and Y. C. Yortsos. Coupling between external and internal mass transfer during drying of a porous medium. *Water Resources Research*, 43(6), 2007. doi: 10.1029/2006WR005558. W06403.

S. Zeng and P. Wesseling. An ILU smoother for the incompressible Navier-Stokes equations in general co-ordinates. *International Journal for Numerical Methods in Fluids*, 20(1):59–74, 1995. doi: 10.1002/fld.1650200104.

K. Zhang, A. D. Bosch-Serra, J. Boixadera, and A. J. Thompson. Investigation of water dynamics and the effect of evapotranspiration on grain yield of rainfed wheat and barley under a mediterranean environment: A modelling approach. *PLOS ONE*, 10(6):1–18, 2015. doi: 10.1371/journal.pone.0131360.

Y. Zhang. *Modélisation et simulation des dispositifs de ventilation dans les stockages de déchets radioactifs*. PhD thesis, Université Nice Sophia Antipolis, Dec 2015. URL `https://hal.inria.fr/tel-01273148`.

Institut für Wasser- und Umweltsystemmodellierung
Universität Stuttgart

Pfaffenwaldring 61
70569 Stuttgart (Vaihingen)
Telefon (0711) 685 - 64717/64749/64752/64679
Telefax (0711) 685 - 67020 o. 64746 o. 64681
E-Mail: iws@iws.uni-stuttgart.de
http://www.iws.uni-stuttgart.de

Verzeichnis der Mitteilungshefte

5 Plate, Erich: *Beitrag zur Bestimmung der Windgeschwindigkeitsverteilung in der durch eine Wand gestörten bodennahen Luftschicht*, und
Röhnisch, Arthur; Marotz, Günter: *Neue Baustoffe und Bauausführungen für den Schutz der Böschungen und der Sohle von Kanälen, Flüssen und Häfen; Gestehungskosten und jeweilige Vorteile*, sowie
Unny, T.E.: *Schwingungsuntersuchungen am Kegelstrahlschieber*, 1967

6 Seiler, Erich: *Die Ermittlung des Anlagenwertes der bundeseigenen Binnenschiffahrtsstraßen und Talsperren und des Anteils der Binnenschiffahrt an diesem Wert*, 1967

7 *Sonderheft anläßlich des 65. Geburtstages von Prof. Arthur Röhnisch mit Beiträgen von* Benk, Dieter; Breitling, J.; Gurr, Siegfried; Haberhauer, Robert; Honekamp, Hermann; Kuz, Klaus Dieter; Marotz, Günter; Mayer-Vorfelder, Hans-Jörg; Miller, Rudolf; Plate, Erich J.; Radomski, Helge; Schwarz, Helmut; Vollmer, Ernst; Wildenhahn, Eberhard; 1967

8 Jumikis, Alfred: *Beitrag zur experimentellen Untersuchung des Wassernachschubs in einem gefrierenden Boden und die Beurteilung der Ergebnisse*, 1968

9 Marotz, Günter: *Technische Grundlagen einer Wasserspeicherung im natürlichen Untergrund*, 1968

10 Radomski, Helge: *Untersuchungen über den Einfluß der Querschnittsform wellenförmiger Spundwände auf die statischen und rammtechnischen Eigenschaften*, 1968

11 Schwarz, Helmut: *Die Grenztragfähigkeit des Baugrundes bei Einwirkung vertikal gezogener Ankerplatten als zweidimensionales Bruchproblem*, 1969

12 Erbel, Klaus: *Ein Beitrag zur Untersuchung der Metamorphose von Mittelgebirgsschneedecken unter besonderer Berücksichtigung eines Verfahrens zur Bestimmung der thermischen Schneequalität*, 1969

13 Westhaus, Karl-Heinz: *Der Strukturwandel in der Binnenschiffahrt und sein Einfluß auf den Ausbau der Binnenschiffskanäle*, 1969

14 Mayer-Vorfelder, Hans-Jörg: *Ein Beitrag zur Berechnung des Erdwiderstandes unter Ansatz der logarithmischen Spirale als Gleitflächenfunktion*, 1970

15 Schulz, Manfred: *Berechnung des räumlichen Erddruckes auf die Wandung kreiszylindrischer Körper*, 1970

16 Mobasseri, Manoutschehr: *Die Rippenstützmauer. Konstruktion und Grenzen ihrer Standsicherheit*, 1970

17 Benk, Dieter: *Ein Beitrag zum Betrieb und zur Bemessung von Hochwasserrückhaltebecken*, 1970

18 Gàl, Attila: *Bestimmung der mitschwingenden Wassermasse bei überströmten Fischbauchklappen mit kreiszylindrischem Staublech*, 1971, vergriffen

19 Kuz, Klaus Dieter: *Ein Beitrag zur Frage des Einsetzens von Kavitationserscheinungen in einer Düsenströmung bei Berücksichtigung der im Wasser gelösten Gase*, 1971, vergriffen

20 Schaak, Hartmut: *Verteilleitungen von Wasserkraftanlagen*, 1971

21 *Sonderheft zur Eröffnung der neuen Versuchsanstalt des Instituts für Wasserbau der Universität Stuttgart mit Beiträgen von* Brombach, Hansjörg; Dirksen, Wolfram; Gàl, Attila; Gerlach, Reinhard; Giesecke, Jürgen; Holthoff, Franz-Josef; Kuz, Klaus Dieter; Marotz, Günter; Minor, Hans-Erwin; Petrikat, Kurt; Röhnisch, Arthur; Rueff, Helge; Schwarz, Helmut; Vollmer, Ernst; Wildenhahn, Eberhard; 1972

22 Wang, Chung-su: *Ein Beitrag zur Berechnung der Schwingungen an Kegelstrahlschiebern*, 1972

23 Mayer-Vorfelder, Hans-Jörg: *Erdwiderstandsbeiwerte nach dem Ohde-Variationsverfahren*, 1972

24 Minor, Hans-Erwin: *Beitrag zur Bestimmung der Schwingungsanfachungsfunktionen überströmter Stauklappen*, 1972, vergriffen

25 Brombach, Hansjörg: *Untersuchung strömungsmechanischer Elemente (Fluidik) und die Möglichkeit der Anwendung von Wirbelkammerelementen im Wasserbau*, 1972, vergriffen

26 Wildenhahn, Eberhard: *Beitrag zur Berechnung von Horizontalfilterbrunnen*, 1972

27 Steinlein, Helmut: *Die Eliminierung der Schwebstoffe aus Flußwasser zum Zweck der unterirdischen Wasserspeicherung, gezeigt am Beispiel der Iller*, 1972

28 Holthoff, Franz Josef: *Die Überwindung großer Hubhöhen in der Binnenschiffahrt durch Schwimmerhebewerke*, 1973

29 Röder, Karl: *Einwirkungen aus Baugrundbewegungen auf trog- und kastenförmige Konstruktionen des Wasser- und Tunnelbaues*, 1973

30 Kretschmer, Heinz: *Die Bemessung von Bogenstaumauern in Abhängigkeit von der Talform*, 1973

31 Honekamp, Hermann: *Beitrag zur Berechnung der Montage von Unterwasserpipelines*, 1973

32 Giesecke, Jürgen: *Die Wirbelkammertriode als neuartiges Steuerorgan im Wasserbau*, und Brombach, Hansjörg: *Entwicklung, Bauformen, Wirkungsweise und Steuereigenschaften von Wirbelkammerverstärkern*, 1974

33 Rueff, Helge: *Untersuchung der schwingungserregenden Kräfte an zwei hintereinander angeordneten Tiefschützen unter besonderer Berücksichtigung von Kavitation*, 1974

34 Röhnisch, Arthur: *Einpreßversuche mit Zementmörtel für Spannbeton - Vergleich der Ergebnisse von Modellversuchen mit Ausführungen in Hüllwellrohren*, 1975

35 *Sonderheft anläßlich des 65. Geburtstages von Prof. Dr.-Ing. Kurt Petrikat mit Beiträgen von*: Brombach, Hansjörg; Erbel, Klaus; Flinspach, Dieter; Fischer jr., Richard; Gàl, Attila; Gerlach, Reinhard; Giesecke, Jürgen; Haberhauer, Robert; Hafner Edzard; Hausenblas, Bernhard; Horlacher, Hans-Burkhard; Hutarew, Andreas; Knoll, Manfred; Krummet, Ralph; Marotz, Günter; Merkle, Theodor; Miller, Christoph; Minor, Hans-Erwin; Neumayer, Hans; Rao, Syamala; Rath, Paul; Rueff, Helge; Ruppert, Jürgen; Schwarz, Wolfgang; Topal-Gökceli, Mehmet; Vollmer, Ernst; Wang, Chung-su; Weber, Hans-Georg; 1975

36 Berger, Jochum: *Beitrag zur Berechnung des Spannungszustandes in rotationssymmetrisch belasteten Kugelschalen veränderlicher Wandstärke unter Gas- und Flüssigkeitsdruck durch Integration schwach singulärer Differentialgleichungen*, 1975

37 Dirksen, Wolfram: *Berechnung instationärer Abflußvorgänge in gestauten Gerinnen mittels Differenzenverfahren und die Anwendung auf Hochwasserrückhaltebecken*, 1976

38 Horlacher, Hans-Burkhard: *Berechnung instationärer Temperatur- und Wärmespannungsfelder in langen mehrschichtigen Hohlzylindern*, 1976

39 Hafner, Edzard: *Untersuchung der hydrodynamischen Kräfte auf Baukörper im Tiefwasserbereich des Meeres*, 1977, ISBN 3-921694-39-6

40 Ruppert, Jürgen: *Über den Axialwirbelkammerverstärker für den Einsatz im Wasserbau*, 1977, ISBN 3-921694-40-X

41 Hutarew, Andreas: *Beitrag zur Beeinflußbarkeit des Sauerstoffgehalts in Fließgewässern an Abstürzen und Wehren*, 1977, ISBN 3-921694-41-8, *vergriffen*

42 Miller, Christoph: *Ein Beitrag zur Bestimmung der schwingungserregenden Kräfte an unterströmten Wehren*, 1977, ISBN 3-921694-42-6

43 Schwarz, Wolfgang: *Druckstoßberechnung unter Berücksichtigung der Radial- und Längsverschiebungen der Rohrwandung*, 1978, ISBN 3-921694-43-4

44 Kinzelbach, Wolfgang: *Numerische Untersuchungen über den optimalen Einsatz variabler Kühlsysteme einer Kraftwerkskette am Beispiel Oberrhein*, 1978, ISBN 3-921694-44-2

45 Barczewski, Baldur: *Neue Meßmethoden für Wasser-Luftgemische und deren Anwendung auf zweiphasige Auftriebsstrahlen*, 1979, ISBN 3-921694-45-0

46 Neumayer, Hans: *Untersuchung der Strömungsvorgänge in radialen Wirbelkammerverstärkern*, 1979, ISBN 3-921694-46-9

47 Elalfy, Youssef-Elhassan: *Untersuchung der Strömungsvorgänge in Wirbelkammerdioden und -drosseln*, 1979, ISBN 3-921694-47-7

48 Brombach, Hansjörg: *Automatisierung der Bewirtschaftung von Wasserspeichern*, 1981, ISBN 3-921694-48-5

49 Geldner, Peter: *Deterministische und stochastische Methoden zur Bestimmung der Selbstdichtung von Gewässern*, 1981, ISBN 3-921694-49-3, *vergriffen*

50 Mehlhorn, Hans: *Temperaturveränderungen im Grundwasser durch Brauchwassereinleitungen*, 1982, ISBN 3-921694-50-7, *vergriffen*

51 Hafner, Edzard: *Rohrleitungen und Behälter im Meer*, 1983, ISBN 3-921694-51-5

52 Rinnert, Bernd: *Hydrodynamische Dispersion in porösen Medien: Einfluß von Dichteunterschieden auf die Vertikalvermischung in horizontaler Strömung*, 1983, ISBN 3-921694-52-3, *vergriffen*

53 Lindner, Wulf: *Steuerung von Grundwasserentnahmen unter Einhaltung ökologischer Kriterien*, 1983, ISBN 3-921694-53-1, *vergriffen*

54 Herr, Michael; Herzer, Jörg; Kinzelbach, Wolfgang; Kobus, Helmut; Rinnert, Bernd: *Methoden zur rechnerischen Erfassung und hydraulischen Sanierung von Grundwasserkontaminationen*, 1983, ISBN 3-921694-54-X

55 Schmitt, Paul: *Wege zur Automatisierung der Niederschlagsermittlung*, 1984, ISBN 3-921694-55-8, *vergriffen*

56 Müller, Peter: *Transport und selektive Sedimentation von Schwebstoffen bei gestautem Abfluß*, 1985, ISBN 3-921694-56-6

57 El-Qawasmeh, Fuad: *Möglichkeiten und Grenzen der Tropfbewässerung unter besonderer Berücksichtigung der Verstopfungsanfälligkeit der Tropfelemente*, 1985, ISBN 3-921694-57-4, *vergriffen*

58 Kirchenbaur, Klaus: *Mikroprozessorgesteuerte Erfassung instationärer Druckfelder am Beispiel seegangsbelasteter Baukörper*, 1985, ISBN 3-921694-58-2

59 Kobus, Helmut (Hrsg.): *Modellierung des großräumigen Wärme- und Schadstofftransports im Grundwasser*, Tätigkeitsbericht 1984/85 (DFG-Forschergruppe an den Universitäten Hohenheim, Karlsruhe und Stuttgart), 1985, ISBN 3-921694-59-0, *vergriffen*

60 Spitz, Karlheinz: *Dispersion in porösen Medien: Einfluß von Inhomogenitäten und Dichteunterschieden*, 1985, ISBN 3-921694-60-4, *vergriffen*

61 Kobus, Helmut: *An Introduction to Air-Water Flows in Hydraulics*, 1985, ISBN 3-921694-61-2

62 Kaleris, Vassilios: *Erfassung des Austausches von Oberflächen- und Grundwasser in horizontalebenen Grundwassermodellen*, 1986, ISBN 3-921694-62-0

63 Herr, Michael: *Grundlagen der hydraulischen Sanierung verunreinigter Porengrundwasserleiter*, 1987, ISBN 3-921694-63-9

64 Marx, Walter: *Berechnung von Temperatur und Spannung in Massenbeton infolge Hydratation*, 1987, ISBN 3-921694-64-7

65 Koschitzky, Hans-Peter: *Dimensionierungskonzept für Sohlbelüfter in Schußrinnen zur Vermeidung von Kavitationsschäden*, 1987, ISBN 3-921694-65-5

66 Kobus, Helmut (Hrsg.): *Modellierung des großräumigen Wärme- und Schadstofftransports im Grundwasser*, Tätigkeitsbericht 1986/87 (DFG-Forschergruppe an den Universitäten Hohenheim, Karlsruhe und Stuttgart) 1987, ISBN 3-921694-66-3

67 Söll, Thomas: *Berechnungsverfahren zur Abschätzung anthropogener Temperaturanomalien im Grundwasser*, 1988, ISBN 3-921694-67-1

68 Dittrich, Andreas; Westrich, Bernd: *Bodenseeufererosion, Bestandsaufnahme und Bewertung*, 1988, ISBN 3-921694-68-X, *vergriffen*

69 Huwe, Bernd; van der Ploeg, Rienk R.: *Modelle zur Simulation des Stickstoffhaushaltes von Standorten mit unterschiedlicher landwirtschaftlicher Nutzung*, 1988, ISBN 3-921694-69-8, *vergriffen*

70 Stephan, Karl: *Integration elliptischer Funktionen*, 1988, ISBN 3-921694-70-1

71 Kobus, Helmut; Zilliox, Lothaire (Hrsg.): *Nitratbelastung des Grundwassers, Auswirkungen der Landwirtschaft auf die Grundwasser- und Rohwasserbeschaffenheit und Maßnahmen zum Schutz des Grundwassers*. Vorträge des deutsch-französischen Kolloquiums am 6. Oktober 1988, Universitäten Stuttgart und Louis Pasteur Strasbourg (Vorträge in deutsch oder französisch, Kurzfassungen zweisprachig), 1988, ISBN 3-921694-71-X

72 Soyeaux, Renald: *Unterströmung von Stauanlagen auf klüftigem Untergrund unter Berücksichtigung laminarer und turbulenter Fließzustände*,1991, ISBN 3-921694-72-8

73 Kohane, Roberto: *Berechnungsmethoden für Hochwasserabfluß in Fließgewässern mit überströmten Vorländern*, 1991, ISBN 3-921694-73-6

74 Hassinger, Reinhard: *Beitrag zur Hydraulik und Bemessung von Blocksteinrampen in flexibler Bauweise*, 1991, ISBN 3-921694-74-4, vergriffen

75 Schäfer, Gerhard: *Einfluß von Schichtenstrukturen und lokalen Einlagerungen auf die Längsdispersion in Porengrundwasserleitern*, 1991, ISBN 3-921694-75-2

76 Giesecke, Jürgen: *Vorträge, Wasserwirtschaft in stark besiedelten Regionen; Umweltforschung mit Schwerpunkt Wasserwirtschaft*, 1991, ISBN 3-921694-76-0

77 Huwe, Bernd: *Deterministische und stochastische Ansätze zur Modellierung des Stickstoffhaushalts landwirtschaftlich genutzter Flächen auf unterschiedlichem Skalenniveau*, 1992, ISBN 3-921694-77-9, vergriffen

78 Rommel, Michael: *Verwendung von Kluftdaten zur realitätsnahen Generierung von Kluftnetzen mit anschließender laminar-turbulenter Strömungsberechnung*, 1993, ISBN 3-92 1694-78-7

79 Marschall, Paul: *Die Ermittlung lokaler Stofffrachten im Grundwasser mit Hilfe von Einbohrloch-Meßverfahren*, 1993, ISBN 3-921694-79-5, vergriffen

80 Ptak, Thomas: *Stofftransport in heterogenen Porenaquiferen: Felduntersuchungen und stochastische Modellierung*, 1993, ISBN 3-921694-80-9, vergriffen

81 Haakh, Frieder: *Transientes Strömungsverhalten in Wirbelkammern,* 1993, ISBN 3-921694-81-7

82 Kobus, Helmut; Cirpka, Olaf; Barczewski, Baldur; Koschitzky, Hans-Peter: *Versuchseinrichtung zur Grundwasser und Altlastensanierung VEGAS, Konzeption und Programmrahmen*, 1993, ISBN 3-921694-82-5

83 Zang, Weidong: *Optimaler Echtzeit-Betrieb eines Speichers mit aktueller Abflußregenerierung*, 1994, ISBN 3-921694-83-3, vergriffen

84 Franke, Hans-Jörg: *Stochastische Modellierung eines flächenhaften Stoffeintrages und Transports in Grundwasser am Beispiel der Pflanzenschutzmittelproblematik*, 1995, ISBN 3-921694-84-1

85 Lang, Ulrich: *Simulation regionaler Strömungs- und Transportvorgänge in Karstaquiferen mit Hilfe des Doppelkontinuum-Ansatzes: Methodenentwicklung und Parameteridentifikation*, 1995, ISBN 3-921694-85-X, vergriffen

86 Helmig, Rainer: *Einführung in die Numerischen Methoden der Hydromechanik*, 1996, ISBN 3-921694-86-8, vergriffen

87 Cirpka, Olaf: *CONTRACT: A Numerical Tool for Contaminant Transport and Chemical Transformations - Theory and Program Documentation -*, 1996, ISBN 3-921694-87-6

88 Haberlandt, Uwe: *Stochastische Synthese und Regionalisierung des Niederschlages für Schmutzfrachtberechnungen*, 1996, ISBN 3-921694-88-4

89 Croisé, Jean: *Extraktion von flüchtigen Chemikalien aus natürlichen Lockergesteinen mittels erzwungener Luftströmung*, 1996, ISBN 3-921694-89-2, vergriffen

90 Jorde, Klaus: *Ökologisch begründete, dynamische Mindestwasserregelungen bei Ausleitungskraftwerken*, 1997, ISBN 3-921694-90-6, vergriffen

91 Helmig, Rainer: *Gekoppelte Strömungs- und Transportprozesse im Untergrund - Ein Beitrag zur Hydrosystemmodellierung-*, 1998, ISBN 3-921694-91-4, vergriffen

92 Emmert, Martin: *Numerische Modellierung nichtisothermer Gas-Wasser Systeme in porösen Medien,* 1997, ISBN 3-921694-92-2

93 Kern, Ulrich: *Transport von Schweb- und Schadstoffen in staugeregelten Fließgewässern am Beispiel des Neckars*, 1997, ISBN 3-921694-93-0, vergriffen

94 Förster, Georg: *Druckstoßdämpfung durch große Luftblasen in Hochpunkten von Rohrleitungen 1997*, ISBN 3-921694-94-9

95 Cirpka, Olaf: *Numerische Methoden zur Simulation des reaktiven Mehrkomponententransports im Grundwasser*, 1997, ISBN 3-921694-95-7, *vergriffen*

96 Färber, Arne: *Wärmetransport in der ungesättigten Bodenzone: Entwicklung einer thermischen In-situ-Sanierungstechnologie*, 1997, ISBN 3-921694-96-5

97 Betz, Christoph: *Wasserdampfdestillation von Schadstoffen im porösen Medium: Entwicklung einer thermischen In-situ-Sanierungstechnologie*, 1998, SBN 3-921694-97-3

98 Xu, Yichun: *Numerical Modeling of Suspended Sediment Transport in Rivers*, 1998, ISBN 3-921694-98-1, *vergriffen*

99 Wüst, Wolfgang: *Geochemische Untersuchungen zur Sanierung CKW-kontaminierter Aquifere mit Fe(0)-Reaktionswänden,* 2000, ISBN 3-933761-02-2

100 Sheta, Hussam: *Simulation von Mehrphasenvorgängen in porösen Medien unter Einbeziehung von Hysterese-Effekten*, 2000, ISBN 3-933761-03-4

101 Ayros, Edwin: *Regionalisierung extremer Abflüsse auf der Grundlage statistischer Verfahren*, 2000, ISBN 3-933761-04-2, *vergriffen*

102 Huber, Ralf: *Compositional Multiphase Flow and Transport in Heterogeneous Porous Media*, 2000, ISBN 3-933761-05-0

103 Braun, Christopherus: *Ein Upscaling-Verfahren für Mehrphasenströmungen in porösen Medien*, 2000, ISBN 3-933761-06-9

104 Hofmann, Bernd: *Entwicklung eines rechnergestützten Managementsystems zur Beurteilung von Grundwasserschadensfällen*, 2000, ISBN 3-933761-07-7

105 Class, Holger: *Theorie und numerische Modellierung nichtisothermer Mehrphasenprozesse in NAPL-kontaminierten porösen Medien,* 2001, ISBN 3-933761-08-5

106 Schmidt, Reinhard: *Wasserdampf- und Heißluftinjektion zur thermischen Sanierung kontaminierter Standorte*, 2001, ISBN 3-933761-09-3

107 Josef, Reinhold:, *Schadstoffextraktion mit hydraulischen Sanierungsverfahren unter Anwendung von grenzflächenaktiven Stoffen*, 2001, ISBN 3-933761-10-7

108 Schneider, Matthias: *Habitat- und Abflussmodellierung für Fließgewässer mit unscharfen Berechnungsansätzen*, 2001, ISBN 3-933761-11-5

109 Rathgeb, Andreas: *Hydrodynamische Bemessungsgrundlagen für Lockerdeckwerke an überströmbaren Erddämmen*, 2001, ISBN 3-933761-12-3

110 Lang, Stefan: *Parallele numerische Simulation instätionärer Probleme mit adaptiven Methoden auf unstrukturierten Gittern*, 2001, ISBN 3-933761-13-1

111 Appt, Jochen; Stumpp Simone: *Die Bodensee-Messkampagne 2001, IWS/CWR Lake Constance Measurement Program 2001*, 2002, ISBN 3-933761-14-X

112 Heimerl, Stephan: *Systematische Beurteilung von Wasserkraftprojekten,* 2002, ISBN 3-933761-15-8, *vergriffen*

113 Iqbal, Amin: *On the Management and Salinity Control of Drip Irrigation,* 2002, ISBN 3-933761-16-6

114 Silberhorn-Hemminger, Annette: *Modellierung von Kluftaquifersystemen: Geostatistische Analyse und deterministisch-stochastische Kluftgenerierung,* 2002, ISBN 3-933761-17-4

115 Winkler, Angela: *Prozesse des Wärme- und Stofftransports bei der In-situ-Sanierung mit festen Wärmequellen,* 2003, ISBN 3-933761-18-2

116 Marx, Walter: *Wasserkraft, Bewässerung, Umwelt - Planungs- und Bewertungsschwerpunkte der Wasserbewirtschaftung,* 2003, ISBN 3-933761-19-0

117 Hinkelmann, Reinhard: *Efficient Numerical Methods and Information-Processing Techniques in Environment Water,* 2003, ISBN 3-933761-20-4

118 Samaniego-Eguiguren, Luis Eduardo: *Hydrological Consequences of Land Use / Land Cover and Climatic Changes in Mesoscale Catchments*, 2003, ISBN 3-933761-21-2

119 Neunhäuserer, Lina: *Diskretisierungsansätze zur Modellierung von Strömungs- und Transportprozessen in geklüftet-porösen Medien*, 2003, ISBN 3-933761-22-0

120 Paul, Maren: *Simulation of Two-Phase Flow in Heterogeneous Poros Media with Adaptive Methods*, 2003, ISBN 3-933761-23-9

121 Ehret, Uwe: *Rainfall and Flood Nowcasting in Small Catchments using Weather Radar*, 2003, ISBN 3-933761-24-7

122 Haag, Ingo: *Der Sauerstoffhaushalt staugeregelter Flüsse am Beispiel des Neckars - Analysen, Experimente, Simulationen -,* 2003, ISBN 3-933761-25-5

123 Appt, Jochen: *Analysis of Basin-Scale Internal Waves in Upper Lake Constance,* 2003, ISBN 3-933761-26-3

124 Hrsg.: Schrenk, Volker; Batereau, Katrin; Barczewski, Baldur; Weber, Karolin und Koschitzky, Hans-Peter: *Symposium Ressource Fläche und VEGAS - Statuskolloquium 2003, 30. September und 1. Oktober 2003,* 2003, ISBN 3-933761-27-1

125 Omar Khalil Ouda: *Optimisation of Agricultural Water Use: A Decision Support System for the Gaza Strip,* 2003, ISBN 3-933761-28-0

126 Batereau, Katrin: *Sensorbasierte Bodenluftmessung zur Vor-Ort-Erkundung von Schadensherden im Untergrund*, 2004, ISBN 3-933761-29-8

127 Witt, Oliver: *Erosionsstabilität von Gewässersedimenten mit Auswirkung auf den Stofftransport bei Hochwasser am Beispiel ausgewählter Stauhaltungen des Oberrheins*, 2004, ISBN 3-933761-30-1

128 Jakobs, Hartmut: *Simulation nicht-isothermer Gas-Wasser-Prozesse in komplexen Kluft-Matrix-Systemen*, 2004, ISBN 3-933761-31-X

129 Li, Chen-Chien: *Deterministisch-stochastisches Berechnungskonzept zur Beurteilung der Auswirkungen erosiver Hochwasserereignisse in Flussstauhaltungen,* 2004, ISBN 3-933761-32-8

130 Reichenberger, Volker; Helmig, Rainer; Jakobs, Hartmut; Bastian, Peter; Niessner, Jennifer: *Complex Gas-Water Processes in Discrete Fracture-Matrix Systems: Up-scaling, Mass-Conservative Discretization and Efficient Multilevel Solution,* 2004, ISBN 3-933761-33-6

131 Hrsg.: Barczewski, Baldur; Koschitzky, Hans-Peter; Weber, Karolin; Wege, Ralf: *VEGAS - Statuskolloquium 2004,* Tagungsband zur Veranstaltung am 05. Oktober 2004 an der Universität Stuttgart, Campus Stuttgart-Vaihingen, 2004, ISBN 3-933761-34-4

132 Asie, Kemal Jabir: *Finite Volume Models for Multiphase Multicomponent Flow through Porous Media*. 2005, ISBN 3-933761-35-2

133 Jacoub, George: *Development of a 2-D Numerical Module for Particulate Contaminant Transport in Flood Retention Reservoirs and Impounded Rivers,* 2004, ISBN 3-933761-36-0

134 Nowak, Wolfgang: *Geostatistical Methods for the Identification of Flow and Transport Parameters in the Subsurface,* 2005, ISBN 3-933761-37-9

135 Süß, Mia: *Analysis of the influence of structures and boundaries on flow and transport processes in fractured porous media*, 2005, ISBN 3-933761-38-7

136 Jose, Surabhin Chackiath: *Experimental Investigations on Longitudinal Dispersive Mixing in Heterogeneous Aquifers,* 2005, ISBN: 3-933761-39-5

137 Filiz, Fulya: *Linking Large-Scale Meteorological Conditions to Floods in Mesoscale Catchments,* 2005, ISBN 3-933761-40-9

138 Qin, Minghao: *Wirklichkeitsnahe und recheneffiziente Ermittlung von Temperatur und Spannungen bei großen RCC-Staumauern*, 2005, ISBN 3-933761-41-7

139 Kobayashi, Kenichiro: *Optimization Methods for Multiphase Systems in the Subsurface - Application to Methane Migration in Coal Mining Areas*, 2005, ISBN 3-933761-42-5

140 Rahman, Md. Arifur: *Experimental Investigations on Transverse Dispersive Mixing in Heterogeneous Porous Media,* 2005, ISBN 3-933761-43-3

141 Schrenk, Volker: *Ökobilanzen zur Bewertung von Altlastensanierungsmaßnahmen,* 2005, ISBN 3-933761-44-1

142 Hundecha, Hirpa Yeshewatesfa: *Regionalization of Parameters of a Conceptual Rainfall-Runoff Model*, 2005, ISBN: 3-933761-45-X

143 Wege, Ralf: *Untersuchungs- und Überwachungsmethoden für die Beurteilung natürlicher Selbstreinigungsprozesse im Grundwasser,* 2005, ISBN 3-933761-46-8

144 Breiting, Thomas: *Techniken und Methoden der Hydroinformatik - Modellierung von komplexen Hydrosystemen im Untergrund*, 2006, ISBN 3-933761-47-6

145 Hrsg.: Braun, Jürgen; Koschitzky, Hans-Peter; Müller, Martin: *Ressource Untergrund: 10 Jahre VEGAS: Forschung und Technologieentwicklung zum Schutz von Grundwasser und Boden,* Tagungsband zur Veranstaltung am 28. und 29. September 2005 an der Universität Stuttgart, Campus Stuttgart-Vaihingen, 2005, ISBN 3-933761-48-4

146 Rojanschi, Vlad: *Abflusskonzentration in mesoskaligen Einzugsgebieten unter Berücksichtigung des Sickerraumes,* 2006, ISBN 3-933761-49-2

147 Winkler, Nina Simone: *Optimierung der Steuerung von Hochwasserrückhaltebeckensystemen,* 2006, ISBN 3-933761-50-6

148 Wolf, Jens: *Räumlich differenzierte Modellierung der Grundwasserströmung alluvialer Aquifere für mesoskalige Einzugsgebiete*, 2006, ISBN: 3-933761-51-4

149 Kohler, Beate: *Externe Effekte der Laufwasserkraftnutzung*, 2006, ISBN 3-933761-52-2

150 Hrsg.: Braun, Jürgen; Koschitzky, Hans-Peter; Stuhrmann, Matthias: *VEGAS-Statuskolloquium 2006,* Tagungsband zur Veranstaltung am 28. September 2006 an der Universität Stuttgart, Campus Stuttgart-Vaihingen, 2006, ISBN 3-933761-53-0

151 Niessner, Jennifer: *Multi-Scale Modeling of Multi-Phase - Multi-Component Processes in Heterogeneous Porous Media*, 2006, ISBN 3-933761-54-9

152 Fischer, Markus: *Beanspruchung eingeerdeter Rohrleitungen infolge Austrocknung bindiger Böden,* 2006, ISBN 3-933761-55-7

153 Schneck, Alexander: *Optimierung der Grundwasserbewirtschaftung unter Berücksichtigung der Belange der Wasserversorgung, der Landwirtschaft und des Naturschutzes*, 2006, ISBN 3-933761-56-5

154 Das, Tapash: *The Impact of Spatial Variability of Precipitation on the Predictive Uncertainty of Hydrological Models,* 2006, ISBN 3-33761-57-3

155 Bielinski, Andreas: *Numerical Simulation of CO_2 sequestration in geological formations*, 2007, ISBN 3-933761-58-1

156 Mödinger, Jens: *Entwicklung eines Bewertungs- und Entscheidungsunterstützungssystems für eine nachhaltige regionale Grundwasserbewirtschaftung*, 2006, ISBN 3-933761-60-3

157 Manthey, Sabine: *Two-phase flow processes with dynamic effects in porous media - parameter estimation and simulation,* 2007, ISBN 3-933761-61-1

158 Pozos Estrada, Oscar: *Investigation on the Effects of Entrained Air in Pipelines,* 2007, ISBN 3-933761-62-X

159 Ochs, Steffen Oliver: *Steam injection into saturated porous media – process analysis including experimental and numerical investigations*, 2007, ISBN 3-933761-63-8

160 Marx, Andreas: *Einsatz gekoppelter Modelle und Wetterradar zur Abschätzung von Niederschlagsintensitäten und zur Abflussvorhersage, 2007,* ISBN 3-933761-64-6

161 Hartmann, Gabriele Maria: *Investigation of Evapotranspiration Concepts in Hydrological Modelling for Climate Change Impact Assessment*, 2007, ISBN 3-933761-65-4

162 Kebede Gurmessa, Tesfaye: *Numerical Investigation on Flow and Transport Characteristics to Improve Long-Term Simulation of Reservoir Sedimentation*, 2007, ISBN 3-933761-66-2

163 Trifković, Aleksandar: *Multi-objective and Risk-based Modelling Methodology for Planning, Design and Operation of Water Supply Systems*, 2007, ISBN 3-933761-67-0

164 Götzinger, Jens: *Distributed Conceptual Hydrological Modelling - Simulation of Climate, Land Use Change Impact and Uncertainty Analysis*, 2007, ISBN 3-933761-68-9

165 Hrsg.: Braun, Jürgen; Koschitzky, Hans-Peter; Stuhrmann, Matthias: *VEGAS – Kolloquium 2007,* Tagungsband zur Veranstaltung am 26. September 2007 an der Universität Stuttgart, Campus Stuttgart-Vaihingen, 2007, ISBN 3-933761-69-7

166 Freeman, Beau: *Modernization Criteria Assessment for Water Resources Planning; Klamath Irrigation Project, U.S.*, 2008, ISBN 3-933761-70-0

167 Dreher, Thomas: *Selektive Sedimentation von Feinstschwebstoffen in Wechselwirkung mit wandnahen turbulenten Strömungsbedingungen*, 2008, ISBN 3-933761-71-9

168 Yang, Wei: *Discrete-Continuous Downscaling Model for Generating Daily Precipitation Time Series*, 2008, ISBN 3-933761-72-7

169 Kopecki, Ianina: *Calculational Approach to FST-Hemispheres for Multiparametrical Benthos Habitat Modelling,* 2008*,* ISBN 3-933761-73-5

170 Brommundt, Jürgen: *Stochastische Generierung räumlich zusammenhängender Niederschlagszeitreihen*, 2008, ISBN 3-933761-74-3

171 Papafotiou, *Alexandros: Numerical Investigations of the Role of Hysteresis in Heterogeneous Two-Phase Flow Systems*, 2008, ISBN 3-933761-75-1

172 He, Yi: *Application of a Non-Parametric Classification Scheme to Catchment Hydrology*, 2008, ISBN 978-3-933761-76-7

173 Wagner, Sven: *Water Balance in a Poorly Gauged Basin in West Africa Using Atmospheric Modelling and Remote Sensing Information*, 2008, ISBN 978-3-933761-77-4

174 Hrsg.: Braun, Jürgen; Koschitzky, Hans-Peter; Stuhrmann, Matthias; Schrenk, Volker: *VEGAS-Kolloquium 2008 Ressource Fläche III*, Tagungsband zur Veranstaltung am 01. Oktober 2008 an der Universität Stuttgart, Campus Stuttgart-Vaihingen, 2008, ISBN 978-3-933761-78-1

175 Patil, Sachin: *Regionalization of an Event Based Nash Cascade Model for Flood Predictions in Ungauged Basins*, 2008, ISBN 978-3-933761-79-8

176 Assteerawatt, Anongnart: *Flow and Transport Modelling of Fractured Aquifers based on a Geostatistical Approach,* 2008, ISBN 978-3-933761-80-4

177 Karnahl, Joachim Alexander: *2D numerische Modellierung von multifraktionalem Schwebstoff- und Schadstofftransport in Flüssen*, 2008, ISBN 978-3-933761-81-1

178 Hiester, Uwe: *Technologieentwicklung zur In-situ-Sanierung der ungesättigten Bodenzone mit festen Wärmequellen,* 2009, ISBN 978-3-933761-82-8

179 Laux, Patrick: *Statistical Modeling of Precipitation for Agricultural Planning in the Volta Basin of West Africa,* 2009, ISBN 978-3-933761-83-5

180 Ehsan, Saqib: *Evaluation of Life Safety Risks Related to Severe Flooding,* 2009, ISBN 978-3-933761-84-2

181 Prohaska, Sandra: *Development and Application of a 1D Multi-Strip Fine Sediment Transport Model for Regulated Rivers,* 2009, ISBN 978-3-933761-85-9

182 Kopp, Andreas: *Evaluation of CO_2 Injection Processes in Geological Formations for Site Screening,* 2009, ISBN 978-3-933761-86-6

183 Ebigbo, Anozie: *Modelling of biofilm growth and its influence on CO_2 and water (two-phase) flow in porous media,* 2009, ISBN 978-3-933761-87-3

184 Freiboth, Sandra: *A phenomenological model for the numerical simulation of multiphase multicomponent processes considering structural alterations of porous media*, 2009, ISBN 978-3-933761-88-0

185 Zöllner, Frank: *Implementierung und Anwendung netzfreier Methoden im Konstruktiven Wasserbau und in der Hydromechanik*, 2009, ISBN 978-3-933761-89-7

186 Vasin, Milos: *Influence of the soil structure and property contrast on flow and transport in the unsaturated zone*, 2010, ISBN 978-3-933761-90-3

187 Li, Jing: *Application of Copulas as a New Geostatistical Tool*, 2010, ISBN 978-3-933761-91-0

188 AghaKouchak, Amir: *Simulation of Remotely Sensed Rainfall Fields Using Copulas*, 2010, ISBN 978-3-933761-92-7

189 Thapa, Pawan Kumar: *Physically-based spatially distributed rainfall runoff modelling for soil erosion estimation*, 2010, ISBN 978-3-933761-93-4

190 Wurms, Sven: *Numerische Modellierung der Sedimentationsprozesse in Retentionsanlagen zur Steuerung von Stoffströmen bei extremen Hochwasserabflussereignissen*, 2011, ISBN 978-3-933761-94-1

191 Merkel, Uwe: *Unsicherheitsanalyse hydraulischer Einwirkungen auf Hochwasserschutzdeiche und Steigerung der Leistungsfähigkeit durch adaptive Strömungsmodellierung*, 2011, ISBN 978-3-933761-95-8

192 Fritz, Jochen: *A Decoupled Model for Compositional Non-Isothermal Multiphase Flow in Porous Media and Multiphysics Approaches for Two-Phase Flow*, 2010, ISBN 978-3-933761-96-5

193 Weber, Karolin (Hrsg.): *12. Treffen junger WissenschaftlerInnen an Wasserbauinstituten*, 2010, ISBN 978-3-933761-97-2

194 Bliefernicht, Jan-Geert: *Probability Forecasts of Daily Areal Precipitation for Small River Basins,* 2011, ISBN 978-3-933761-98-9

195 Hrsg.: Koschitzky, Hans-Peter; Braun, Jürgen: *VEGAS-Kolloquium 2010 In-situ-Sanierung - Stand und Entwicklung Nano und ISCO -,* Tagungsband zur Veranstaltung am 07. Oktober 2010 an der Universität Stuttgart, Campus Stuttgart-Vaihingen*,* 2010*,* ISBN 978-3-933761-99-6

196 Gafurov, Abror: *Water Balance Modeling Using Remote Sensing Information - Focus on Central Asia,* 2010, ISBN 978-3-942036-00-9

197 Mackenberg, Sylvia: *Die Quellstärke in der Sickerwasserprognose: Möglichkeiten und Grenzen von Labor- und Freilanduntersuchungen,* 2010, ISBN 978-3-942036-01-6

198 Singh, Shailesh Kumar: *Robust Parameter Estimation in Gauged and Ungauged Basins,* 2010, ISBN 978-3-942036-02-3

199 Doğan, Mehmet Onur: *Coupling of porous media flow with pipe flow,* 2011, ISBN 978-3-942036-03-0

200 Liu, Min: *Study of Topographic Effects on Hydrological Patterns and the Implication on Hydrological Modeling and Data Interpolation,* 2011, ISBN 978-3-942036-04-7

201 Geleta, Habtamu Itefa: *Watershed Sediment Yield Modeling for Data Scarce Areas,* 2011, ISBN 978-3-942036-05-4

202 Franke, Jörg: *Einfluss der Überwachung auf die Versagenswahrscheinlichkeit von Staustufen,* 2011, ISBN 978-3-942036-06-1

203 Bakimchandra, Oinam: *Integrated Fuzzy-GIS approach for assessing regional soil erosion risks,* 2011, ISBN 978-3-942036-07-8

204 Alam, Muhammad Mahboob: *Statistical Downscaling of Extremes of Precipitation in Mesoscale Catchments from Different RCMs and Their Effects on Local Hydrology ,* 2011, ISBN 978-3-942036-08-5

205 Hrsg.: Koschitzky, Hans-Peter; Braun, Jürgen: *VEGAS-Kolloquium 2011 Flache Geothermie - Perspektiven und Risiken,* Tagungsband zur Veranstaltung am 06. Oktober 2011 an der Universität Stuttgart, Campus Stuttgart-Vaihingen*,* 2011*,* ISBN 978-3-933761-09-2

206 Haslauer, Claus: *Analysis of Real-World Spatial Dependence of Subsurface Hydraulic Properties Using Copulas with a Focus on Solute Transport Behaviour,* 2011, ISBN 978-3-942036-10-8

207 Dung, Nguyen Viet: *Multi-objective automatic calibration of hydrodynamic models – development of the concept and an application in the Mekong Delta,* 2011, ISBN 978-3-942036-11-5

208 Hung, Nguyen Nghia: *Sediment dynamics in the floodplain of the Mekong Delta, Vietnam,* 2011, ISBN 978-3-942036-12-2

209 Kuhlmann, Anna: *Influence of soil structure and root water uptake on flow in the unsaturated zone,* 2012, ISBN 978-3-942036-13-9

210 Tuhtan, Jeffrey Andrew: *Including the Second Law Inequality in Aquatic Ecodynamics: A Modeling Approach for Alpine Rivers Impacted by Hydropeaking,* 2012, ISBN 978-3-942036-14-6

211 Tolossa, Habtamu: *Sediment Transport Computation Using a Data-Driven Adaptive Neuro-Fuzzy Modelling Approach,* 2012, ISBN 978-3-942036-15-3

212 Tatomir, Alexandru-Bodgan: *From Discrete to Continuum Concepts of Flow in Fractured Porous Media,* 2012, ISBN 978-3-942036-16-0

213 Erbertseder, Karin: *A Multi-Scale Model for Describing Cancer-Therapeutic Transport in the Human Lung,* 2012, ISBN 978-3-942036-17-7

214 Noack, Markus: *Modelling Approach for Interstitial Sediment Dynamics and Reproduction of Gravel Spawning Fish,* 2012, ISBN 978-3-942036-18-4

215 De Boer, Cjestmir Volkert: *Transport of Nano Sized Zero Valent Iron Colloids during Injection into the Subsurface*, 2012, ISBN 978-3-942036-19-1

216 Pfaff, Thomas: *Processing and Analysis of Weather Radar Data for Use in Hydrology*, 2013, ISBN 978-3-942036-20-7

217 Lebrenz, Hans-Henning: *Addressing the Input Uncertainty for Hydrological Modeling by a New Geostatistical Method*, 2013, ISBN 978-3-942036-21-4

218 Darcis, Melanie Yvonne: *Coupling Models of Different Complexity for the Simulation of CO_2 Storage in Deep Saline Aquifers*, 2013, ISBN 978-3-942036-22-1

219 Beck, Ferdinand: *Generation of Spatially Correlated Synthetic Rainfall Time Series in High Temporal Resolution - A Data Driven Approach*, 2013, ISBN 978-3-942036-23-8

220 Guthke, Philipp: *Non-multi-Gaussian spatial structures: Process-driven natural genesis, manifestation, modeling approaches, and influences on dependent processes*, 2013, ISBN 978-3-942036-24-5

221 Walter, Lena: *Uncertainty studies and risk assessment for CO_2 storage in geological formations*, 2013, ISBN 978-3-942036-25-2

222 Wolff, Markus: *Multi-scale modeling of two-phase flow in porous media including capillary pressure effects,* 2013, ISBN 978-3-942036-26-9

223 Mosthaf, Klaus Roland: *Modeling and analysis of coupled porous-medium and free flow with application to evaporation processes,* 2014, ISBN 978-3-942036-27-6

224 Leube, Philipp Christoph: *Methods for Physically-Based Model Reduction in Time: Analysis, Comparison of Methods and Application*, 2013, ISBN 978-3-942036-28-3

225 Rodríguez Fernández, Jhan Ignacio: *High Order Interactions among environmental variables: Diagnostics and initial steps towards modeling*, 2013, ISBN 978-3-942036-29-0

226 Eder, Maria Magdalena: *Climate Sensitivity of a Large Lake*, 2013, ISBN 978-3-942036-30-6

227 Greiner, Philipp: *Alkoholinjektion zur In-situ-Sanierung von CKW Schadensherden in Grundwasserleitern: Charakterisierung der relevanten Prozesse auf unterschiedlichen Skalen*, 2014, ISBN 978-3-942036-31-3

228 Lauser, Andreas: *Theory and Numerical Applications of Compositional Multi-Phase Flow in Porous Media*, 2014, ISBN 978-3-942036-32-0

229 Enzenhöfer, Rainer: *Risk Quantification and Management in Water Production and Supply Systems*, 2014, ISBN 978-3-942036-33-7

230 Faigle, Benjamin: *Adaptive modelling of compositional multi-phase flow with capillary pressure*, 2014, ISBN 978-3-942036-34-4

231 Oladyshkin, Sergey: *Efficient modeling of environmental systems in the face of complexity and uncertainty*, 2014, ISBN 978-3-942036-35-1

232 Sugimoto, Takayuki: *Copula based Stochastic Analysis of Discharge Time Series*, 2014, ISBN 978-3-942036-36-8

233 Koch, Jonas: *Simulation, Identification and Characterization of Contaminant Source Architectures in the Subsurface*, 2014, ISBN 978-3-942036-37-5

234 Zhang, Jin: *Investigations on Urban River Regulation and Ecological Rehabilitation Measures, Case of Shenzhen in China*, 2014, ISBN 978-3-942036-38-2

235 Siebel, Rüdiger: *Experimentelle Untersuchungen zur hydrodynamischen Belastung und Standsicherheit von Deckwerken an überströmbaren Erddämmen,* 2014, ISBN 978-3-942036-39-9

236 Baber, Katherina: *Coupling free flow and flow in porous media in biological and technical applications: From a simple to a complex interface description,* 2014, ISBN 978-3-942036-40-5

237 Nuske, Klaus Philipp: *Beyond Local Equilibrium — Relaxing local equilibrium assumptions in multiphase flow in porous media,* 2014, ISBN 978-3-942036-41-2

238 Geiges, Andreas: *Efficient concepts for optimal experimental design in nonlinear environmental systems*, 2014, ISBN 978-3-942036-42-9

239 Schwenck, Nicolas: *An XFEM-Based Model for Fluid Flow in Fractured Porous Media*, 2014, ISBN 978-3-942036-43-6

240 Chamorro Chávez, Alejandro: *Stochastic and hydrological modelling for climate change prediction in the Lima region, Peru*, 2015, ISBN 978-3-942036-44-3

241 Yulizar: *Investigation of Changes in Hydro-Meteorological Time Series Using a Depth-Based Approach*, 2015, ISBN 978-3-942036-45-0

242 Kretschmer, Nicole: *Impacts of the existing water allocation scheme on the Limarí watershed – Chile, an integrative approach*, 2015, ISBN 978-3-942036-46-7

243 Kramer, Matthias: *Luftbedarf von Freistrahlturbinen im Gegendruckbetrieb*, 2015, ISBN 978-3-942036-47-4

244 Hommel, Johannes: *Modeling biogeochemical and mass transport processes in the subsurface: Investigation of microbially induced calcite precipitation*, 2016, ISBN 978-3-942036-48-1

245 Germer, Kai: *Wasserinfiltration in die ungesättigte Zone eines makroporösen Hanges und deren Einfluss auf die Hangstabilität*, 2016, ISBN 978-3-942036-49-8

246 Hörning, Sebastian: *Process-oriented modeling of spatial random fields using copulas*, 2016, ISBN 978-3-942036-50-4

247 Jambhekar, Vishal: *Numerical modeling and analysis of evaporative salinization in a coupled free-flow porous-media system,* 2016, ISBN 978-3-942036-51-1

248 Huang, Yingchun: *Study on the spatial and temporal transferability of conceptual hydrological models*, 2016, ISBN 978-3-942036-52-8

249 Kleinknecht, Simon Matthias: *Migration and retention of a heavy NAPL vapor and remediation of the unsaturated zone*, 2016, ISBN 978-3-942036-53-5

250 Kwakye, Stephen Oppong: *Study on the effects of climate change on the hydrology of the West African sub-region*, 2016, ISBN 978-3-942036-54-2

251 Kissinger, Alexander: *Basin-Scale Site Screening and Investigation of Possible Impacts of CO_2 Storage on Subsurface Hydrosystems*, 2016, ISBN 978-3-942036-55-9

252 Sinsbeck, Michael: *Uncertainty Quantification for Expensive Simulations – Optimal Surrogate Modeling under Time Constraints*, 2017, ISBN 978-3-942036-56-6

253 Grüninger, Christoph: *Numerical Coupling of Navier-Stokes and Darcy Flow for Soil-Water Evaporation*, 2017, ISBN 978-3-942036-57-3

Die Mitteilungshefte ab der Nr. 134 (Jg. 2005) stehen als pdf-Datei über die Homepage des Instituts: www.iws.uni-stuttgart.de zur Verfügung.